On the Use of Absorbing and Matching Metasurfaces for Microwave Imaging

by

Ziqi Liu

A Thesis submitted to the Faculty of Graduate Studies of
The University of Manitoba
in partial fulfilment of the requirements of the degree of

MASTER OF SCIENCE

Department of Electrical and Computer Engineering
University of Manitoba
Winnipeg

Abstract

This thesis aims to investigate the use of electromagnetic metasurfaces in microwave imaging (MWI) to provide advantages for the development of imaging systems. In particular, this thesis is focused on two main contributions: (1) the use of absorbing metasurfaces in MWI, and (2) the use of matching metasurfaces in MWI.

Firstly, metallic-backed absorbing metasurfaces are proposed to be used as the casing of MWI systems to not only shield the imaging system from external noise but also reduce the reflections from the casing back to the imaging domain. Metasurfaces are thin and light weight, thus making them suitable for portable MWI systems. In addition, metasurfaces at the microwave frequency range can be fabricated using standard printed circuit board (PCB) technology. Using simulated data in Ansys HFSS, we demonstrate the potential of using this type of enclosure for MWI systems. Finally, we fabricate one metallic-backed absorbing metasurface to evaluate its reflectivity.

Secondly, matching metasurfaces are investigated for MWI as impedance transformers to more efficiently couple microwave energy into the target. This is important as sufficient interrogation of the target is essential for successful imaging. This will also alleviate the necessity of using coupling liquids in MWI. Similar to the absorbing metasurfaces, matching metasurfaces are also thin, light weight, and easy to manufacture at the microwave frequency range, thus making them suitable for MWI. Using simulated data in Ansys HFSS and an appropriate calibration technique, we demonstrate the possibility of using matching metasurfaces in MWI. Also, one matching metasurface is fabricated and measured to verify its matching performance.

For both cases, the disadvantages of using metasurfaces for MWI are discussed. For the metasurfaces that we used in this research, the main disadvantage is their angular dependency, which affects their performance for complex scattering scenarios. The main future work should be focused on experimental evaluation of these metasurfaces in a real imaging chamber where practical issues such antenna mutual coupling and antenna impedance matching are present.

Contributions

This thesis includes the following contributions:

Refereed Journal Papers

1. Ziqi Liu, Nozhan Bayat and Puyan Mojabi, "On the Use of Absorbing Metasurfaces in Microwave Imaging," *accepted for IEEE Transactions on Antennas and Propagation.* Manuscript ID: AP2010-1956.R2.

   – Ziqi Liu: manuscript preparation, metasurface design, simulation, and measurement

   – Nozhan Bayet: MR-GNI, MR-CSI inverse scattering algorithms

   – Puyan Mojabi: measurement, advisory role

Refereed Conference Papers

1. Ziqi Liu, Nozhan Bayat and Puyan Mojabi, "On Microwave Imaging with Absorbing Metasurface Enclosure," *IEEE AP-S Symposium on Antennas and Propagation and USNC-URSI Radio Science Meeting*, Montreal, July 2020.

   – Ziqi Liu: manuscript preparation, metasurface design, simulation

   – Nozhan Bayet: MR-GNI, MR-CSI inverse scattering algorithms

   – Puyan Mojabi: Advisory role

2. Ziqi Liu and Puyan Mojabi, "Investigating the Use of Matching Metasurfaces in Microwave Imaging," *IEEE AP-S Symposium on Antennas and Propagation and USNC-URSI Radio Science Meeting (Submitted)*, Singapore, Dec 2021.

   – Ziqi Liu: manuscript preparation, metasurface design and simulation

   – Puyan Mojabi: Inverse scattering algorithm and advisory role

Acknowledgements

First of all, I would like to thank my supervisor, Prof. Puyan Mojabi, for his invaluable guidance, and endless support. Without his help, and encouragements, I would not be able to finish this work.

I would like to acknowledge Prof. Greg Bridges and Prof. Vladimir Okhmatovski for taking time to evaluate this thesis, and valuable comments.

Also, I would like to thank all Puyan's group members for having a good time with you guys for these two years.

Special thanks to technical staffs Mr. Ehsan Zeynali and Mr. Cory Smit for helping me with the manufacturing and the measurement system setup.

Lastly, I want to thank the University of Manitoba UMGF and GETS program, as well as the Canada Research Chair (CRC) program.

Dedication

To my parents, Yan Liu
& Aijun Liu

Table of Contents

List of Abbreviations

Abbreviation	Description
1D	One-dimensional
2D	Two-dimensional
3D	Three-dimensional
EM	Electromagnetic
TE	Transverse electric
TM	Transverse magnetic
GSTCs	Generalized sheet transition conditions
EMS	Electromagnetic metasurfaces
MWI	Microwave imaging
OI	Object of interest
SNR	Signal-to-noise ratio
PCB	Printed circuit board
PML	Perfectly matched layer
PEC	Perfect electric conductor
PMC	Perfect magnetic conductor
MR	Multiplicative regularization
SP	Spatial prior
GNI	Gauss-Newton inversion
CSI	Contrast source inversion
MoM	Method of moment
CG	Conjugate gradient algorithm
FFT	Fast Fourier transform
LPC	Local power conservation
VNA	Vector network analyzer

List of Symbols

Symbol	Description
$\boldsymbol{r}$	Position vector to a general observation point
$\boldsymbol{r'}$	Position vector to a general source point
j	Imaginary unit ($j^2 = -1$)
$\boldsymbol{E}$	Electric field intensity
$\boldsymbol{H}$	Magnetic field intensity
$\boldsymbol{p}$	Electric dipole moment
$\boldsymbol{m}$	Magnetic dipole moment
$\boldsymbol{P}$	Electric polarization density
$\boldsymbol{M}$	Magnetic polarization density
$\boldsymbol{J}_e$	Electric current
$\boldsymbol{J}_m$	Magnetic current
$\overline{\overline{\hat{\alpha}}}$	Effective polarizability tensor
$\overline{\overline{\chi}}$	Macroscopic surface-averaged susceptibility tensor
$\overline{\overline{Z}}_{se}$	Surface electric impedance tensor
$\overline{\overline{Y}}_{sm}$	Surface magnetic admittance tensor
$\overline{\overline{K}}_{em}$	Magnetoelectric coupling coefficient tensor
$\overline{\overline{K}}_{me}$	Electromagnetic coupling coefficient tensor
$\boldsymbol{S}^{av}$	Time-average Poynting vector
k_b	Background wavenumber
λ_0	Wavelength in free space
$\mathcal{D}$	Imaging domain
$\mathcal{S}$	Measurement domain

Γ	Enclosure of the MWI system
∇^2	Laplacian operator
w	Contrast source
g	Green's function
H_0^2	Zeroth order Hankel function of the second kind
$O(\boldsymbol{r})$	Contrast's function
Δ	Difference
av	Average

Chapter 1

Introduction

An electromagnetic metasurface (EMS) is an artificial structure with sub-wavelength thickness which can systematically manipulate the electromagnetic behaviors [1–4]. Due to its sub-wavelength thickness, it is considered as a surface or the two-dimensional (2D) form of metamaterials. The behaviors that can be controlled by metasurfaces include radiation patterns [5,6], polarization [7,8], reflection [9], absorption [10], etc. When an incident electromagnetic wave impinges on the metasurface, a set of electric and magnetic polarization currents are induced. These currents will then create a secondary radiation that can change the features of the original incident field [11, 12]. The characteristics of these polarization currents determine the final form of the transmitted and reflected waves. Thus, an EMS can be considered as a transformer for electromagnetic waves. For example, in [13], electromagnetic metasurfaces have been used to transform an incident wave into a transmitting wave that satisfies some desired performance criteria such as a desired half power beamwidth (HPBW), a main beam direction, and null angles.

In order to systematically study the field transformation of metasurfaces, generalized sheet transition conditions, also known as GSTCs, have been developed to describe the electromagnetic field transformation across the metasurface. These boundary conditions were derived by Idemen [14] and have then been applied to the discontinuity of electromagnetic

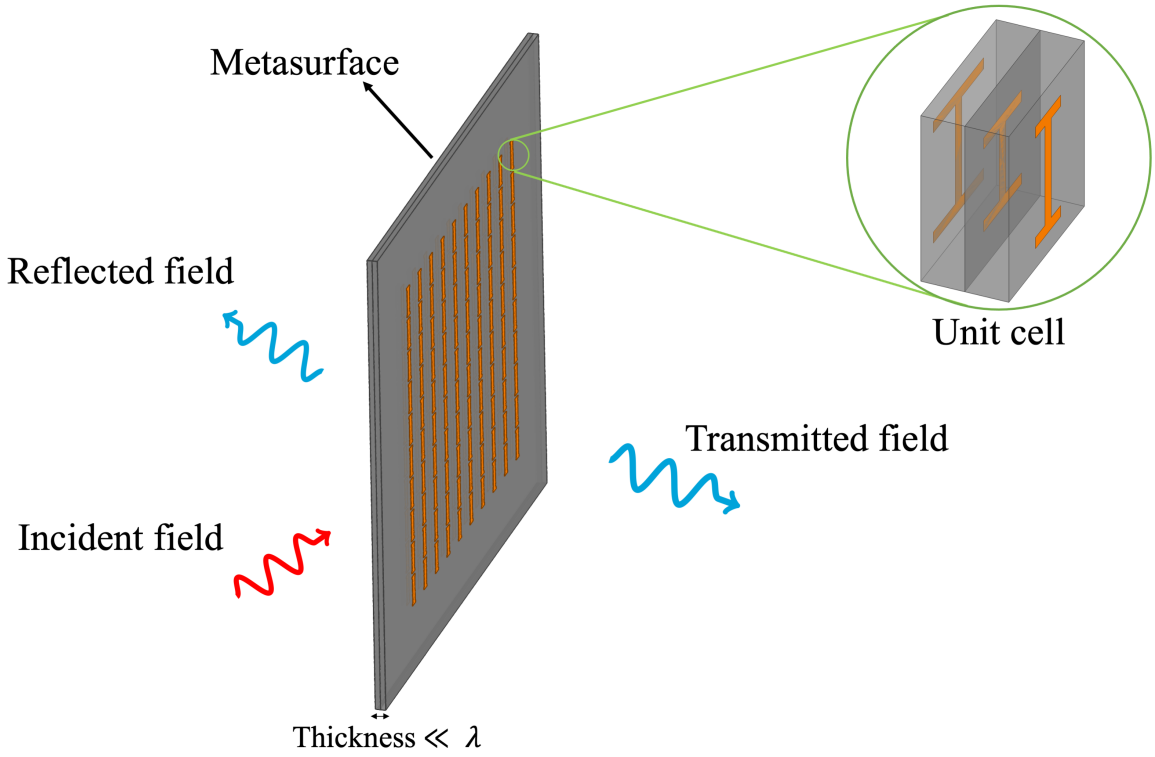

Fig. 1.1: An incident field, shown with a red arrow, impinges on the metasurface. A reflected field and a transmitted field shown in blue arrows arise. The metasurface consists of a set of unit cells with subwavelength dimensions. A common implementation of a unit cell that consists of a three-layer printed circuit board design (PCB) is shown.

fields across metasurfaces [15–18].

As shown in Figure 1.1, a metasurface consists of a lattice of homogenized sub-wavelength unit cells. When these unit cells interact with the incident field, reflected and transmitted fields will arise that can be controlled by the properties of the unit cells [9]. The GSTCs can be described by a set of effective surface parameters. For homogenization, it is required that each unit cell within the metasurface is small enough compared to the wavelength [19]. The GSTCs may then be represented using three different approaches, namely,

- The polarizability model [11, 20]
- The susceptibility model [16, 21]
- The impedance model [1, 22]

We will review all of these three models in Chapter 2, but will then focus on the susceptibility model in later chapters. As will be seen, in all of these models, when we know the electromagnetic fields on both sides of the metasurface, the surface parameters can be systematically computed. In practice, the incidence field on the metasurface is known. Also, in several applications, we would like the reflected field from the metasurface to be zero (reflectionless metasurfaces). However, knowing the fields on the output side of the metasurface may not be straightforward. This is due to the fact that we typically look for some features such as HPBW and main beam direction; consequently, we may not know the exact form of the field on the output face of the metasurface. One approach to handle this situation is to use electromagnetic inversion techniques to mathematically reconstruct the fields on the boundary of the metasurface from the desired performance criteria [13, 23]. In cases where we can write the analytical form of the desired fields on the metasurface, the use of electromagnetic inversion is not needed and we can simply use the GSTCs to design our metasurfaces. In Chapter 4 of this thesis, where we focus on the use of an absorbing metasurface for microwave imaging, we will see an example of this scenario.

Metasurfaces may be classified in different ways. One way is to classify them into mono-anisotropic and bi-anisotropic cases. (These two will be explained in details in Chapter 2.) As will be seen, bi-anisotropic metasurfaces have asymmetric structures and have an extra degree of freedom known as magneto-electric coupling where the electric (magnetic) polarization responses to a magnetic (electric) field [19, 24]. As will be seen, in this thesis, we focus on bi-anisotropic metasurfaces.

Furthermore, metasurfaces can be categorized into active or passive structures. In this work, we will mainly focus on passive metasurfaces. Passive metasurfaces can be either lossy or lossless. We will encounter both lossy and lossless metasurfaces in this thesis. Alternatively, metasurfaces can be classified under reciprocal and non-reciprocal media. Herein, due to the ease of implementation, we focus on reciprocal metasurfaces.

When we find the required surface parameters of the metasurface (e.g., the required

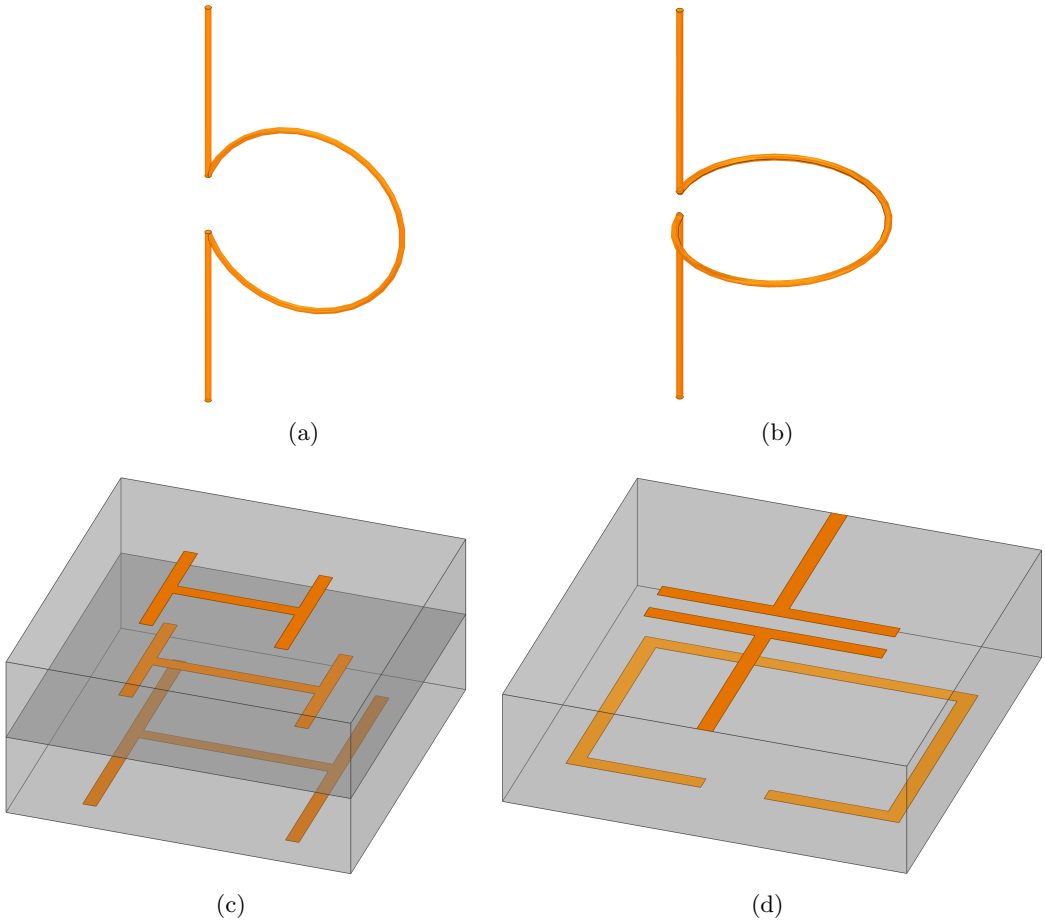

Fig. 1.2: A few unit cell topologies: (a) Omega particle, (b) Chiral particle, (c) stacked-layer dogbone topology, and (d) wire-loop topology.

surface susceptibilities), we need to implement them. As noted above, this is typically done by breaking the surface into different unit cells. As shown in Figure 1.2, each unit cell will then includes designs such as Omega particles, Chiral particles [12], wire-loop structures [1, 25], and stacked-layer dogbone structures [26, 27]. For example, the wire-loop structure consists of wire and loop copper traces printed on dielectric substrates. These wires and loops for each unit cell control the induced electric and magnetic currents [1, 25]. The stacked-layer topology typically consists of three impedance layers printed on two cascaded dielectric substrates [13, 26]. To physically realize the impedance layers, inclusions such as dogbone [24, 26, 28] or spider [29] are used. Geometrical features of these inclusions, e.g.,

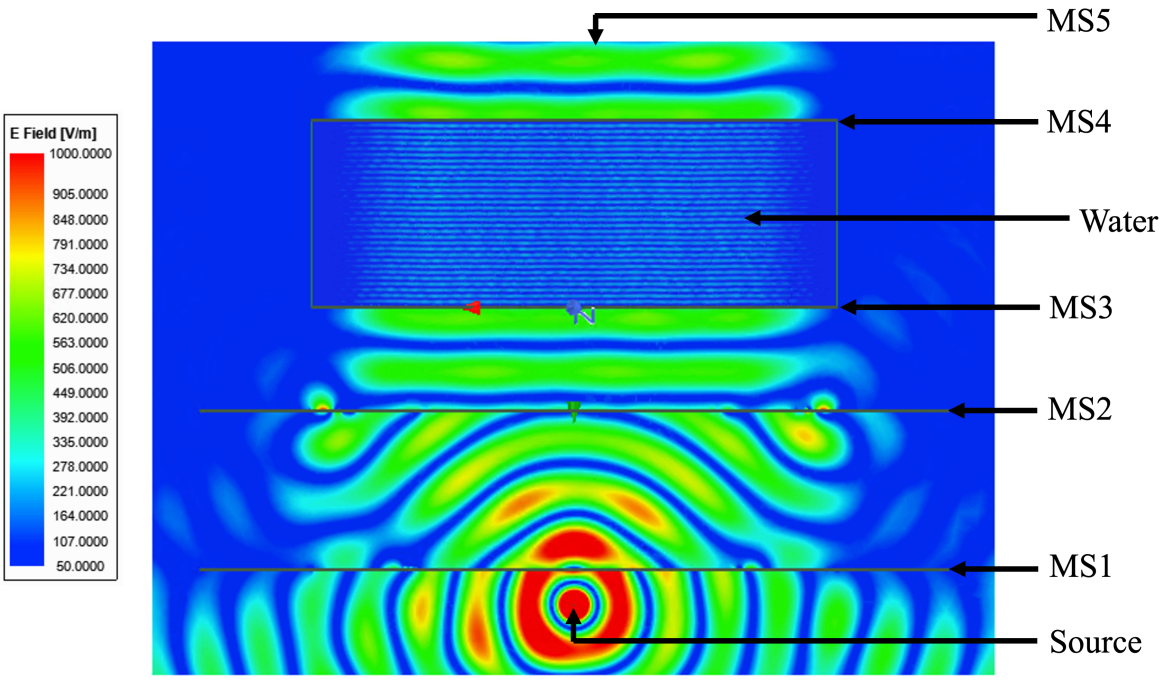

Fig. 1.3: An example of combining the use of three kinds of metasurfaces, which are a cascaded metasurface system (MS1 and MS2) for wavefront shaping, matching metasurfaces (MS3 and MS4) and an absorbing metasurface (MS5). This simulation is a 2D simulation where the source is a line source.

length and width of the dogbone, need to be optimized to obtain the desired performance.

As noted earlier, metasurfaces offer several applications such as wavefront shaping [6, 30–32], perfect absorption [10,33–35], invisibility cloaks [36–39], and polarization control [7, 40, 41]. In Fig. 1.3, we present an example that performs wavefront shaping, impedance matching and absorbing. In this example, the metasurface pair (denoted by MS1 and MS2) converts a cylindrical wavefront to a truncated plane wave.[1] Then, the truncated plane wave propagates from air to a high permittivity medium (water) with minimal reflections via the use of a matching metasurface (MS3). Then, a second matching metasurface (MS4) is used to couple the wave from water to air. Lastly, the plane wave is absorbed by an absorbing metasurface denoted by MS5. In this thesis, we focus on taking advantage of metasurfaces for microwave imaging (MWI). MWI is a non-destructive imaging technique

[1]The design process for wavefront shaping using metasurface pairs can be found in [6, 31]. (The design of this particular metasurface pair was performed by Trevor Brown.)

that reconstructs qualitative or quantitative images of the relative complex permittivity profile of an object of interest (OI) [42–47]. The fundamentals behind MWI will be presented in Chapter 3. As will be seen, in this thesis, we mainly use inverse scattering algorithms that *quantitatively* reconstruct an image of the OI's relative complex permittivity profile. Usually in MWI, a set of transceivers are installed around the OI from different angles. The OI is irradiated by each transmitter, and the resulting scattered fields are collected by the receivers. The scattered fields are then processed by an inverse scattering algorithm. Two common inverse scattering algorithms used in this work are the Gauss-Newton inversion (GNI) [48, 49] and the contrast source inversion (CSI) algorithms [50]. While optimizing, a regularization scheme is used to stabilize the inversion process (i.e., treating the ill-posed problem) [51]. In order to overcome the difficulties of selecting regularization parameters, multiplicative regularization (MR) has been utilized for inverse scattering applications to automatically regularize the problem. Thus, in this thesis, the MR-GNI and MR-CSI algorithms are used to reconstruct the OI's relative complex permittivity profiles [48–50, 52, 53].

1.1 Objectives

The purpose of this thesis is to investigate the use of metasurfaces for the MWI application, and investigate if they can offer certain advantages for performing microwave imaging. Since metasurfaces can tailor electromagnetic fields in different fashions, they can therefore be used for MWI in several different ways. Herein, we consider two different ways that metasurfaces can offer advantages for MWI.

1. In the first case, the use of metasurfaces is proposed as thin metallic-backed microwave absorbers in MWI to reduce reflections from the MWI enclosure while shielding the imaging chamber from external interference. In MWI, casing is needed to contain the coupling liquid and/or mount the transceivers. The inverse scattering algorithms which are used to process the measured scattered field data often assume an infi-

nite background medium. To mimic an infinite background medium, reflections are required to be reduced at the enclosure interface. One approach is to add loss in the coupling liquid. However, the main disadvantage of using lossy coupling liquid is that not only the reflections but also the desired signal level will be reduced. Thus, the metallic-backed absorbing metasurfaces are proposed to be used in MWI (see Chapter 4). The advantages of using absorbing metasurfaces in MWI are that (i) metasurfaces are light and thin which are essential for having a portable MWI system; (ii) metasurfaces can be fabricated using standard PCB technology; and (iii) the metallic-backed feature shields the imaging environment from outside interference. In Chapter 4, three topologies of absorbing metasurface unit cell are considered. Synthetic imaging results are presented to show the promise of using a metasurface enclosure. Finally, an absorbing metasurface using two bonded Rogers substrates are fabricated and experimentally measured.

2. In the second case, the use of metasurfaces as impedance transformers is investigated in MWI to more efficiently couple microwave energy into the target. In MWI, it is required to have sufficient microwave energy interrogating the target. Matching fluids are often used to facilitate this. However, the disadvantages of using matching liquids are that (i) matching fluids must be contained within a chamber and changed regularly, especially for biomedical applications (ii) It may not be feasible for some targets to be immersed in the matching fluid, and (iii) the matching fluids are often lossy, so they negatively affect the signal-to-noise ratio of the measured data. To reduce the necessity of having matching fluids, matching metasurfaces are proposed to be used as impedance transformers to couple the energy into the target. The advantages of using matching metasurfaces in MWI are that (i) they are thin and light weight, which is important for portable MWI systems, and (ii) they are easy to fabricate and cost efficiently. Three metasurface design topologies are proposed in Chapter 5, and one of them is fabricated and measured to verify the performance of the metasurface.

Finally, we note that the above advantages come with its own disadvantages which will be discussed in Chapters 4 and 5.

1.2 Thesis Outline

The outline of this thesis is as follows.

In Chapter 2, the theory of metasurfaces and the associated boundary conditions (GSTCs) based on the three surface models will be discussed. It will be reviewed that the metasurface unit cell can be considered as an equivalent two-port circuit network. By considering the two-port network, the framework of cascaded layer topology design will be studied. Furthermore, the conditions of lossless and reciprocal metasurfaces are also reviewed.

In Chapter 3, the theory of MWI will be discussed. A two-dimensional tomographic MWI with TM_z propagation will be emphasized in this chapter. In particular, the main governing equations of MWI and the main unknown of the problem, which is the relative complex permittivity contrast, are presented.

In Chapter 4, metasurfaces are designed to be thin microwave absorbers for the enclosure of MWI. Firstly, a design framework of absorbing metasurfaces based on effective surface susceptibilities is systematically evaluated. Then, three topologies of absorbing metasurface unit cells are considered to realize the desired surface parameters. Next, the proposed metasurfaces are implemented in the MWI as enclosure, and the scattered field data are collected in a full-wave simulation software, Ansys HFSS. Furthermore, the state-of-the-art inverse scattering algorithms, known as the Gauss-Newton and contrast source inversion algorithms, are used to process the collected scattered data. This chapter concludes with an experimental evaluation of a fabricated metasurface.

In Chapter 5, metasurfaces are proposed to be used as impedance matching transformers in MWI so that we can couple microwave energy directly from air to a high permittivity medium. Firstly, a design framework of matching metasurfaces is outlined in which the

boundary conditions are based on the surface susceptibility model. With the surface parameters, three topologies are designed. Next, a synthetic imaging example with the use of spatial prior information is presented. This chapter concludes with an experimental evaluation study.

In Chapter 6, we present the conclusions of this research and present potential future works of the thesis. There are also a few appendices that provide extra information about some of the topics covered in this thesis.

Chapter 2

Fundamentals of Metasurfaces

Electromagnetic Matesurfaces

An electromagnetic metasurface (EMS) is three-dimensional (3D) artificial structure with sub-wavelength thickness which can provide a means to control electromagnetic field properties [1, 15, 16, 26, 54]. As an incidence electromagnetic wave impinges on the metasurface, a set of electric and magnetic dipole moments are induced on the metasurface. These dipole moments will themselves form a set of electric and magnetic fields [11]. The superposition of the dipoles' fields can determine the final form of the resulting wave.

In order to systematically evaluate the field transformation across the metasurface, metasurfaces are discretized into a set of unit cells. The dimension of the unit cell is small compared to the wavelength λ [19], e.g., about $\lambda/6$ or $\lambda/10$. Let us begin by assuming a time dependency of $\exp(j\omega t)$ where $j^2 = -1$, ω is the angular frequency, and t is time. In addition, we denote the permittivity and permeability of free space with ε_0 and μ_0 respectively. Assume that we have a metasurface that is located on $x = 0$ plane in free space. The input and output sides of the metasurfaces are denoted by $x = 0^-$, and $x = 0^+$ respectively as shown in Fig. 2.1. Due to the discontinuity provided by the metasurface, we write the volumetric electric and magnetic polarization density vectors

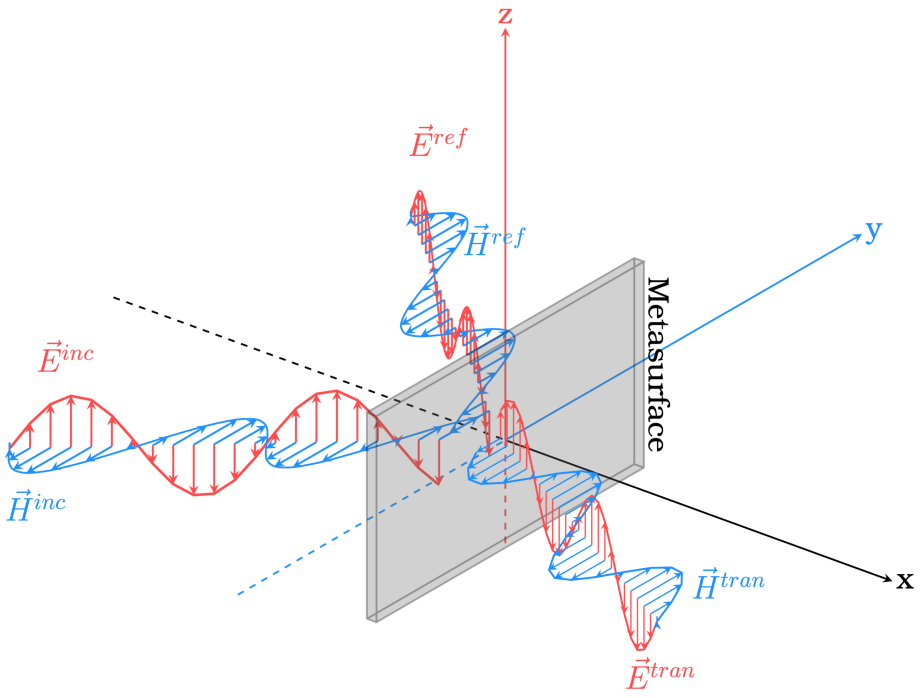

Fig. 2.1: A metasurface is located on the $x = 0$ plane. The input and output sides of the metasurface are $x = 0^-$ and $x = 0^+$ respectively. An arbitrary incident wave illuminated the metasurface, and propagate along $+\hat{x}$ direction. The metasurface is located in free space.

respectively as [16–18]

$$\boldsymbol{P} = \boldsymbol{P}_0 + \boldsymbol{P}_s\delta(x) \tag{2.1a}$$

$$\boldsymbol{M} = \boldsymbol{M}_0 + \boldsymbol{M}_s\delta(x) \tag{2.1b}$$

where the Dirac delta function $\delta(x)$ represents the discontinuity (jump) when passing through the metasurface, $\boldsymbol{P}_0$ and $\boldsymbol{M}_0$ represents the volumetric polarization density vectors and $\boldsymbol{P}_s$ and $\boldsymbol{M}_s$ represents the surface polarization density vectors. Therefore, we can write the electric flux density $\boldsymbol{D}$ and the magnetic flux density $\boldsymbol{B}$ as

$$\boldsymbol{D} = \varepsilon_0\boldsymbol{E} + \boldsymbol{P} \quad \Longrightarrow \quad \boldsymbol{E} = \frac{\boldsymbol{D} - \boldsymbol{P}_0 - \boldsymbol{P}_s\delta(x)}{\varepsilon_0} \tag{2.2a}$$

$$\boldsymbol{B} = \mu_0\boldsymbol{H} + \mu_0\boldsymbol{M} \quad \Longrightarrow \quad \boldsymbol{H} = \frac{\boldsymbol{B}}{\mu_0} - \boldsymbol{M}_0 - \boldsymbol{M}_s\delta(x) \tag{2.2b}$$

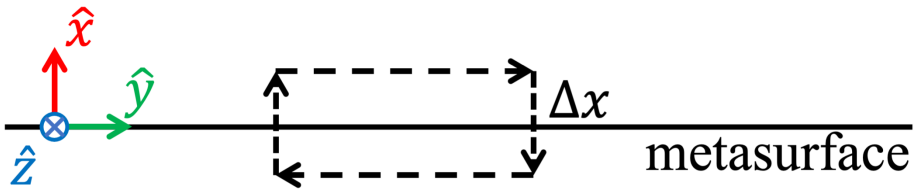

Fig. 2.2: Pillbox across the metasurface boundary with thickness of $\Delta x \to 0$. The pillbox has created to obtain the required tangential boundary conditions.

where $\boldsymbol{E}$ and $\boldsymbol{H}$ denote the electric and magnetic intensity vectors. We can then substitute the above equations in the following Maxwell's curl equations

$$\nabla \times \boldsymbol{E} = -j\omega\boldsymbol{B} - \boldsymbol{J}_{\mathrm{m},i} \tag{2.3a}$$

$$\nabla \times \boldsymbol{H} = j\omega\boldsymbol{D} + \boldsymbol{J}_{\mathrm{e},i} \tag{2.3b}$$

where $\boldsymbol{J}_{\mathrm{e},i}$ and $\boldsymbol{J}_{\mathrm{m},i}$ are impressed currents and '$\nabla\times$' denotes the curl operator. Then, similar to the derivation of the typical electromagnetic tangential boundary conditions, we can use the curl equations in conjunction with the Stokes' theorem and perform integration over a pillbox shown in Fig. 2.2. Letting the thickness of the pillbox, denoted by Δx, go to zero, we arrive at the following equations [15–18]

$$\hat{n} \times \left(\boldsymbol{H}_t^+ - \boldsymbol{H}_t^-\right) = j\omega\boldsymbol{P}_t - \hat{n} \times \nabla_t \boldsymbol{M}_n + \boldsymbol{J}_{\mathrm{e},i,t} \tag{2.4a}$$

$$\left(\boldsymbol{E}_t^+ - \boldsymbol{E}_t^-\right) \times \hat{n} = j\omega\mu_0\boldsymbol{M}_t - \nabla_t\left(\frac{\boldsymbol{P}_n}{\varepsilon_0}\right) \times \hat{n} + \boldsymbol{J}_{\mathrm{m},i,t} \tag{2.4b}$$

where

- $\hat{n}$ is the normal vector, which is equal to $\hat{x}$ for the metasurface shown in Fig. 2.2.
- The superscript '$-$' represents the fields at $x = 0^-$ side, and the superscript '$+$' represents the fields at the $x = 0^+$ side.
- The subscript 't' denotes the tangential component. Therefore, $\boldsymbol{H}_t^+$ represents the

tangential magnetic field on the $x = 0^+$ side of the metasurface.

- $\boldsymbol{P}_t$ and $\boldsymbol{M}_t$ represent the tangential components of $\boldsymbol{P}_s$ and $\boldsymbol{M}_s$ respectively.

- $\boldsymbol{P}_n$ and $\boldsymbol{M}_n$ represent the normal components of $\boldsymbol{P}_s$ and $\boldsymbol{M}_s$ respectively.

- ∇_t denotes the tangential gradient operator. For example, for the metasurface shown in Fig. 2.2, we have $\nabla_t = \frac{\partial}{\partial y}\hat{y} + \frac{\partial}{\partial z}\hat{z}$.

- $\boldsymbol{J}_{\mathrm{e},i,t}$ and $\boldsymbol{J}_{\mathrm{m},i,t}$ denote the tangential components of the impressed electric and magnetic currents over the metasurface.

The equations presented in (2.4) are referred to as the generalized sheet transition conditions (GSTCs) which govern how the electromagnetic waves interact with metasurfaces. As metasurfaces are ultra-thin structures (compared to the wavelength), normal polarizations are typically ignored for simplicity [16]. Thus, the two equations in (2.4) are simplified as

$$\hat{n} \times \left(\boldsymbol{H}_t^+ - \boldsymbol{H}_t^-\right) \;=\; j\omega \boldsymbol{P}_t + \boldsymbol{J}_{\mathrm{e},i,t} \tag{2.5a}$$

$$\left(\boldsymbol{E}_t^+ - \boldsymbol{E}_t^-\right) \times \hat{n} \;=\; j\omega\mu_0 \boldsymbol{M}_t + \boldsymbol{J}_{\mathrm{m},i,t} \tag{2.5b}$$

Since this thesis does not consider active metasurfaces, we also set the impressed currents to zero and arrive at

$$\hat{n} \times \left(\boldsymbol{H}_t^+ - \boldsymbol{H}_t^-\right) \;=\; j\omega \boldsymbol{P}_t \tag{2.6a}$$

$$\left(\boldsymbol{E}_t^+ - \boldsymbol{E}_t^-\right) \times \hat{n} \;=\; j\omega\mu_0 \boldsymbol{M}_t \tag{2.6b}$$

In the following, (2.6) will be presented in terms of three models, which are surface polarizabilities [20, 55], surface susceptibilities [16, 21], and surface impedances [1, 22].

2.1 Polarizability Model

The polarizability model describes the ability of the metasurface to form electric and magnetic dipole moments when illuminated by the incident field $(\boldsymbol{E}^{\text{inc}}, \boldsymbol{H}^{\text{inc}})$. Under some assumptions, the tangential electric and magnetic dipole moments, denoted by $\boldsymbol{p}_t$ and $\boldsymbol{m}_t$, can be written as [10, 11]

$$\begin{bmatrix} \boldsymbol{p}_t \\ \boldsymbol{m}_t \end{bmatrix} = \begin{bmatrix} \overline{\overline{\hat{\alpha}}}_{\text{ee}} & \overline{\overline{\hat{\alpha}}}_{\text{em}} \\ \overline{\overline{\hat{\alpha}}}_{\text{me}} & \overline{\overline{\hat{\alpha}}}_{\text{mm}} \end{bmatrix} \begin{bmatrix} \boldsymbol{E}_t^{\text{inc}} \\ \boldsymbol{H}_t^{\text{inc}} \end{bmatrix} \tag{2.7}$$

where $\boldsymbol{E}_t^{\text{inc}}$ and $\boldsymbol{H}_t^{\text{inc}}$ are the tangential electric and magnetic incident fields on the metasurface. In addition, $\overline{\overline{\hat{\alpha}}}_{\text{ee}}$, $\overline{\overline{\hat{\alpha}}}_{\text{em}}$, $\overline{\overline{\hat{\alpha}}}_{\text{me}}$, and $\overline{\overline{\hat{\alpha}}}_{\text{mm}}$ are the effective surface electric-to-electric, magnetic-to-electric, electric-to-magnetic, and magnetic-to-magnetic polarizabilities [11,55].

To obtain $\boldsymbol{P}_t$ and $\boldsymbol{M}_t$ in (2.6), we can use $\boldsymbol{P}_t = \boldsymbol{p}_t/S$ and $\boldsymbol{M}_t = \boldsymbol{m}_t/S$ where S is the area of a unit cell. Therefore, (2.6) with the help of (2.7) can be written as

$$\hat{n} \times \left(\boldsymbol{H}_t^+ - \boldsymbol{H}_t^-\right) = j\omega\left(\frac{\overline{\overline{\hat{\alpha}}}_{\text{ee}}}{S}\, \boldsymbol{E}_t^{\text{inc}} + \frac{\overline{\overline{\hat{\alpha}}}_{\text{em}}}{S} \boldsymbol{H}_t^{\text{inc}}\right) \tag{2.8a}$$

$$\left(\boldsymbol{E}_t^+ - \boldsymbol{E}_t^-\right) \times \hat{n} = j\omega\mu_0\left(\frac{\overline{\overline{\hat{\alpha}}}_{\text{mm}}}{S} \boldsymbol{H}_t^{\text{inc}} + \frac{\overline{\overline{\hat{\alpha}}}_{\text{me}}}{S}\, \boldsymbol{E}_t^{\text{inc}}\right) \tag{2.8b}$$

In addition, it can be shown that [56, Appendix C] [11]

$$\boldsymbol{E}_t^{\text{av}} = \boldsymbol{E}_t^{\text{inc}} - \frac{j\omega\eta_0}{2}\boldsymbol{P}_t \tag{2.9a}$$

$$\boldsymbol{H}_t^{\text{av}} = \boldsymbol{H}_t^{\text{inc}} - \frac{j\omega}{2\eta_0}\boldsymbol{M}_t \tag{2.9b}$$

where $\eta_0 = 120\pi$ and $\boldsymbol{E}_t^{\text{av}}$ and $\boldsymbol{H}_t^{\text{av}}$ are the averaged fields defined as

$$\boldsymbol{E}_t^{\text{av}} = \frac{\boldsymbol{E}_t^+ + \boldsymbol{E}_t^-}{2} \tag{2.10}$$

$$\boldsymbol{H}_t^{\text{av}} = \frac{\boldsymbol{H}_t^+ + \boldsymbol{H}_t^-}{2} \tag{2.11}$$

Based on (2.9), we can re-write (2.8) as an equation that only contain the difference between the tangential fields, the averaged of the tangential fields, and the effective surface polarizabilities. The expression for this final form can be found in [19, 57].

2.2 Susceptibility Model

In the surface susceptibility model, we write the surface polarization density vectors in (2.6) as [16, 17]

$$\boldsymbol{P}_t \;=\; \varepsilon_0 \overline{\overline{\chi}}_{\mathrm{ee}} \boldsymbol{E}_t^{\mathrm{av}} \;+\; \frac{1}{c_0} \overline{\overline{\chi}}_{\mathrm{em}} \boldsymbol{H}_t^{\mathrm{av}} \tag{2.12a}$$

$$\boldsymbol{M}_t \;=\; \overline{\overline{\chi}}_{\mathrm{mm}} \boldsymbol{H}_t^{\mathrm{av}} \;+\; \frac{1}{\eta_0} \overline{\overline{\chi}}_{\mathrm{me}} \boldsymbol{E}_t^{\mathrm{av}} \tag{2.12b}$$

where c_0 denotes the velocity of light in free space and $\overline{\overline{\chi}}_{\mathrm{ee}}$, $\overline{\overline{\chi}}_{\mathrm{mm}}$, $\overline{\overline{\chi}}_{\mathrm{em}}$, and $\overline{\overline{\chi}}_{\mathrm{me}}$ are electric (or electric-to-electric), magnetic (or magnetic-to-magnetic), magnetic-to-electric and electric-to-magnetic surface susceptibility tensors, respectively. Therefore, the GSTCs in (2.6) will become

$$\hat{n} \times \left(\boldsymbol{H}_t^{+} - \boldsymbol{H}_t^{-} \right) \;=\; j\omega (\varepsilon_0 \overline{\overline{\chi}}_{\mathrm{ee}} \boldsymbol{E}_t^{\mathrm{av}} \;+\; \frac{1}{c_0} \overline{\overline{\chi}}_{\mathrm{em}} \boldsymbol{H}_t^{\mathrm{av}}) \tag{2.13a}$$

$$\left(\boldsymbol{E}_t^{+} - \boldsymbol{E}_t^{-} \right) \times \hat{n} \;=\; j\omega\mu_0 (\overline{\overline{\chi}}_{\mathrm{mm}} \boldsymbol{H}_t^{\mathrm{av}} \;+\; \frac{1}{\eta_0} \overline{\overline{\chi}}_{\mathrm{me}} \boldsymbol{E}_t^{\mathrm{av}}) \tag{2.13b}$$

To make an example, let us assume that the metasurface is located on the $x = 0$ plane as shown in Fig. 2.1. Therefore, (2.13) can be written as [16, 58]

$$\begin{bmatrix} -\Delta H_z \\ \Delta H_y \end{bmatrix} = j\omega\varepsilon_0 \begin{bmatrix} \chi_{\mathrm{ee}}^{yy} & \chi_{\mathrm{ee}}^{yz} \\ \chi_{\mathrm{ee}}^{zy} & \chi_{\mathrm{ee}}^{zz} \end{bmatrix} \begin{bmatrix} E_y^{\mathrm{av}} \\ E_z^{\mathrm{av}} \end{bmatrix} + j\omega\sqrt{\mu_0\varepsilon_0} \begin{bmatrix} \chi_{\mathrm{em}}^{yy} & \chi_{\mathrm{em}}^{yz} \\ \chi_{\mathrm{em}}^{zy} & \chi_{\mathrm{em}}^{zz} \end{bmatrix} \begin{bmatrix} H_y^{\mathrm{av}} \\ H_z^{\mathrm{av}} \end{bmatrix} \tag{2.14a}$$

$$\begin{bmatrix} \Delta E_z \\ -\Delta E_y \end{bmatrix} = j\omega\mu_0 \begin{bmatrix} \chi_{\mathrm{mm}}^{yy} & \chi_{\mathrm{mm}}^{yz} \\ \chi_{\mathrm{mm}}^{zy} & \chi_{\mathrm{mm}}^{zz} \end{bmatrix} \begin{bmatrix} H_y^{\mathrm{av}} \\ H_z^{\mathrm{av}} \end{bmatrix} + j\omega\sqrt{\mu_0\varepsilon_0} \begin{bmatrix} \chi_{\mathrm{me}}^{yy} & \chi_{\mathrm{me}}^{yz} \\ \chi_{\mathrm{me}}^{zy} & \chi_{\mathrm{me}}^{zz} \end{bmatrix} \begin{bmatrix} E_y^{\mathrm{av}} \\ E_z^{\mathrm{av}} \end{bmatrix} \tag{2.14b}$$

In the above GSTCs, the position vector $\boldsymbol{r}$, which shows a given unit cell location, has been

dropped for brevity. For a given location $\boldsymbol{r}$ on the metasurface:

— Δu where $u \in \{E_y, E_z, H_y, H_z\}$ represents the difference of the tangential fields on input and output sides of the metasurface (i.e., $\Delta u = u^+ - u^-$).

— As noted before, u_{av} is the algebraic average of the tangential fields on both sides (i.e., $u_{\text{av}} = (u^+ + u^-)/2$).

— The first subscript and superscript of the surface susceptibilities represents field response in corresponding direction, and second subscript and superscript represents field excitation in a given location, respectively.

  – For example, consider χ_{me}^{yz}: it represents how an electric field excitation in the z direction (i.e., second subscript and superscript) creates a magnetic polarization response in the y direction (first subscript and superscript).

  – As another example, consider χ_{ee}^{yy}: it represents how an electric field excitation in the y direction (i.e., second subscript and superscript) creates an electric polarization response in the y direction (first subscript and superscript).

As an example, consider the non-gyrotropy assumption for our metasurface located on $x = 0$ plane which requires [24]

$$\chi_{\text{ee}}^{yz} = \chi_{\text{ee}}^{zy} = 0 \tag{2.15a}$$

$$\chi_{\text{mm}}^{yz} = \chi_{\text{mm}}^{zy} = 0 \tag{2.15b}$$

$$\chi_{\text{em}}^{zz} = \chi_{\text{em}}^{yy} = 0 \tag{2.15c}$$

$$\chi_{\text{me}}^{zz} = \chi_{\text{me}}^{yy} = 0 \tag{2.15d}$$

Under the assumption of (2.15), (2.14) simplifies to

$$-\Delta H_z = j\omega\varepsilon_0\chi_{\text{ee}}^{yy}E_y^{\text{av}} + j\omega\sqrt{\varepsilon_0\mu_0}\chi_{\text{em}}^{yz}H_z^{\text{av}} \tag{2.16a}$$

$$\Delta H_y = j\omega\varepsilon_0\chi_{\text{ee}}^{zz}E_z^{\text{av}} + j\omega\sqrt{\varepsilon_0\mu_0}\chi_{\text{em}}^{zy}H_y^{\text{av}} \tag{2.16b}$$

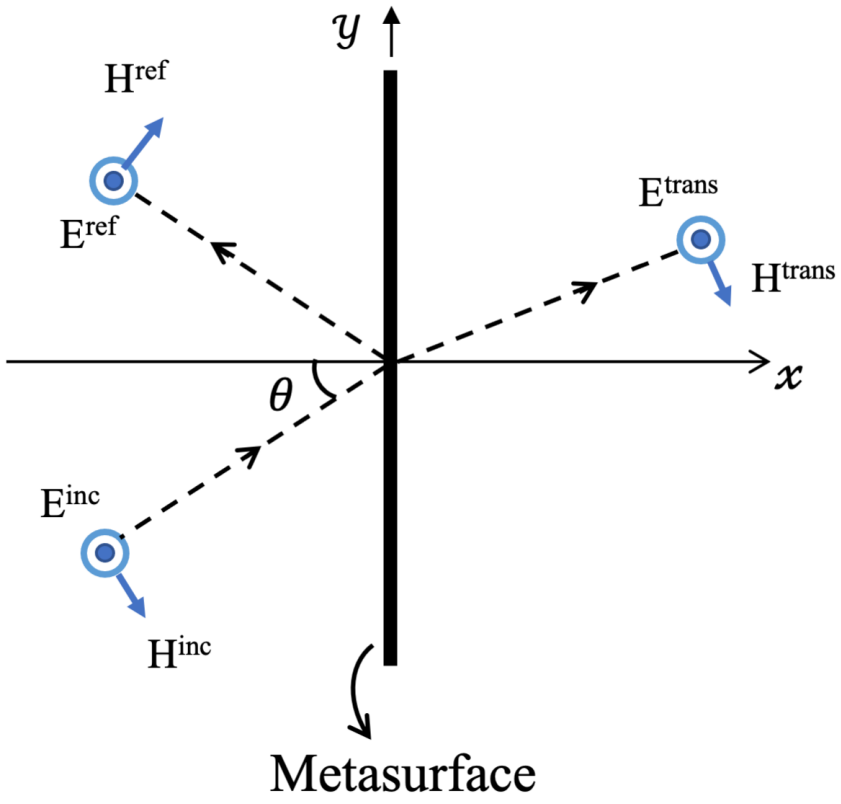

Fig. 2.3: A metasurface is located on the y axis. Thus, the input and output sides of the metasurface are $x = 0^-$ and $x = 0^+$ respectively. A TE (TM_z) incident wave illuminates the metasurface which results in reflected and transmitted waves. Reprinted, with permission, from [59]

$$\Delta E_z = j\omega\mu_0\chi_{\mathrm{mm}}^{yy}H_y^{\mathrm{av}} + j\omega\sqrt{\varepsilon_0\mu_0}\chi_{\mathrm{me}}^{yz}E_z^{\mathrm{av}} \tag{2.16c}$$

$$-\Delta E_y = j\omega\mu_0\chi_{\mathrm{mm}}^{zz}H_z^{\mathrm{av}} + j\omega\sqrt{\varepsilon_0\mu_0}\chi_{\mathrm{me}}^{zy}E_y^{\mathrm{av}} \tag{2.16d}$$

As another example, we can consider a two-dimensional (2D) transverse electric (TE) wave impinges on a metasurface along $x = 0$ plane as shown in Fig. 2.3.[1] Due to the assumption of the TE case, we have the following field components: E_z, H_x, and H_y.

[1] In microwave imaging, this polarization is sometimes referred to as transverse magnetic with respect to the z direction (TM_z).

Therefore, the GSTCs shown in (2.13) for the TE case will be

$$\Delta H_y \;=\; j\omega\varepsilon_0\chi_{\rm ee}^{zz}\; E_z^{\rm av} + j\omega\sqrt{\varepsilon_0\mu_0}\chi_{\rm em}^{zy}H_y^{\rm av} \tag{2.17a}$$

$$\Delta E_z \;=\; j\omega\mu_0\chi_{\rm mm}^{yy}H_y^{\rm av} + j\omega\sqrt{\varepsilon_0\mu_0}\chi_{\rm me}^{yz}E_z^{\rm av} \tag{2.17b}$$

Similarly for the TM case incidence mode, the GSTCs can be written as

$$-\Delta H_z \;=\; j\omega\varepsilon_0\chi_{\rm ee}^{yy}\; E_y^{\rm av} + j\omega\sqrt{\varepsilon_0\mu_0}\chi_{\rm em}^{yz}H_z^{\rm av} \tag{2.18a}$$

$$-\Delta E_y \;=\; j\omega\mu_0\chi_{\rm mm}^{zz}H_z^{\rm av} + j\omega\sqrt{\varepsilon_0\mu_0}\chi_{\rm me}^{zy}E_y^{\rm av} \tag{2.18b}$$

The relation between the surface polarizabilities and the surface susceptibilies can be obtained; see [4, 57] for the derivation. Finally, note that there are different forms of bianisotropic media. For example, an Omega-bianisotropic medium requires [4, 60]

$$\overline{\overline{\chi}}_{\rm em} = -\overline{\overline{\chi}}_{\rm me}^{T} = \begin{bmatrix} 0 & \chi_{\rm em}^{yz} \\ -\chi_{\rm em}^{yz} & 0 \end{bmatrix} \tag{2.19}$$

Conceptually, the Omega-bianisotropy means that an acting electric field creates a magnetic current that is perpendicular to the acting electric field, and similarly an acting magnetic field creates an electric current that is perpendicular to the acting magnetic field [17, 61].

2.3 Impedance Model

The impedance model relates the averaged tangential fields to the equivalent electric and magnetic surface currents denoted by $\boldsymbol{J}_{{\rm e},s}$ and $\boldsymbol{J}_{{\rm m},s}$ as [26, 61]

$$\boldsymbol{E}_t^{\rm av} \;=\; \overline{\overline{Z}}_{\rm se}\; \boldsymbol{J}_{{\rm e},s} \;+\; \overline{\overline{K}}_{\rm em}\,(\boldsymbol{J}_{{\rm m},s} \;\times \hat{n}) \tag{2.20a}$$

$$\boldsymbol{H}_t^{\rm av} \;=\; \overline{\overline{Y}}_{\rm sm}\; \boldsymbol{J}_{{\rm m},s} \;+\; \overline{\overline{K}}_{\rm me}\,(\hat{n} \;\times\; \boldsymbol{J}_{{\rm e},s}) \tag{2.20b}$$

where $\overline{\overline{Z}}_{\rm se}$ is the surface electric impedance, $\overline{\overline{Y}}_{\rm sm}$ is the surface magnetic admittance, $\overline{\overline{K}}_{\rm em}$ is the magnetoelectric coupling coefficient and $\overline{\overline{K}}_{\rm me}$ is the electromagnetic coupling coefficient. In addition, the surface equivalent currents can be written as

$$\boldsymbol{J}_{{\rm e},s} \;=\; \hat{n} \times \left(\boldsymbol{H}_t^{+} - \boldsymbol{H}_t^{-}\right) \tag{2.21a}$$

$$\boldsymbol{J}_{{\rm m},s} \;=\; \left(\boldsymbol{E}_t^{+} - \boldsymbol{E}_t^{-}\right) \times \hat{n} \tag{2.21b}$$

Therefore, using (2.21), (2.20) can be written as

$$\boldsymbol{E}_t^{\rm av} \;=\; \overline{\overline{Z}}_{\rm se}\left(\hat{n} \times \left(\boldsymbol{H}_t^{+} - \boldsymbol{H}_t^{-}\right)\right) \;+\; \overline{\overline{K}}_{\rm em}\left(\left(\left(\boldsymbol{E}_t^{+} - \boldsymbol{E}_t^{-}\right) \times \hat{n}\right) \;\times \hat{n}\right) \tag{2.22a}$$

$$\boldsymbol{H}_t^{\rm av} \;=\; \overline{\overline{Y_{\rm sm}}}\left(\left(\boldsymbol{E}_t^{+} - \boldsymbol{E}_t^{-}\right) \times \hat{n}\right) \;+\; \overline{\overline{K}}_{\rm me}\left(\hat{n} \;\times\; \left(\hat{n} \times \left(\boldsymbol{H}_t^{+} - \boldsymbol{H}_t^{-}\right)\right)\right) \tag{2.22b}$$

Also, note that

$$\left(\left(\boldsymbol{E}_t^{+} - \boldsymbol{E}_t^{-}\right) \times \hat{n}\right) \times \hat{n} = -\left(\boldsymbol{E}_t^{+} - \boldsymbol{E}_t^{-}\right) \tag{2.23a}$$

$$\hat{n} \times \left(\hat{n} \times \left(\boldsymbol{H}_t^{+} - \boldsymbol{H}_t^{-}\right)\right) = -\left(\boldsymbol{H}_t^{+} - \boldsymbol{H}_t^{-}\right) \tag{2.23b}$$

Substituting (2.23) into (2.22), the general form of GSTCs based on impedance model can be expressed as [25, 26]

$$\boldsymbol{E}_t^{\rm av} \;=\; \overline{\overline{Z}}_{\rm se}\left(\hat{n} \times \left(\boldsymbol{H}_t^{+} - \boldsymbol{H}_t^{-}\right) \;-\; \overline{\overline{K}}_{\rm em}\left(\boldsymbol{E}_t^{+} - \boldsymbol{E}_t^{-}\right)\right. \tag{2.24a}$$

$$\boldsymbol{H}_t^{\rm av} \;=\; \overline{\overline{Y}}_{\rm sm}\left(\left(\boldsymbol{E}_t^{+} - \boldsymbol{E}_t^{-}\right) \;\times \hat{n}\right) \;-\; \overline{\overline{K}}_{\rm me}\left(\boldsymbol{H}_t^{+} - \boldsymbol{H}_t^{-}\right) \tag{2.24b}$$

For our metasurface on the $x = 0$ plane, we can write the above equation as

$$\begin{bmatrix} E_y^{\rm av} \\ E_z^{\rm av} \end{bmatrix} = \begin{bmatrix} Z_{\rm se}^{yy} & Z_{\rm se}^{yz} \\ Z_{\rm se}^{zy} & Z_{\rm se}^{zz} \end{bmatrix} \begin{bmatrix} -\Delta H_z \\ \Delta H_y \end{bmatrix} - \begin{bmatrix} K_{\rm em}^{yy} & K_{\rm em}^{yz} \\ K_{\rm em}^{zy} & K_{\rm em}^{zz} \end{bmatrix} \begin{bmatrix} \Delta E_y \\ \Delta E_z \end{bmatrix} \tag{2.25a}$$

$$\begin{bmatrix} H_y^{\text{av}} \\ H_z^{\text{av}} \end{bmatrix} = \begin{bmatrix} Y_{\text{sm}}^{yy} & Y_{\text{sm}}^{yz} \\ Y_{\text{sm}}^{zy} & Y_{\text{sm}}^{zz} \end{bmatrix} \begin{bmatrix} \Delta E_z \\ -\Delta E_y \end{bmatrix} - \begin{bmatrix} K_{\text{me}}^{yy} & K_{\text{me}}^{yz} \\ K_{\text{me}}^{zy} & K_{\text{me}}^{zz} \end{bmatrix} \begin{bmatrix} \Delta H_y \\ \Delta H_z \end{bmatrix} \tag{2.25b}$$

In the case of Omega-bianisotropic metasurfaces, we have [61]

$$Z_{\text{se}}^{yz} = Z_{\text{se}}^{zy} = 0 \tag{2.26a}$$

$$Y_{\text{sm}}^{yz} = Y_{\text{sm}}^{zy} = 0 \tag{2.26b}$$

$$K_{\text{em}}^{yz} = K_{\text{em}}^{zy} = 0 \tag{2.26c}$$

$$K_{\text{me}}^{yz} = K_{\text{me}}^{zy} = 0 \tag{2.26d}$$

Under the assumption of (2.26), (2.25) simplifies to

$$E_z^{\text{av}} = Z_{\text{se}}^{zz}\Delta H_y - K_{\text{em}}^{zz}\Delta E_z \tag{2.27a}$$

$$E_y^{\text{av}} = -Z_{\text{se}}^{yy}\Delta H_z - K_{\text{em}}^{yy}\Delta E_y \tag{2.27b}$$

$$H_z^{\text{av}} = -Y_{\text{sm}}^{zz}\Delta E_y - K_{\text{me}}^{zz}\Delta H_z \tag{2.27c}$$

$$H_y^{\text{av}} = Y_{\text{sm}}^{yy}\Delta E_z - K_{\text{me}}^{yy}\Delta H_y \tag{2.27d}$$

As another example, we can consider a two-dimensional (2D) TE wave impinges on a metasurface along $x = 0$ plane as shown in Fig. 2.3. Due to the assumption of the TE case, we have the following field components: E_z, H_x, and H_y. Therefore, the GSTCs shown in (2.25) for the TE case will be

$$E_z^{\text{av}} = Z_{\text{se}}^{zz}\Delta H_y - K_{\text{em}}^{zz}\Delta E_z \tag{2.28a}$$

$$H_y^{\text{av}} = Y_{\text{sm}}^{yy}\Delta E_z - K_{\text{me}}^{yy}\Delta H_y \tag{2.28b}$$

Similarly for the TM case, the GSTCs can be written as

$$E_y^{\text{av}} = -Z_{\text{se}}^{yy}\Delta H_z - K_{\text{em}}^{yy}\Delta E_y \tag{2.29a}$$

$$H_z^{\rm av} \;=\; -Y_{\rm sm}^{zz}\Delta E_y \;-\; K_{\rm me}^{zz}\Delta H_z \tag{2.29b}$$

Finally, we note that the the surface susceptibility and the impedance model are related. To this end, let us start with the GSTCs based on the surface susceptibility model, and write (2.13) as

$$\boldsymbol{J}_{{\rm e},s} \;=\; j\omega\varepsilon_0\overline{\overline{\chi}}_{\rm ee}\boldsymbol{E}_t^{\rm av} \;+\; j\omega\sqrt{\varepsilon_0\mu_0}\overline{\overline{\chi}}_{\rm em}\boldsymbol{H}_t^{\rm av} \tag{2.30a}$$

$$\boldsymbol{J}_{{\rm m},s} = \; j\omega\mu_0\overline{\overline{\chi}}_{\rm mm}\boldsymbol{H}_t^{\rm av} \;+\; j\omega\sqrt{\varepsilon_0\mu_0}\overline{\overline{\chi}}_{\rm me}\boldsymbol{E}_t^{\rm av} \tag{2.30b}$$

where $\boldsymbol{J}_{{\rm e},s}$ and $\boldsymbol{J}_{{\rm m},s}$ are the surface electric and magnetic currents. For brevity of notation, let us assume $\bar{\bar{A}} \;=\; j\omega\varepsilon_0\overline{\overline{\chi}}_{\rm ee}$, $\bar{\bar{B}} \;=\; j\omega\sqrt{\varepsilon_0\mu_0}\overline{\overline{\chi}}_{\rm em}$, $\bar{\bar{C}} \;=\; j\omega\sqrt{\varepsilon_0\mu_0}\overline{\overline{\chi}}_{\rm me}$, and $\bar{\bar{D}} \;=\; j\omega\mu_0\overline{\overline{\chi}}_{\rm mm}$. By manipulating (2.30), the average electric and magnetic fields can be expressed by the surface currents as shown below. (The details can be found in Appendix A.)

$$\boldsymbol{E}_t^{\rm av} \;=\; (\bar{\bar{A}} \;-\; \bar{\bar{B}}\bar{\bar{D}}^{-1}\bar{\bar{C}})^{-1}\boldsymbol{J}_{{\rm e},s} \;-\; (\bar{\bar{A}} \;-\; \bar{\bar{B}}\bar{\bar{D}}^{-1}\bar{\bar{C}})^{-1}\bar{\bar{B}}\bar{\bar{D}}^{-1}\boldsymbol{J}_{{\rm m},s} \tag{2.31a}$$

$$\boldsymbol{H}_t^{\rm av} \;=\; (\bar{\bar{A}}\bar{\bar{C}}^{-1}\bar{\bar{D}} \;-\; \bar{\bar{B}})^{-1}\bar{\bar{A}}\bar{\bar{C}}^{-1}\boldsymbol{J}_{{\rm m},s} \;-\; (\bar{\bar{A}}\bar{\bar{C}}^{-1}\bar{\bar{D}} \;-\; \bar{\bar{B}})^{-1}\boldsymbol{J}_{{\rm e},s} \tag{2.31b}$$

Finally, by comparing (2.31) with (2.20), the relation between the surface susceptibility and impedance models can be obtained as

$$\overline{\overline{Z}}_{\rm se} = (\bar{\bar{A}} \;-\; \bar{\bar{B}}\bar{\bar{D}}^{-1}\bar{\bar{C}})^{-1}$$

$$\overline{\overline{Y}}_{\rm sm} = (\bar{\bar{A}}\bar{\bar{C}}^{-1}\bar{\bar{D}} \;-\; \bar{\bar{B}})^{-1}\bar{\bar{A}}\bar{\bar{C}}^{-1}$$

$$\begin{bmatrix} K_{\rm em}^{yz} & -K_{\rm em}^{yy} \\ K_{\rm em}^{zz} & -K_{\rm em}^{zy} \end{bmatrix} = (\bar{\bar{A}} - \bar{\bar{B}}\bar{\bar{D}}^{-1}\bar{\bar{C}})^{-1}\bar{\bar{B}}\bar{\bar{D}}^{-1}$$

$$\begin{bmatrix} -K_{\rm me}^{yz} & K_{\rm me}^{yy} \\ -K_{\rm me}^{zz} & K_{\rm me}^{zy} \end{bmatrix} = (\bar{\bar{A}}\bar{\bar{C}}^{-1}\bar{\bar{D}} \;-\; \bar{\bar{B}})^{-1}$$

where the superscript '-1' denotes the inverse operator.

2.4 Two-Port Circuit Representation

Metasurface unit cells can be modeled by a two-port network in which the electric and magnetic fields on both sides of the metasurface can be considered as voltages and currents, respectively, and the dielectric substrates are regarded as transmission lines [62, 63]. In this section, the GSTCs based on the susceptibility model will be first re-arranged into a two-port representation.

Let us begin our discussion by assuming a TE incidence wave that impinges on the metasurface lying on the $x = 0$ plane as shown in Fig. 2.3. Also, let us first focus on the mono-anisotropic metasurface case; that is the metasurface does not contain magnetoelectric and electromagnetic coupling. Thus, the GSTCs in (2.13) can be written as [24, 64]

$$\hat{x} \times \Delta H_y \;=\; j\omega\varepsilon_0 \chi_{\mathrm{ee}}^{zz} E_z^{\mathrm{av}} \tag{2.33a}$$

$$\Delta E_z \times \hat{x} \;=\; j\omega\mu_0 \chi_{\mathrm{mm}}^{yy} H_y^{\mathrm{av}} \tag{2.33b}$$

Assuming $A = \frac{j\omega\varepsilon_0}{2}$, and $C = \frac{j\omega\mu_0}{2}$ for the simplicity of notation, the GSTCs can be represented as

$$H_y^+ \;-\; H_y^- \;=\; A\chi_{\mathrm{ee}}^{zz}(E_z^+ \;+\; E_z^-) \tag{2.34}$$

$$E_z^+ \;-\; E_z^- \;=\; C\chi_{\mathrm{mm}}^{yy}(H_y^+ \;+\; H_y^-) \tag{2.35}$$

The above equation can be re-arranged as

$$\begin{bmatrix} E_z^- \\ E_z^+ \end{bmatrix} = \begin{bmatrix} \overbrace{-1 - AC\chi_{\mathrm{ee}}^{zz}\chi_{\mathrm{mm}}^{yy}}^{Z_{11}} & \overbrace{-1 + AC\chi_{\mathrm{ee}}^{zz}\chi_{\mathrm{mm}}^{yy}}^{Z_{12}} \\ \underbrace{-1 + AC\chi_{\mathrm{ee}}^{zz}\chi_{\mathrm{mm}}^{yy}}_{Z_{21}} & \underbrace{-1 - AC\chi_{\mathrm{ee}}^{zz}\chi_{\mathrm{mm}}^{yy}}_{Z_{22}} \end{bmatrix} \begin{bmatrix} H_y^- \\ -H_y^+ \end{bmatrix} \tag{2.36}$$

As can be seen, this is similar to the impedance representation of two-port networks. It is important to note $Z_{11} = Z_{22}$. This means that the structure of the metasurface from

a circuit point of view is symmetric. Also, note that $Z_{12} = Z_{21}$ indicates that the two-port network is reciprocal. One of the disadvantages of this symmetric network is that it cannot remove the reflections when designing for refracting metasurfaces [61]. Thus, it is challenging to manipulate the incident radiation pattern of antennas without creating reflections. To handle this, we need an extra degree of freedom such as magnetoelectric coupling χ_{em} to further control wave transformation. This will convert the metasurface from mono-anisotropic to bi-anisotropic.

The GSTCs for bi-anisotropic metasurfaces under the TE case as shown in Fig. 2.3 will then be [16, 58]

$$\hat{x} \times (H_y^+ - H_y^-) = j\omega\varepsilon_0\chi_{\text{ee}}^{zz}E_z^{av} + j\omega\sqrt{\varepsilon_0\mu_0}\chi_{\text{em}}^{zy}H_y^{av} \tag{2.37a}$$

$$(E_z^+ - E_z^-) \times \hat{x} = j\omega\mu_0\chi_{\text{mm}}^{yy}H_y^{av} + j\omega\sqrt{\varepsilon_0\mu_0}\chi_{\text{me}}^{yz}E_z^{av} \tag{2.37b}$$

For simplicity of discussion, let us consider a reciprocal metasurface; thus having $\chi_{\text{em}}^{zy} = -\chi_{\text{me}}^{yz}$ [17, 56]. The GSTCs will then be

$$H_y^+ - H_y^- = \frac{j\omega\varepsilon_0}{2}\chi_{\text{ee}}^{zz}\,(E_z^- + E_z^+) + \frac{j\omega\sqrt{\varepsilon_0\mu_0}}{2}\chi_{\text{em}}^{zy}(H_y^- + H_y^+) \tag{2.38a}$$

$$E_z^- - E_z^+ = \frac{j\omega\mu_0}{2}\chi_{\text{mm}}^{yy}(H_y^- + H_y^+) - \frac{j\omega\sqrt{\varepsilon_0\mu_0}}{2}\chi_{\text{em}}^{zy}(E_z^- + E_z^+) \tag{2.38b}$$

To simplify the above equations, assume $A = \frac{j\omega\varepsilon_0}{2}$, $B = \frac{j\omega\sqrt{\varepsilon_0\mu_0}}{2}$, $C = \frac{j\omega\mu_0}{2}$. We can then write

$$\begin{bmatrix} E_z^- \\ E_z^+ \end{bmatrix} = \begin{bmatrix} Z_{11} & Z_{12} \\ Z_{21} & Z_{22} \end{bmatrix} \begin{bmatrix} H_y^- \\ -H_y^+ \end{bmatrix} \tag{2.39}$$

where

$$Z_{11} = \frac{AC\chi_{\text{ee}}^{zz}\chi_{\text{mm}}^{yy} + (1 + B\chi_{\text{em}}^{zy})^2}{-2A\chi_{\text{ee}}^{zz}} \tag{2.40a}$$

$$Z_{12} = \frac{-AC\chi_{\mathrm{ee}}^{zz}\chi_{\mathrm{mm}}^{yy} + 1 - \left(B\chi_{\mathrm{em}}^{zy}\right)^2}{-2A\chi_{\mathrm{ee}}^{zz}} \tag{2.40b}$$

$$Z_{21} = \frac{-AC\chi_{\mathrm{ee}}^{zz}\chi_{\mathrm{mm}}^{yy} + 1 - \left(B\chi_{\mathrm{em}}^{zy}\right)^2}{-2A\chi_{\mathrm{ee}}^{zz}} \tag{2.40c}$$

$$Z_{22} = \frac{AC\chi_{\mathrm{ee}}^{zz}\chi_{\mathrm{mm}}^{yy} + \left(1 - B\chi_{\mathrm{em}}^{zy}\right)^2}{-2A\chi_{\mathrm{ee}}^{zz}} \tag{2.40d}$$

As can be seen in (2.40), $Z_{12} = Z_{21}$ which confirms that the metasurface is reciprocal. More importantly, as opposed to the previous case, $Z_{11} \neq Z_{22}$, thus, illustrating that the two-port network of the metasurface is *not* symmetric. These non-symmetric two-port networks have been used to design reflectionless refracting metasurfaces [62], and creating desired radiation patterns without incurring reflections at the metasurface [65].

In addition, the equivalent two-port transmission (T) parameters can be derived from the GSTCs in (2.38a) as

$$\begin{bmatrix} E_z^- \\ H_y^- \end{bmatrix} = \underbrace{\begin{bmatrix} T_{11} & T_{12} \\ T_{21} & T_{22} \end{bmatrix}}_{T} \begin{bmatrix} E_z^+ \\ H_y^+ \end{bmatrix} \tag{2.41}$$

where,

$$T_{11} = -\frac{AC\chi_{\mathrm{ee}}^{zz}\chi_{\mathrm{mm}}^{yy} + \left(1 + B\chi_{\mathrm{em}}^{zy}\right)^2}{AC\chi_{\mathrm{ee}}^{zz}\chi_{\mathrm{mm}}^{yy} + \left(B\chi_{\mathrm{em}}^{zy}\right)^2 - 1} \tag{2.42a}$$

$$T_{12} = \frac{2C\chi_{\mathrm{mm}}^{yy}}{AC\chi_{\mathrm{ee}}^{zz}\chi_{\mathrm{mm}}^{yy} + \left(B\chi_{\mathrm{em}}^{zy}\right)^2 - 1} \tag{2.42b}$$

$$T_{21} = \frac{2A\chi_{\mathrm{ee}}^{zz}}{AC\chi_{\mathrm{ee}}^{zz}\chi_{\mathrm{mm}}^{yy} + \left(B\chi_{\mathrm{em}}^{zy}\right)^2 - 1} \tag{2.42c}$$

$$T_{22} = -\frac{AC\chi_{\mathrm{ee}}^{zz}\chi_{\mathrm{mm}}^{yy} + \left(1 - B\chi_{\mathrm{em}}^{zy}\right)^2}{AC\chi_{\mathrm{ee}}^{zz}\chi_{\mathrm{mm}}^{yy} + \left(B\chi_{\mathrm{em}}^{zy}\right)^2 - 1} \tag{2.42d}$$

Noting the similarity between the electric field and the voltage and the magnetic field with the current, one can see that the above equation represents the transmission parameters (also known as the ABCD parameters) of the two-port network. Also note that due to

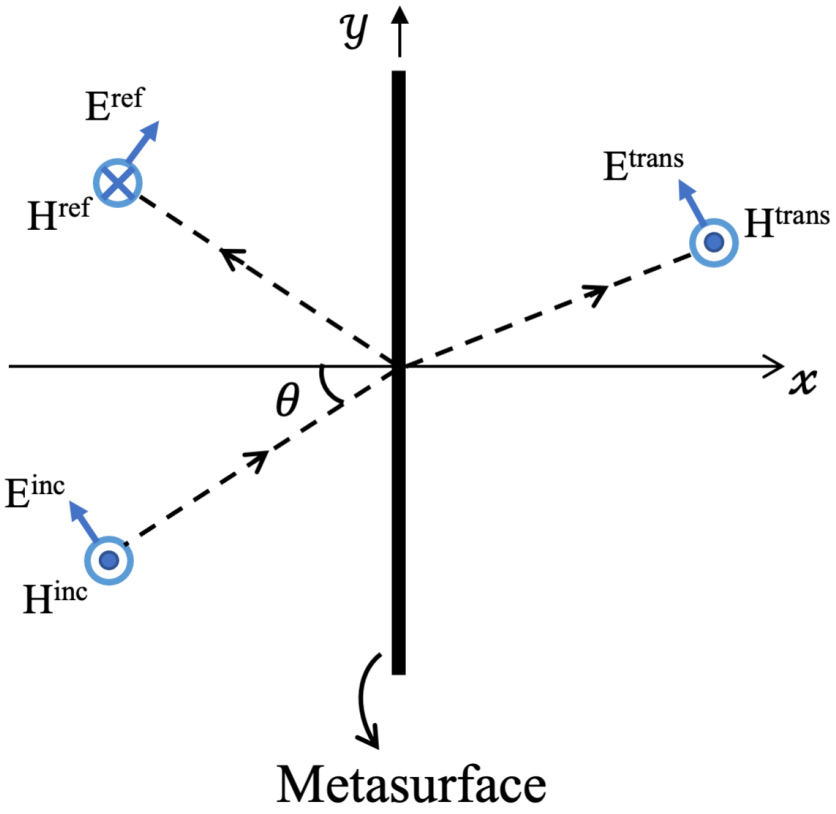

Fig. 2.4: A metasurface is located on the y axis. Thus, the input and output sides of the metasurface are $x = 0^-$ and $x = 0^+$ respectively. A TM (TE_z) incident wave illuminates the metasurface which results in reflected and transmitted waves.

the reciprocity, the determinant of the T-matrix is equal to unity (i.e., $\det(T) = T_{11}T_{22} - T_{12}T_{21} = 1$).

Now let us consider the TM case as shown in Fig. 2.4. For this polarization, the tangential fields over the metasurface (located on $x = 0$ plane) are E_y and H_z as shown in Fig. 2.4[2]. The GSTCs for the TM illumination will be [16, 24]

$$-(H_z^+ - H_z^-) = \frac{j\omega\varepsilon_0}{2}\chi_{\mathrm{ee}}^{yy}(E_y^- + E_y^+) + \frac{j\omega\sqrt{\varepsilon_0\mu_0}}{2}\chi_{\mathrm{em}}^{yz}(H_z^- + H_z^+) \tag{2.43a}$$

$$-(E_y^- - E_y^+) = \frac{j\omega\mu_0}{2}\chi_{\mathrm{mm}}^{zz}(H_z^- + H_z^+) + \frac{j\omega\sqrt{\varepsilon_0\mu_0}}{2}\chi_{\mathrm{me}}^{zy}(E_y^- + E_y^+) \tag{2.43b}$$

[2]In microwave imaging, this polarization is sometimes referred to as transverse magnetic with respect to the z direction (TE_z).

In order to simplify the above equation, we assume $A = \frac{j\omega\varepsilon_0}{2}$, $B = \frac{j\omega\sqrt{\varepsilon_0\mu_0}}{2}$, $C = \frac{j\omega\mu_0}{2}$, and also assume reciprocity ($\chi_{\rm em}^{yz} = -\chi_{\rm me}^{zy}$). The GSTCs can be re-organized to map with a two-port network as

$$\begin{bmatrix} E_y^- \\ E_y^+ \end{bmatrix} = \begin{bmatrix} Z_{11} & Z_{12} \\ Z_{21} & Z_{22} \end{bmatrix} \begin{bmatrix} H_z^- \\ -H_z^+ \end{bmatrix} \tag{2.44}$$

where

$$Z_{11} = \frac{AC\chi_{\rm ee}^{yy}\chi_{\rm mm}^{zz} + (1 - B\chi_{\rm em}^{yz})^2}{2A\chi_{\rm ee}^{yy}} \tag{2.45a}$$

$$Z_{12} = \frac{-AC\chi_{\rm ee}^{yy}\chi_{\rm mm}^{zz} + 1 - (B\chi_{\rm em}^{yz})^2}{2A\chi_{\rm ee}^{yy}} \tag{2.45b}$$

$$Z_{21} = \frac{-AC\chi_{\rm ee}^{yy}\chi_{\rm mm}^{zz} + 1 - (B\chi_{\rm em}^{yz})^2}{2A\chi_{\rm ee}^{yy}} \tag{2.45c}$$

$$Z_{22} = \frac{AC\chi_{\rm ee}^{yy}\chi_{\rm mm}^{zz} + (1 + B\chi_{\rm em}^{yz})^2}{2A\chi_{\rm ee}^{yy}} \tag{2.45d}$$

As expected $Z_{12} = Z_{21}$ which shows the reciprocity of the two-port network. In addition, $Z_{11} \neq Z_{22}$ which shows its non-symmetrical form.

Next, following the same manner, the equivalent transmission (T) parameters can be found as[3]

$$\begin{bmatrix} E_y^- \\ H_z^- \end{bmatrix} = \begin{bmatrix} T_{11} & T_{12} \\ T_{21} & T_{22} \end{bmatrix} \begin{bmatrix} E_y^+ \\ H_z^+ \end{bmatrix} \tag{2.46}$$

where the T parameters are

$$T_{11} = -\frac{AC\chi_{\rm ee}^{yy}\chi_{\rm mm}^{zz} + (1 - B\chi_{\rm em}^{yz})^2}{AC\chi_{\rm ee}^{yy}\chi_{\rm mm}^{zz} + (B\chi_{\rm em}^{yz})^2 - 1} \tag{2.47a}$$

$$T_{12} = -\frac{2C\chi_{\rm mm}^{zz}}{AC\chi_{\rm ee}^{yy}\chi_{\rm mm}^{zz} + (B\chi_{\rm em}^{yz})^2 - 1} \tag{2.47b}$$

[3]Note that instead of T_{ij}, one may use A, B, C, and D variables to represent the transmission matrix. However, since we have used A, B, C, and D variables for a different purpose, we only use T_{ij} for the parameters of the transmission matrix.

$$T_{21} = -\frac{2A\chi_{\rm ee}^{yy}}{AC\chi_{\rm ee}^{yy}\chi_{\rm mm}^{zz} + (B\chi_{\rm em}^{yz})^2 - 1} \tag{2.47c}$$

$$T_{22} = -\frac{AC\chi_{\rm ee}^{yy}\chi_{\rm mm}^{zz} + (1 + B\chi_{\rm em}^{yz})^2}{AC\chi_{\rm ee}^{yy}\chi_{\rm mm}^{zz} + (B\chi_{\rm em}^{yz})^2 - 1} \tag{2.47d}$$

In summary, knowing the surface susceptibilities of a unit cell, we can convert them to a two-port circuit representation of the unit cell.

Let us now create our two-port representation by starting from the GSTCs impedance model. To this end, let us first assume a 2D TE polarization case as shown in Fig 2.3. Similarly, let us assume a reciprocal system, thus $K_{\rm em}^{zz} = -K_{\rm me}^{yy}$ [61]. The GSTCs will then be shown as following [26]

$$\frac{1}{2}(E_z^- + E_z^+) = Z_{\rm se}^{zz}(H_y^+ - H_y^-) - K_{\rm em}^{zz}(E_z^+ - E_z^-) \tag{2.48a}$$

$$\frac{1}{2}(H_y^- + H_y^+) = Y_{\rm sm}^{yy}(E_z^+ - E_z^-) + K_{\rm em}^{zz}(H_y^+ - H_y^-) \tag{2.48b}$$

Therefore, the impedance parameters of the two-port network will be [26]

$$\begin{bmatrix} E_z^- \\ E_z^+ \end{bmatrix} = \begin{bmatrix} -Z_{\rm se}^{zz} - \frac{(2K_{\rm em}^{zz}+1)^2}{4Y_{\rm sm}^{yy}} & -Z_{\rm se}^{zz} - \frac{4K_{\rm em}^{zz\,2}-1}{4Y_{\rm sm}^{yy}} \\ -Z_{\rm se}^{zz} - \frac{4K_{\rm em}^{zz\,2}-1}{4Y_{\rm sm}^{yy}} & -Z_{\rm se}^{zz} - \frac{(2K_{\rm em}^{zz}-1)^2}{4Y_{\rm sm}^{yy}} \end{bmatrix} \begin{bmatrix} H_y^- \\ -H_y^+ \end{bmatrix} \tag{2.49}$$

By equating the impedance parameters of susceptibility model in (2.40), the effective surface susceptibilities for passive and reciprocal metasurfaces under the TE illumination can be expressed by surface impedance model as

$$\chi_{\rm ee}^{zz} = \frac{1}{2A}\frac{Y_{\rm sm}^{yy}}{Z_{\rm se}^{zz}Y_{\rm sm}^{yy} + K_{\rm em}^{zz\,2}} \tag{2.50a}$$

$$\chi_{\rm em}^{zy} = \frac{1}{2B}\frac{K_{\rm em}^{zz}}{Z_{\rm se}^{zz}Y_{\rm sm}^{yy} + K_{\rm em}^{zz\,2}} \tag{2.50b}$$

$$\chi_{\rm mm}^{yy} = \frac{1}{2C}\frac{Z_{\rm se}^{zz}}{Z_{\rm se}^{zz}Y_{\rm sm}^{yy} + K_{\rm em}^{zz\,2}} \tag{2.50c}$$

where $A = \frac{j\omega\varepsilon_0}{2}$, $B = \frac{j\omega\sqrt{\varepsilon_0\mu_0}}{2}$, and $C = \frac{j\omega\mu_0}{2}$.

Similarly for the TM incidence mode, due to reciprocity $K_{\rm em}^{yy} = -K_{\rm me}^{zz}$ the GSTCs can be written as [25–27]

$$\frac{1}{2}(E_y^- + E_y^+) = -Z_{\rm se}^{yy}(H_z^+ - H_z^-) - K_{\rm em}^{yy}(E_y^+ - E_y^-) \tag{2.51a}$$

$$\frac{1}{2}(H_z^- + H_z^+) = -Y_{\rm sm}^{zz}(E_y^+ - E_y^-) + K_{\rm em}^{yy}(H_z^+ - H_z^-) \tag{2.51b}$$

Thus, the equivalent impedance parameters can be presented as

$$\begin{bmatrix} E_y^- \\ E_y^+ \end{bmatrix} = \begin{bmatrix} Z_{\rm se}^{yy} + \frac{(2K_{\rm em}^{yy}+1)^2}{4Y_{\rm sm}^{zz}} & Z_{\rm se}^{yy} + \frac{4K_{\rm em}^{yy\,2}-1}{4Y_{\rm sm}^{zz}} \\ Z_{\rm se}^{yy} + \frac{4K_{\rm em}^{yy\,2}-1}{4Y_{\rm sm}^{zz}} & Z_{\rm se}^{yy} + \frac{(2K_{\rm em}^{yy}-1)^2}{4Y_{\rm sm}^{zz}} \end{bmatrix} \begin{bmatrix} H_z^- \\ -H_z^+ \end{bmatrix} \tag{2.52}$$

Similarly by equating these Z parameters with their counterpart associated with the susceptibility model shown in (2.45), the following relation under the TM case can be obtained

$$\chi_{\rm ee}^{yy} = \frac{1}{2A}\,\frac{Y_{\rm sm}^{zz}}{Z_{\rm se}^{yy}Y_{\rm sm}^{zz} + K_{\rm em}^{yy\,2}} \tag{2.53a}$$

$$\chi_{\rm em}^{yz} = \frac{1}{2B}\,\frac{-K_{\rm em}^{yy}}{Z_{\rm se}^{yy}Y_{\rm sm}^{zz} + K_{\rm em}^{yy\,2}} \tag{2.53b}$$

$$\chi_{\rm mm}^{zz} = \frac{1}{2C}\,\frac{Z_{\rm se}^{yy}}{Z_{\rm se}^{yy}Y_{\rm sm}^{zz} + K_{\rm em}^{yy\,2}} \tag{2.53c}$$

where $A = \frac{j\omega\varepsilon_0}{2}$, $B = \frac{j\omega\sqrt{\varepsilon_0\mu_0}}{2}$, and $C = \frac{j\omega\mu_0}{2}$.

2.5 Cascaded Layer Topology

One of the approaches to realize the equivalent surface parameters is to use cascaded layer topology, in which the admittance/impedance layers are connected by two dielectric substrates, and the substrates are regarded as transmission line model in the network expression [28, 62, 63]. The topology is presented in Fig. 2.5(a), and the circuit point of view is shown in Fig. 2.5(b). In order to satisfy the required two-port representation, at least

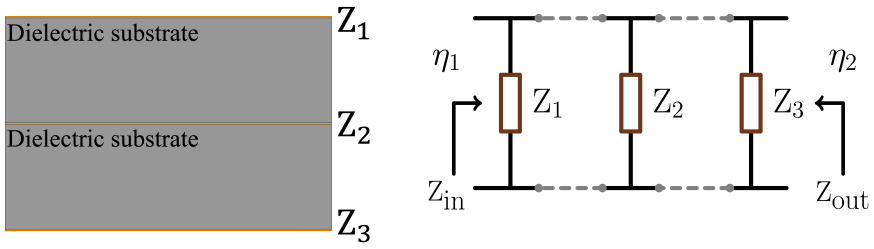

(a) Structure topology (b) Circuit view point

Fig. 2.5: The equivalent circuit form of a unit cell topology for a non-reflection metasurface. The complex input and output impedance η_1 and η_2 can be implemented in different ways.

three impedance layers are needed. From the cascaded layer topology, the corresponding T parameters can be obtained as [66, Chapter 2]

$$[T] = \underbrace{\begin{bmatrix} 1 & 0 \\ Y_1 & 1 \end{bmatrix}}_{\text{Layer 1}} \times \underbrace{[M]}_{\text{Substrate 1}} \times \underbrace{\begin{bmatrix} 1 & 0 \\ Y_2 & 1 \end{bmatrix}}_{\text{Layer 2}} \times \underbrace{[N]}_{\text{Substrate 2}} \times \underbrace{\begin{bmatrix} 1 & 0 \\ Y_3 & 1 \end{bmatrix}}_{\text{Layer 3}} \tag{2.54}$$

where Y_i ($i \in \{1, 2, 3\}$) is the admittance of each layer; i.e., $Y_i = 1/Z_i$. The matrices $[M]$ and $[N]$ represent the equivalent T-matrix of the dielectric substrates. Note that $[M]$ and $[N]$ are not necessarily the same; i.e., the dielectric substrates are not necessarily identical. Based on the transmission line theorem, these matrices can be obtained as [67, Appendix A]

$$[M] = \begin{bmatrix} \cos(\beta_1 t_1) & jZ_{s1}\sin(\beta_1 t_1) \\ \frac{j\sin(\beta_1 t_1)}{Z_{s1}} & \cos(\beta_1 t_1) \end{bmatrix} \tag{2.55a}$$

$$[N] = \begin{bmatrix} \cos(\beta_2 t_2) & jZ_{s2}\sin(\beta_2 t_2) \\ \frac{j\sin(\beta_2 t_2)}{Z_{s2}} & \cos(\beta_2 t_2) \end{bmatrix} \tag{2.55b}$$

where β_1, β_2, are the wavenumbers in the first and second dielectric substrates, and t_1, t_2 are the thickness of the substrates, respectively. Also, Z_{s1} and Z_{s2} are the characteristic impedance of the corresponding substrates.

Assuming that we would like to have the following desired T matrix

$$T^{\text{des}} = \begin{bmatrix} T_{11}^{\text{des}} & T_{12}^{\text{des}} \\ T_{21}^{\text{des}} & T_{22}^{\text{des}} \end{bmatrix} \tag{2.56}$$

and knowing our substrates to be used, we can find the required impedance values of each layer as

$$Y_1 = \frac{T_{22}^{\text{des}} - N_{12}M_{21} - N_{12}M_{22}Y_2 - M_{22}N_{22}}{M_{11}N_{12} + Y_2M_{12}N_{12} + M_{12}N_{22}} \tag{2.57a}$$

$$Y_2 = \frac{T_{12}^{\text{des}} - M_{11}N_{12} - M_{12}N_{22}}{M_{12}N_{12}} \tag{2.57b}$$

$$Y_3 = \frac{T_{11}^{\text{des}} - N_{11}M_{11} - N_{11}M_{12}Y_2 - M_{12}N_{21}}{M_{11}N_{12} + Y_2M_{12}N_{12} + M_{12}N_{22}} \tag{2.57c}$$

2.6 Ansys HFSS Simulation to Infer Y_1, Y_2, and Y_3

Let us now see how we can obtain Y_1, Y_2, and Y_3 by performing Ansys HFSS simulation. Assume we use geometries such as dogbone copper traces [24, 26, 28] to implement our admittance layers. Then, we need to know the admittance value for a given W, L, S, and D as depicted in Fig. 2.6. To this end, a unit cell is simulated in Ansys HFSS (or other solvers), surrounded by periodic boundary conditions. The top and bottom surfaces are excited by Floquet ports, and the excitation ports are placed far enough from the unit cell to not include the effect of evanescent modes [29]. For example, the excitation ports can be vertically placed 2λ away from the surface of the unit cell, in which λ is wavelength in free space at the operating frequency.

The de-embedding needs to be performed to move the reference plane right on the unit cell structure [27]. This has been shown by two arrows in Fig. 2.7. With respect to this

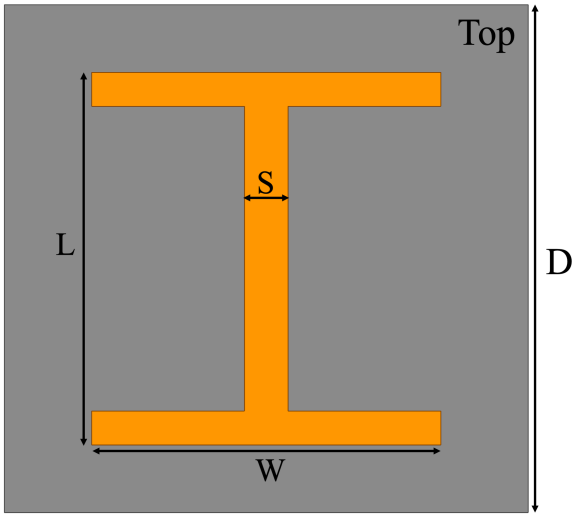

Fig. 2.6: Top view of the dogbone geometry

new reference plane, the scattering parameters

$$[S] = \begin{bmatrix} S_{11} & S_{12} \\ S_{21} & S_{22} \end{bmatrix} \tag{2.58}$$

can be obtained. The structure is reciprocal. Based on reciprocity, S_{12} equals to S_{21} [66]. Once we get our scattering parameters from Ansys HFSS, we can convert it to the transmission parameters as follows [68]

$$T_{11} = \frac{(Z_{01}^* + S_{11}Z_{01})(1 - S_{22}) + S_{12}S_{21}Z_{01}}{2S_{21}(R_{01}R_{02})^{1/2}} \tag{2.59a}$$

$$T_{12} = \frac{(Z_{01}^* + S_{11}Z_{01})(Z_{02}^* + S_{22}Z_{02}) - S_{12}S_{21}Z_{01}Z_{02}}{2S_{21}(R_{01}R_{02})^{1/2}} \tag{2.59b}$$

$$T_{21} = \frac{(1 - S_{11})(1 - S_{22}) - S_{12}S_{21}}{2S_{21}(R_{01}R_{02})^{1/2}} \tag{2.59c}$$

$$T_{22} = \frac{(1 - S_{11})(Z_{02}^* + S_{22}Z_{02}) + S_{12}S_{21}Z_{02}}{2S_{21}(R_{01}R_{02})^{1/2}} \tag{2.59d}$$

where Z_{01} is the wave impedance at the source side. In our case, Z_{01} is the impedance of free space assuming normal incidence, thus, $Z_{01} = 120\pi \approx 377\Omega$. On the other hand, Z_{02} is

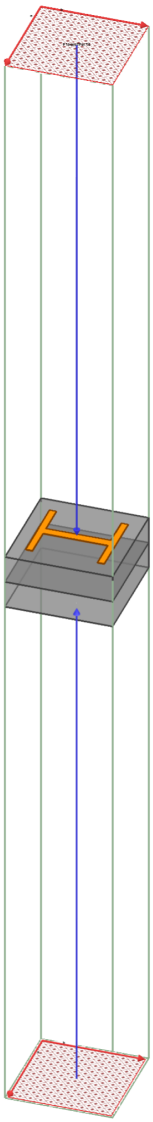

Fig. 2.7: Unit cell simulation with master and slave periodical boundary conditions surrounded, and two Floquet port excitations located above and below 2λ from the metasurface, where λ is the wavelength in free space at the operating frequency.

the wave impedance at the output side. Assuming that the output side is also in free space, then we have, $Z_{02} = 120\pi \approx 377\Omega$. Note that, in general, Z_{01} and Z_{02} can be complex numbers. R_{01} and R_{02} are the real parts of Z_{01} and Z_{02} respectively, and the superscript '$*$' denotes complex conjugate operator. Since Z_{01} and Z_{02} are purely real numbers in this case, R_{01} and R_{02} will equal Z_{01} and Z_{02} respectively. Furthermore, the $*$ operator will

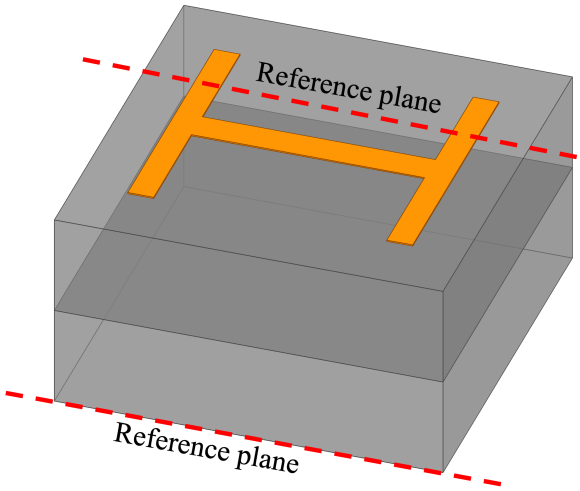

Fig. 2.8: Finding the impedance of the top layer.

have no effect.

Under this simplifying assumption, (2.59) can be simplified to

$$T_{11} = \frac{(1+S_{11})(1-S_{22})+S_{12}S_{21}}{2S_{21}} \tag{2.60a}$$

$$T_{12} = Z_0\frac{(1+S_{11})(1+S_{22})-S_{12}S_{21}}{2S_{21}} \tag{2.60b}$$

$$T_{21} = \frac{1}{Z_0}\frac{(1-S_{11})(1-S_{22})-S_{12}S_{21}}{2S_{21}} \tag{2.60c}$$

$$T_{22} = \frac{(1-S_{11})(1+S_{22})+S_{12}S_{21}}{2S_{21}} \tag{2.60d}$$

where $Z_0 = 120\pi$.

In summary, we had the S parameters with respect to the two reference planes. We then converted them to T parameters, and denote them as $[T_{\text{total}}]$. To extract the admittance or impedance value of the top metallic layer as shown in Fig. 2.8, we have

$$[T_{\text{total}}] = [T_{\text{top layer}}][M][N] \tag{2.61}$$

where $[T_{\text{top layer}}]$ is the T parameters of the top layer. As noted in Section 2.5, M represents the transmission matrix for the first substrate, and N represents the transmission matrix

for the second substrate in the metasurface. (For example, see [27, 28, 62, 63].) Therefore, $[T_{\text{top layer}}]$ will be

$$[T_{\text{top layer}}] = [T_{\text{total}}][N]^{-1}[M]^{-1} \tag{2.62}$$

For example, $[M]$ and $[N]$ are typically the same, and therefore

$$[M] = [N] = \begin{bmatrix} \cos(\beta_{\text{sub}} l) & jZ_{\text{sub}} \sin(\beta_{\text{sub}} l) \\ \frac{j \sin(\beta_{\text{sub}} l)}{Z_{\text{sub}}} & \cos(\beta_{\text{sub}} l) \end{bmatrix} \tag{2.63}$$

where Z_{sub} is the characteristic impedance of the substrate, and β_{sub} is the wavenumber of the substrate. (For example, we may use Rogers RO3003 substrate with $\varepsilon_r = 3$, and $l = 1.52$ mm.) Thus

$$\beta_{\text{sub}} = \frac{2\pi}{\lambda_{\text{sub}}} = \frac{2\pi f}{c_0/\sqrt{\varepsilon_r}}$$
$$Z_{\text{sub}} = \frac{\eta}{\sqrt{\varepsilon_r}} = \frac{120\pi}{\sqrt{\varepsilon_r}}$$

where λ_{sub} is the wavelength in the substrate at the operating frequency. After finding $[T_{\text{top layer}}]$, it should ideally be in the following form

$$[T_{\text{top layer}}] = \begin{bmatrix} T_{11} & T_{12} \\ T_{21} & T_{22} \end{bmatrix} \xrightarrow{\text{IDEALLY}} \begin{bmatrix} 1 & 0 \\ Y_1 & 1 \end{bmatrix} \tag{2.64}$$

Therefore, 'T_{21}' will be Y_1 and $Z_1 = \frac{1}{Y_1} = \frac{1}{T_{21}}$.

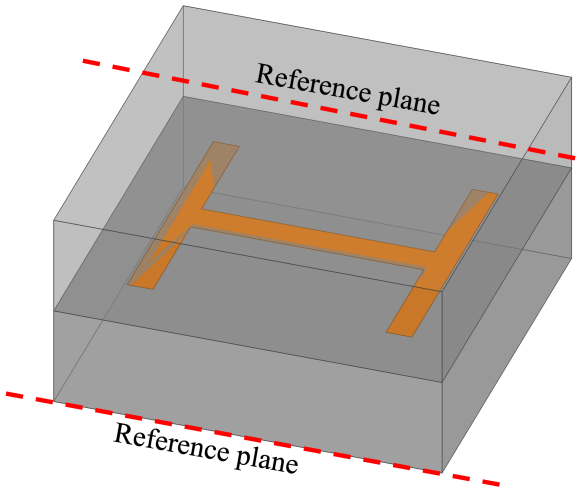

Fig. 2.9: Finding the impedance of the middle layer.

For the dogbone on the middle layer as shown in Fig. 2.9, we perform a similar analysis to find S parameters at the reference plane, then we convert S parameters to the $[T]$, and will call it $[T_{\text{total}}]$. Then

$$[T_{\text{total}}] = [M][T_{\text{middle layer}}][N] \tag{2.65}$$

Thus

$$[T_{\text{middle layer}}] = [M]^{-1}[T_{\text{total}}][N]^{-1} \tag{2.66}$$

Again, ideally, the $[T_{\text{middle layer}}]$ will be in the form of

$$[T_{\text{middle layer}}] = \begin{bmatrix} T_{11} & T_{12} \\ T_{21} & T_{22} \end{bmatrix} \xrightarrow{\text{IDEALLY}} \begin{bmatrix} 1 & 0 \\ Y_2 & 1 \end{bmatrix} \tag{2.67}$$

and therefore its corresponding Z_2 will be $1/Y_2$.

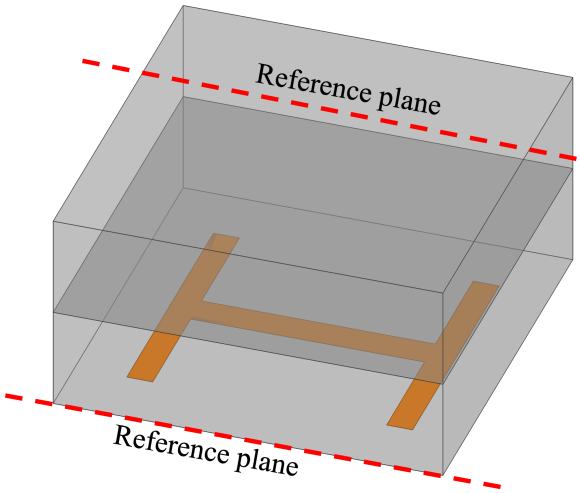

Fig. 2.10: Finding the impedance of the bottom layer.

Similarly as shown in Fig. 2.10, for the bottom layer we find $[S]$ at reference planes, then find the total $[T]$, then

$$[T_{\text{total}}] = [M][N][T_{\text{bottom layer}}] \tag{2.68}$$

Then

$$[T_{\text{bottom layer}}] = [N]^{-1}[M]^{-1}[T_{\text{total}}] \tag{2.69}$$

Similarly, $[T_{\text{bottom layer}}]$ will be ideally of the following form

$$[T_{\text{bottom layer}}] = \begin{bmatrix} T_{11} & T_{12} \\ T_{21} & T_{22} \end{bmatrix} \xrightarrow{\text{IDEALLY}} \begin{bmatrix} 1 & 0 \\ Y_3 & 1 \end{bmatrix} \tag{2.70}$$

and therefore its corresponding Z_3 will be $1/Y_3$. The Matlab code for calculating admittance (or impedance) for top, middle, and bottom layers is provided in Appendix B.

2.7 Conditions of Reciprocity and Losslessness

The reciprocity conditions for a bi-anisotropic metasurface are [16, 17]

$$\overline{\overline{\chi}}_{\rm ee} \;=\; \overline{\overline{\chi}}_{\rm ee}^{T}, \qquad \overline{\overline{\chi}}_{\rm mm} \;=\; \overline{\overline{\chi}}_{\rm mm}^{T}, \qquad \overline{\overline{\chi}}_{\rm em} \;=\; -\overline{\overline{\chi}}_{\rm me}^{T} \tag{2.71}$$

where the superscript 'T' denotes the matrix transpose operator. Reciprocal metasurfaces are classified into different categories [24]. For example one category is the Omega-bianisotropic metasurface in which the induced electric (magnetic) currents are perpendicular to the applied magnetic (electric) fields [61].

To begin the discussion on lossless or lossy metasurfaces, we need to start with the time-average Poynting vector [69]

$$\boldsymbol{S}^{\rm av} = \frac{1}{2}{\rm Re}(\boldsymbol{E}\times\boldsymbol{H}^{*}) \tag{2.72}$$

where 'Re' is the real-part operator and the superscript '$*$' denotes the complex conjugate operator. Assuming a passive and reciprocal metasurface, the divergence of $\boldsymbol{S}^{\rm av}$ will be [56, Appendix B], [4].

$$\begin{aligned}\nabla\;\cdot\;\boldsymbol{S}^{\rm av} \;=\; -\frac{1}{4}{\rm Re}\Big[&j\omega(\varepsilon_0\boldsymbol{E}^{*}\cdot(\overline{\overline{\chi}}_{\rm ee}\;-\;\overline{\overline{\chi}}_{\rm ee}^{\dagger})\cdot\boldsymbol{E}\\ &+\;\mu_0\boldsymbol{H}^{*}\cdot(\overline{\overline{\chi}}_{\rm mm}\;-\;\overline{\overline{\chi}}_{\rm mm}^{\dagger})\cdot\boldsymbol{H}\;+\;2k_0\boldsymbol{E}^{*}\cdot\;(\overline{\overline{\chi}}_{\rm me}\;-\;\overline{\overline{\chi}}_{\rm em}^{\dagger})\cdot\boldsymbol{H})\Big]\end{aligned} \tag{2.73}$$

where '$\nabla\cdot$' is the divergence operator, and $\dagger$ is conjugate transpose operator.

Assuming reciprocity noted in (2.71), (2.73) will become

$$\begin{aligned}\nabla\;\cdot\;\boldsymbol{S}^{\rm av} \;=\; -\frac{1}{4}{\rm Re}\big[&j\omega(\varepsilon_0\boldsymbol{E}^{*}\cdot(\overline{\overline{\chi}}_{\rm ee}\;-\;\overline{\overline{\chi}}_{\rm ee}^{*})\cdot\boldsymbol{E}\\ &+\;\mu_0\boldsymbol{H}^{*}\cdot(\overline{\overline{\chi}}_{\rm mm}\;-\;\overline{\overline{\chi}}_{\rm mm}^{*})\cdot\boldsymbol{H}\;+\;2k_0\boldsymbol{E}^{*}\cdot\;(\overline{\overline{\chi}}_{\rm me}\;+\;\overline{\overline{\chi}}_{\rm me}^{*})\cdot\boldsymbol{H})\big]\end{aligned} \tag{2.74}$$

Simplifying the above further, we arrive at

$$\begin{aligned}\nabla \cdot \boldsymbol{S}^{\mathrm{av}} \;=\; & -\frac{1}{4}\mathrm{Re}\left[j\omega(\varepsilon_0 \boldsymbol{E}^* \cdot (2j\mathrm{Im}\{\overline{\overline{\chi}}_{\mathrm{ee}}\}) \cdot \boldsymbol{E}\right. \\ & \left. +\; \mu_0 \boldsymbol{H}^* \cdot (2j\mathrm{Im}\{\overline{\overline{\chi}}_{\mathrm{mm}}\}) \cdot \boldsymbol{H} \;+\; 2k_0 \boldsymbol{E}^* \cdot\; (2\mathrm{Re}\{\overline{\overline{\chi}}_{\mathrm{me}}\}) \cdot \boldsymbol{H})\right] \end{aligned} \tag{2.75}$$

Let us now consider four scenarios:

- To have a reciprical, lossless and gainless metasurface, we need to have $\nabla \cdot \boldsymbol{S}^{\mathrm{av}} = 0$. To ensure this, we need to have

$$\mathrm{Im}(\overline{\overline{\chi}}_{\mathrm{ee}}) = 0 \tag{2.76a}$$

$$\mathrm{Im}(\overline{\overline{\chi}}_{\mathrm{mm}}) = 0 \tag{2.76b}$$

$$\mathrm{Re}(\overline{\overline{\chi}}_{\mathrm{me}}) = 0 \;\xrightarrow{\text{reciprocity}}\; \mathrm{Re}(\overline{\overline{\chi}}_{\mathrm{em}}) = \;0 \tag{2.76c}$$

- To have a lossy metasurface, we need to have $\nabla \cdot \boldsymbol{S}^{\mathrm{av}} < 0$. For simplicity, let us assume reciprocal non-gyrotropic bianisotropic metasurfaces in which $\overline{\overline{\chi}}_{\mathrm{ee}}$, $\overline{\overline{\chi}}_{\mathrm{mm}}$ have zero off-diagonal elements, and the magnetoelectric coupling $\overline{\overline{\chi}}_{\mathrm{em}}$ and $\overline{\overline{\chi}}_{\mathrm{me}}$ have zero diagonal components. Consequently, the surface susceptibility tensors can be reduced to a scalar form for each polarization (TE and TM) [24]. Herein, we use χ_{ee}, χ_{mm} and χ_{em} (without the $\overline{\overline{\cdot}}$ symbol) to represent the scalar form of the surface susceptibilities. That is,

$$\chi_{\mathrm{ee}} = \chi_{\mathrm{ee}}^{zz}, \quad \chi_{\mathrm{mm}} = \chi_{\mathrm{mm}}^{zz}, \quad \chi_{\mathrm{em}} = \chi_{\mathrm{em}}^{zy} \qquad \text{TM polarization} \tag{2.77}$$

and

$$\chi_{\mathrm{ee}} = \chi_{\mathrm{ee}}^{yy}, \quad \chi_{\mathrm{mm}} = \chi_{\mathrm{mm}}^{yy}, \quad \chi_{\mathrm{em}} = \chi_{\mathrm{em}}^{yz} \qquad \text{TE polarization} \tag{2.78}$$

Therefore, the divergence of the time-average Poynting vector becomes

$$\nabla \cdot \boldsymbol{S}^{\mathrm{av}} = \frac{1}{2}\mathrm{Re}\Big\{\omega\varepsilon_0 \left|\boldsymbol{E}\right|^2 \mathrm{Im}\{\chi_{\mathrm{ee}}\} + \omega\mu_0 \left|\boldsymbol{H}\right|^2 \mathrm{Im}\{\chi_{\mathrm{mm}}\} - j2\omega k_0 \boldsymbol{E}^* \cdot \boldsymbol{H}\mathrm{Re}\{\chi_{\mathrm{em}}\}\Big\} \tag{2.79}$$

To ensure (2.79) is less than zero, the term involved with χ_{em} can be set to zero, since this term depends on the multiplication of electric field and complex conjugate magnetic field, and the sign is uncertain. Thus, a *sufficient* way to achieve this can be the following

$$\text{Im}\{\chi_{\text{ee}}\} \;<\; 0 \tag{2.80a}$$

$$\text{Im}\{\chi_{\text{mm}}\} \;<\; 0 \tag{2.80b}$$

$$\text{Re}\{\chi_{\text{em}}\} \;=\; \text{Re}\{\chi_{\text{me}}\} \;=\; 0 \tag{2.80c}$$

- To have a passive metasurface $\nabla \cdot \boldsymbol{S}^{\text{av}} \leq 0$.
- To have an active (including gain) metasurface, we need to have $\nabla \cdot \boldsymbol{S}^{\text{av}} > 0$. Similar to the lossy case, we restrict ourselves to scalar susceptibilities. A *sufficient* way to achieve this is

$$\text{Im}\{\chi_{\text{ee}}\} \;>\; 0 \tag{2.81a}$$

$$\text{Im}\{\chi_{\text{mm}}\} \;>\; 0 \tag{2.81b}$$

$$\text{Re}\{\chi_{\text{em}}\} \;=\; \text{Re}\{\chi_{\text{me}}\} \;=\; 0 \tag{2.81c}$$

Chapter 3

Fundamentals of MWI

Microwave Imaging (MWI)

Microwave imaging (MWI) is an imaging modality that reconstructs qualitative or quantitative images of the relative complex permittivity profile of an object of interest (OI) [42–46]. In MWI, the OI resides within the imaging domain denoted by $\mathcal{D}$, and the OI is illuminated by antennas which are located outside of the imaging domain from different angles as shown in Fig. 3.1. The resulting scattered fields are obtained by a set of receivers around the OI in the measurement domain denoted by $\mathcal{S}$.

In the absence of the OI, the fields collected are called incident fields as shown in Fig. 3.1(a). On the other hand, when the OI is present in the imaging domain, the collected fields are called total fields as shown in Fig. 3.1(b). By subtracting incident fields from total fields, the corresponding scattered fields can be obtained. The collected scattered field data are then processed by an inverse scattering algorithm to reconstruct the profile of complex permittivity of the OI.

Microwave imaging can be done in different fashions. The simplest one is the case of tomographic configuration in which a TM_z polarization is assumed, and the relative complex permittivity is reconstructed on a given slice. The main assumption for this is that the object and the system are invariant in a given direction. In our case, we assume that we

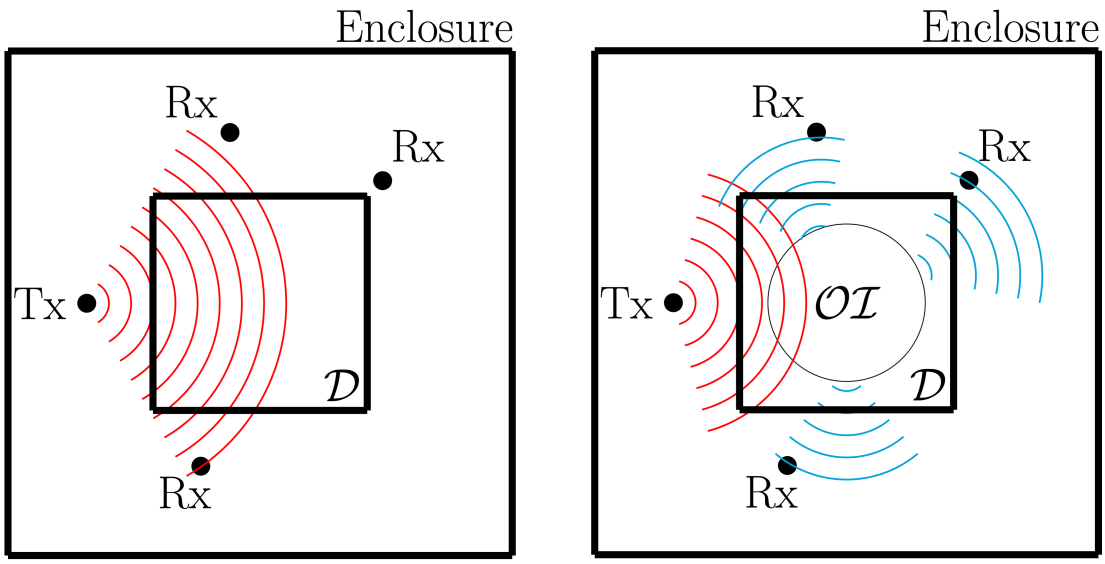

Fig. 3.1: MWI system schematic (a) incidence fields collection with absence of OI, (b) total fields collection with presence of OI.

are invariant with respect to z, and the imaging plane is the xy plane. Consequently, under TM_z polarization, we have E_z, H_x, and H_y components. Therefore, we can formulate the problem in terms of the E_z component.

Under the above assumption, the main governing equation for MWI can be expressed as

$$\begin{aligned} &\nabla^2 E_z^{\text{scat}} + k_b^2 E_z^{\text{scat}} = -k_b^2 w, \ \text{(in the imaging system)} \\ &\text{subject to the 'Appropriate Boundary Conditions' (or ABCs)} \end{aligned} \tag{3.1}$$

where ∇^2 denotes the Laplacian operator, k_b is the wavenumber in the background medium, E_z^{scat} represents the scattered fields and w denotes the contrast sources [50] in the OI to be defined below.

Green's functions which define the Dirac delta (point) response of a given system can be used to present the general solution to the above Helmoltz equation. Using the Green's

function, we arrive at the so-called data equation [50].

$$E_z^{\text{scat}}(\boldsymbol{r} \in \mathcal{S}) = k_b^2 \int_{\mathcal{D}} g(\boldsymbol{r}, \boldsymbol{r}') w(\boldsymbol{r}') d\boldsymbol{r}' \qquad r \notin D \tag{3.2}$$

where g denotes the green's function with appropriate boundary conditions (ABC). To simplify the solutions to (3.2), Sommerfeld radiation condition which assumes the background medium extends to infinity is introduced. This Green's function is

$$g(\boldsymbol{r}, \boldsymbol{r}') = g(\boldsymbol{r} - \boldsymbol{r}') = \frac{1}{4j} H_0^2(k_b |\boldsymbol{r} - \boldsymbol{r}'|) \tag{3.3}$$

where H_0^2 is the zeroth order Hankel function of the second kind, $\mathbf{r}$ and $\mathbf{r}'$ are the observation and source locations respectively. As noted earlier, $w(\boldsymbol{r}')$ represents contrast sources which can be expressed as

$$w(\boldsymbol{r}') \triangleq O(\boldsymbol{r}') E_z(\boldsymbol{r}') \tag{3.4}$$

where $O(\boldsymbol{r})$ denotes the relative complex permittivity contrast of OI with respect to the background medium shown as

$$O(\boldsymbol{r}) \triangleq \frac{\varepsilon(\boldsymbol{r}) - \varepsilon_b}{\varepsilon_b} \tag{3.5}$$

where ε_b is the relative permittivity of the background medium and ε is the unknown relative complex permittivity of the OI. E_z denotes the total field in the imaging domain which is also unknown and is governed by the following equation [50].

$$E_z^{\text{tot}}(\boldsymbol{r} \in \mathcal{D}) = E_z^{\text{inc}} + k_b^2 \int_{\mathcal{D}} g(\boldsymbol{r}, \boldsymbol{r}') w(\boldsymbol{r}') d\boldsymbol{r}' \qquad r \in D \tag{3.6}$$

where E_z^{inc} in the incident field (i.e., field in the absence of the OI).

Since both O and E_z are unknown and related to each other, the mathematical problem of MWI is nonlinear. Therefore, the contrast is updated in an iterative fashion. Two types of algorithms are commonly used to iteratively reconstruct the relative complex permittivity contrast, named Gauss-Newton inversion (GNI) and contrast source inversion (CSI)

methods. While optimizing, a regularization scheme is used to stabilize the inversion process (i.e., treating the ill-posed problem) [70, 71]. In order to overcome the difficulties of selecting regularization parameters, multiplicative regularization (MR) has been utilized for inverse scattering applications to automatically regularize the problem. Thus, MR-GNI, and MR-CSI are two common methods to reconstruct the OI's contrast [48–50, 52, 53].

It is well-known that the success of the inverse scattering algorithms depend on how close the actual system performance is to the simulated problem performance. Since the true OI is unknown in the problem, checking how close the simulated data follow the measured data is not possible. Thus, calibration techniques need to be used to check how close the measured and simulated data are and develop calibration coefficients to handle major discrepancies [72]. (In general, the closer the calibration object to the OI, the better.)

At least there are two types of calibration for MWI. In the incident field calibration, for a given transmitter, we compare the simulated incident data collected at each receiver in the imaging algorithm with those collected in the measurement. For this comparison, calibration coefficients are formed by matching the modeled incident field with the measurement incident field. This calibration factor will then be applied to the scattered data collected from the OI when that particular transmitter is on. Once this process has been applied to all the transmitters, we now have our calibrated scattered data for the imaging algorithm to invert. The other calibration approach is the scattered field calibration in which a known target is placed in the imaging domain to compare its corresponding simulated and measured scattered field data. Based on this comparison, calibration coefficients are formed. In the same manner as the incident field calibration, the collected scattered field data from the OI can be calibrated [72].

As noted before, the purpose of this thesis is to investigate the use of metasurfaces for MWI. Metasurfaces can be used for MWI at least in four possible ways:

- Metasurfaces can be utilized as MWI casing (enclosure) [10, 59]. For example, absorbing metasurfaces can be used as MWI casing to mitigate reflections from the enclosure

and imitate an infinite space. Since the absorption occurs at the metasurface, the loss of the coupling liquid (background medium) can be reduced, and the signal to noise ratio of the measured data can be enhanced.

- Metasurfaces can be implemented as impedance matching transformer [25,73,74]. This can be used to more effectively couple the irradiating energy from the background medium into the OI. The implementation of matching metasurfaces can remove (or alleviate) the necessity of having matching fluids.

- Metasurfaces can manipulate the MWI illumination wavefront. For example, a focused beam can be formed by implementing metasurfaces in front of the transmitting source [75, 76].

- Metasurfaces can be used to change the polarization [7, 8]. This can be for example used to change the polarization of the incident field with which the OI is irradiated.

In this thesis, the first two examples will be presented in the next two chapters.

Chapter 4

Absorbing Metasurfaces in Microwave Imaging

Preface

In this chapter, absorbing metasurfaces are proposed to be used as the enclosure of microwave imaging (MWI) systems to mitigate the reflections from enclosure. The materials presented in this chapter is based on the following works of the author [59, 77, 78]. In particular, it is based on the following journal paper accepted for the IEEE Transactions on Antennas and Propagation:

- Ziqi Liu, Nozhan Bayat and Puyan Mojabi, "On the Use of Absorbing Metasurfaces in Microwave Imaging," *accepted for IEEE Transactions on Antennas and Propagation.* Manuscript ID: AP2010-1956.R2.

- Therefore, some of the figures presented in this chapter can be found in the above paper.

During the review process of the above paper, the reviewers have asked that the paper be summarized. In this chapter, we have used the original version of the above paper which

provides more details and background information. The pre-print of our original submission can be found in the IEEE TechRxiv website as

- Ziqi Liu, Nozhan Bayat and Puyan Mojabi, "On the Use of Absorbing Metasurfaces in Microwave Imaging," *TechRxiv*, 09-Oct-2020, doi: 10.36227/techrxiv.13063925.v1.
  - URL: `https://doi.org/10.36227/techrxiv.11774955.v1`

The above manuscripts were the follow-up work of the author's 2020 conference paper:

- Ziqi Liu, Nozhan Bayat and Puyan Mojabi, "On Microwave Imaging with Absorbing Metasurface Enclosure," *IEEE AP-S Symposium on Antennas and Propagation and USNC-URSI Radio Science Meeting*, Montreal, July 2020.

Consequently, the materials of this chapter have been taken from our under-review paper at the IEEE Transactions on Antennas and Propagation and our IEEE TechRxiv Preprint cited above. Due to this, some materials presented in Chapters 2 and 3 are repeated in this chapter to keep the flow of the original submission.

Abstract

Microwave imaging (MWI) systems are usually enclosed within casings, e.g., in order to contain the utilized coupling liquid or to help mount the antenna system. On the other hand, inverse scattering algorithms, which are used to process the measured microwave scattering data, often assume that the background medium of the imaging system extends to infinity (i.e., unbounded background medium assumption). Thus, they do not consider the reflections occurring at the system enclosure. For such algorithms to yield successful images, these reflections need to be minimized, e.g., via the use of a lossy coupling liquid. As an alternative to a lossy background medium which also reduces the desired signal level, this paper investigates the use of metallic-backed absorbing metasurfaces as the MWI system enclosure in order to (i) reduce these reflections, and also (ii) to shield the MWI system

from external interference. Using simulated data, we then show that standard inverse scattering algorithms, employing the free-space assumption, can successfully process the data collected under the metasurface enclosure and yield acceptable permittivity images. The advantages and disadvantages of absorbing metasurface enclosure, along with the limitations of this study, will also be discussed. Finally, an absorbing metasurface is fabricated and its reflectivity is experimentally evaluated.

4.1 Introduction

Microwave imaging (MWI) is a non-invasive and non-ionizing imaging modality that creates qualitative or quantitative images of the relative complex permittivity profile of an object of interest (OI) [42–46]. The inverse scattering approach to MWI, which is the focus of this paper, is usually concerned with reconstructing a *quantitative* image of the OI's relative complex permittivity profile. In this approach, the OI is often irradiated from different angles, and the resulting scattered fields are collected at different locations around the OI. These external scattered field data are then processed by an inverse scattering algorithm to reconstruct a quantitative image of the OI's relative complex permittivity profile. To this end, the inverse scattering approach employs a nonlinear optimization scheme to iteratively reconstruct a quantitative relative complex permittivity profile by minimizing the discrepancy between the simulated scattering data from a predicted permittivity image and the measured scattered data from the true OI. Two common inverse scattering algorithms, which are used in this paper, are the Gauss-Newton inversion (GNI) [48, 49] and contrast source inversion (CSI) algorithms [50].

Based on the above optimization approach to MWI, it can be understood that the success of the inverse scattering algorithms relies on the following *necessary* condition: if the true model of the OI is given to the computational electromagnetic solver used in the inverse scattering algorithm, the resulting simulated scattered data need to be sufficiently close to the measured data. However, since the true OI is the actual unknown of the problem,

this can never be checked in practice. Instead, the above requirement is often checked in the absence of the OI, i.e., comparing the simulated incident field with the measured incident field. Alternatively, a known target can be employed to compare its corresponding simulated and measured scattered field data. (This comparison of the simulated and measured data is done as part of the data calibration step in microwave imaging [72].)

One of the sources of discrepancy between the simulated and measured data is the reflections from the microwave imaging system enclosure (casing). For example, consider the microwave biomedical imaging experiments considered in [52] in which water was used as the coupling liquid to help with coupling incident microwaves into biological tissues. The use of this coupling liquid fluid reduces the overall impedance mismatch between the OI and the background medium. However, this comes with the following challenge. Assume that the enclosure of the MWI system is an electrically thin plexiglass. Therefore, at the enclosure of the MWI system, we now have a significant impedance mismatch between the interface of water (inside the enclosure) and air (outside the enclosure). Alternatively, if the enclosure is a perfect electric conductor (PEC), we will have 100% reflection.

One common method to handle the above challenge is to make the coupling liquid (also known as matching fluid) lossy to reduce the level of the reflected signals [52, 79–81].[1] By adjusting the coupling liquid loss level as well as the separation between the antennas and the enclosure, the power of these reflected waves can be made negligible once arrived at the receiving antennas. This enables the microwave imaging algorithm to assume that the coupling liquid extends to infinity (i.e., Sommerfeld radiation condition). Therefore, the green's function of an unbounded homogeneous medium can be used in the implementation. Due to the convolutional form of such green's function[2], efficient computational solvers, e.g., the method of moments with the conjugate gradient algorithm accelerated by the Fast Fourier transform (CG-FFT MoM) can then be used in the MWI algorithm.

[1] Other methods such as taking into account these reflections in the imaging algorithm or calibration techniques to remove the undesired fields also exist [82, 83], which is not within the scope of this paper.

[2] That is, the green's function will be $g(\mathbf{r}, \mathbf{r}') = g(\mathbf{r} - \mathbf{r}')$ where $\mathbf{r}$ and $\mathbf{r}'$ are the observation and source locations respectively.

However, a lossy coupling liquid not only reduces the level of the reflections from the enclosure but also reduces the level of the *desired* signal. To understand this better let us consider [80] in which water with various additions of table salt was used to create coupling liquids with various loss levels. (The greater the addition of table salt, the more lossy the coupling liquid.) For small addition of table salt, the loss level was not sufficient to reduce the reflections to an acceptable level. On the other hand, beyond a certain level of salt addition, the loss level was too high to the extent that the desired signal was not usable (i.e., a weak signal-to-noise ratio). Therefore, an appropriate loss level between these two limits was chosen to perform imaging. (Typically, in MWI around the frequency of 1 GHz, a loss value corresponding to a conductivity of $\sigma \approx 1 \frac{\mathrm{S}}{\mathrm{m}}$ has been used.) As another example, in [81], the conductivity of $\sigma = 1.13 \frac{\mathrm{S}}{\mathrm{m}}$ has been used for the coupling liquid for microwave breast imaging. These typical values for the conductivity level correspond to the following imaginary part values for the relative complex permittivity of the coupling liquid: between -15 to -20 assuming $\exp(j\omega t)$ time dependency.

In this paper, the purpose is to investigate the use of absorbing metasurfaces as the enclosure of MWI systems in an attempt to relax the necessity of having a high-loss background medium for the imaging system. Electromagnetic metasurfaces [1–3] are thin structures consisting of subwavelength elements with various applications such as tailoring radiation patterns [65], refraction [24], polarization control [84], absorption [10], etc. Once illuminated, electric and magnetic equivalent currents are induced on these electromagnetic metasurfaces that can then tailor the incident electromagnetic wave in various ways. For example, in [28], currents are induced on three layers of metallic dogbone traces on two bonded Rogers RO3010 substrates to refract a normally incident plane wave by 70°. (The thickness of this metasurface is about 2.5 mm at the frequency of 9.53 GHz, i.e., less than $\lambda_0/12$ where λ_0 is the wavelength in free space.) The category of metasurfaces considered herein is the absorbing metasurfaces which are often designed so as to have a small reflection coefficient for a normally incident plane wave [10, 85–87]. For such absorbing metasurfaces,

once the incident plane wave deviates from the normal incidence, the reflection coefficient worsens as compared to the normal incidence.

The potential advantages of these absorbing metasurfaces for microwave imaging system enclosure are the followings.

- They are electrically thin and light weight (e.g., in the order of one or two dielectric substrates). Therefore, they help with the portability of the MWI system;
- They are often metallic backed. Thus, they can shield the MWI system from undesired external interference and cable effects;
- Since the absorption occurs at the metasurface, the loss of the coupling liquid (background medium) can be reduced. This can improve the signal to noise ratio (SNR) of the measured data. (An improved SNR enhances the achievable image resolution and accuracy.)
- When the background medium is air (e.g., see [47]) the absorbing metasurface enclosure still shields the imaging domain from external noise (due to its PEC backed structure), while not creating significant reflections back to the imaging domain.

On the other hand, a disadvantage of an absorbing metasurface enclosure is its limited bandwidth, which inhibits its use in wideband MWI systems. However, it does not create any major issue for narrow-band MWI systems. A second challenge with absorbing metasurfaces is the angular dependency of their absorption. As will be seen, despite their angular dependency, they can still be helpful in reducing the reflections. In what follows, we first go over MWI, and our problem statement as well as some aspects of metasurfaces including their generalized sheet transition conditions in terms of surface susceptibilities. We will then consider three unit cell designs for absorbing metasurfaces which will later be used as our MWI enclosures. Based on these unit cells, we present some synthetic imaging results using these absorbing metasurface enclosures with the data collected in Ansys

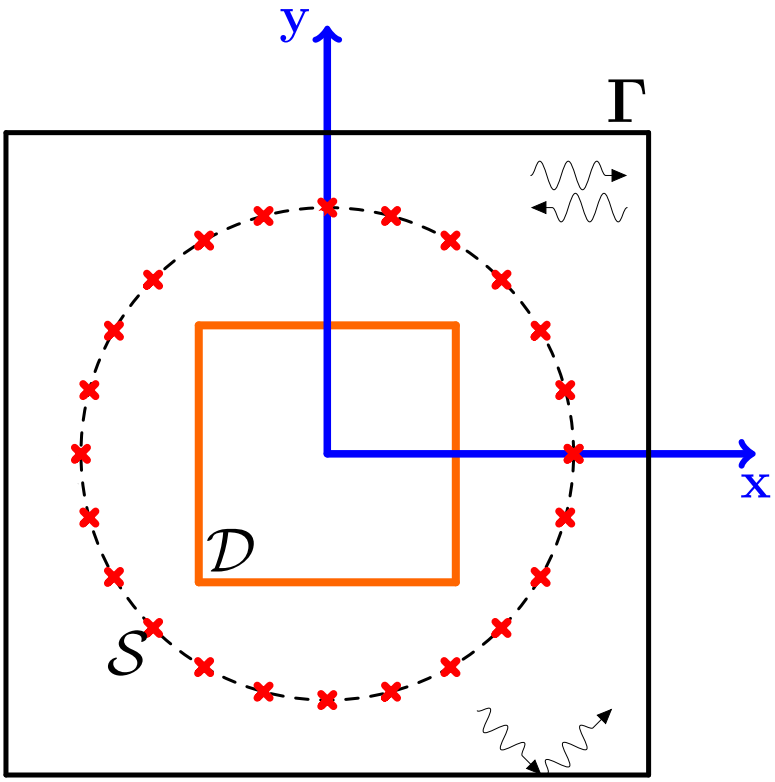

Fig. 4.1: The schematic of a microwave imaging system consisting of three main geometrical domains: (I) the imaging domain $\mathcal{D}$, (II) the measurement domain $\mathcal{S}$ (the red crosses show the locations of antennas on $\mathcal{S}$), and (III) the enclosure of the system Γ. We might have some reflections from Γ back to the imaging environment.

HFSS to demonstrate their performance. Finally, we show a fabricated metasurface and its associated experimental test.

4.2 Microwave Imaging (MWI)

Consider Fig. 4.1 which shows a schematic of a MWI system. The imaging domain, in which the OI resides, is denoted by $\mathcal{D}$. The measurement domain located outside the imaging domain is denoted by $\mathcal{S}$, and represents the location of the transmit/receive antennas. Finally, the enclosure of the MWI system is denoted by Γ. This enclosure, which can for example be plexiglass [47] or metal [52], causes some reflections back to the imaging environment. Under tomographic MWI (i.e., 2D transverse magnetic TM_z propagation),

we assume that the imaging domain lays in the xy plane, and the imaging is performed with the z component of the electric field (and subsequently with the x and y components of the magnetic field). Thus, the main governing equation of the MWI process can be expressed as

$$\begin{aligned} &\nabla^2 E_z^{\text{scat}} + k_b^2 E_z^{\text{scat}} = -k_b^2 w, \text{ (in the imaging system)} \\ &E_z^{\text{scat}} \text{ subject to the boundary condition on } \Gamma \end{aligned} \tag{4.1}$$

where ∇^2 denotes the Laplacian operator, k_b is the wavenumber in the background medium, and w denotes the unknown contrast sources [50] in the OI. Finally, $\boldsymbol{E}^{\text{scat}} = E_z^{\text{scat}}\hat{z}$ denotes the scattered field[3] which has only the $\hat{z}$ component under our tomographic assumption. Assuming that the reflections by the enclosure Γ is small when arrived at the antennas, we can replace the boundary condition in (4.1) by Sommerfeld radiation condition, and arrive at the so-called data equation [50]

$$E_z^{\text{scat}}(\boldsymbol{r} \in \mathcal{S}) = k_b^2 \int_{\mathcal{D}} g(\boldsymbol{r}, \boldsymbol{r}') O(\boldsymbol{r}') E_z(\boldsymbol{r}') d\boldsymbol{r}' \tag{4.2}$$

where g denotes the green's function of the background medium. Due to the assumption that the background medium extends to infinity, we then have

$$g(\boldsymbol{r}, \boldsymbol{r}') = g(\boldsymbol{r} - \boldsymbol{r}') = \frac{1}{4j} H_0^2(k_b|\boldsymbol{r} - \boldsymbol{r}'|), \tag{4.3}$$

where H_0^2 is the zeroth order Hankel function of the second kind. ($\boldsymbol{r}$ and $\boldsymbol{r}'$ denote the position vectors.) In addition, $O(\boldsymbol{r})$ denotes the main unknown of the problem: the relative complex permittivity *contrast* function (object function) defined as

$$O(\boldsymbol{r}) \triangleq \frac{\varepsilon(\boldsymbol{r}) - \varepsilon_b}{\varepsilon_b}, \tag{4.4}$$

[3]The scattered field is defined as the subtraction of the incident field (field in the absence of the OI) from the total field (field in the presence of the OI); i.e., $\boldsymbol{E}^{\text{scat}} \triangleq \boldsymbol{E} - \boldsymbol{E}^{\text{inc}}$.

where ε_b is the relative permittivity of the background medium and ε is the unknown relative complex permittivity of the object being imaged. Finally, $\boldsymbol{E} = E_z\hat{z}$ denotes the induced total field in the imaging domain which is also unknown and is nonlinearly related to O through the so-called domain equation (also known as the state equation) [50]. Due to this nonlinearity, the contrast is updated in an iterative fashion. Two types of algorithms are common in the literature to iteratively reconstruct the relative complex permittivity contrast, namely, Gauss-Newton inversion (GNI) and contrast source inversion (CSI) methods.[4] These methods often use regularization techniques to stabilize the inversion process (i.e., treating the ill-posedness of the problem) and to enhance image quality. A common regularization technique is the weighted L_2 norm total variation multiplicative regularizer which provides both smoothing and edge-preserving operations. Under this regularization, the above two algorithms are referred to as MR-GNI and MR-CSI algorithms [48–50,52,53]. As will be seen in Section 4.7, we use the MR-GNI and MR-CSI algorithms to generate images from microwave scattered data. In all our reconstructions, these algorithms have started from a trivial initial guess which is $O(\boldsymbol{r}) = 0$ for the MR-GNI algorithm, and the back-propagation solution for the MR-CSI algorithm.

[4]In both algorithms, the contrast at the nth iteration is updated as $O_{n+1} = O_n + \beta_n u_n$ where O_n is the known contrast at the nth iteration and β_n is the step length. The vector u_n is the conjugate gradient direction at the nth iteration of the CSI algorithm, and Newton correction at the nth iteration of the GNI algorithm.

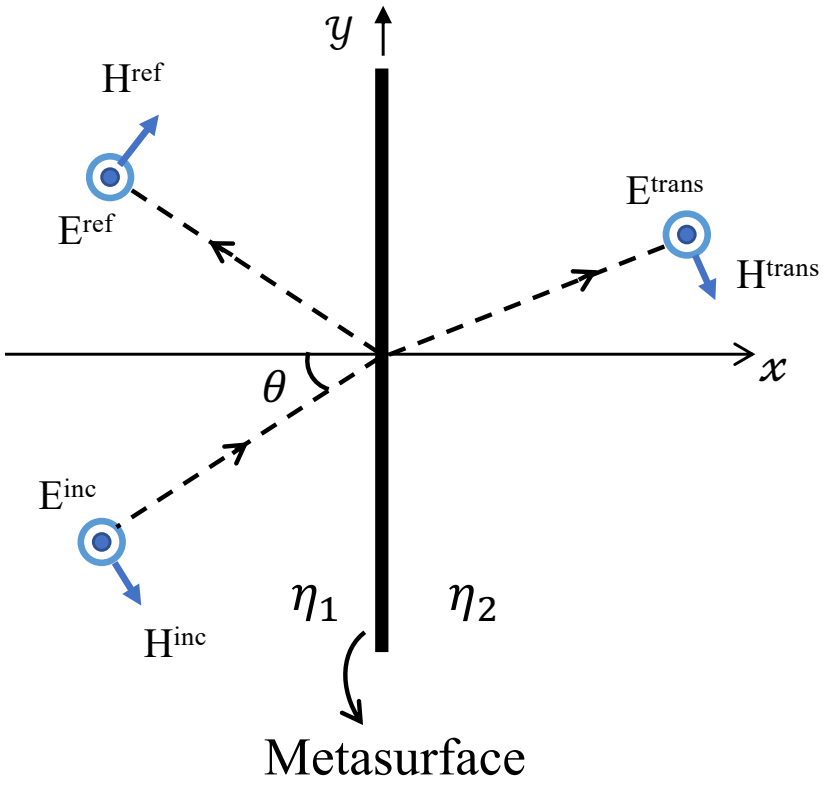

Fig. 4.2: A metasurface is located on the y axis. Thus, the input and output sides of the metasurface are $x = 0^-$ and $x = 0^+$ respectively. A TM_z incident wave illuminates the metasurface which results in reflected and transmitted waves. Also, η_1 and η_2 denote the wave impedance in the two media.

4.3 Problem Statement

Therefore, the main purpose of this paper is to investigate the use of absorbing metasurfaces for the MWI enclosure Γ such that

- we can assume that the background medium extends to infinity, which is equivalent to assuming small reflections from Γ, thus, enabling the use of (4.3) as the green's function in our MWI algorithms;

- the imaging system is shielded from external interference, i.e., utilizing a metallic-backed absorbing metasurface.

For a discussion on the use of conventional absorbers in MWI, see Appendix C.

4.4 Metasurface Theory

Metasurfaces provides a boundary condition for the wave propagation which is described by the generalized sheet transition conditions (GSTCs) [14–16]. Assuming that the metasurface is along the y axis as shown in Fig. 4.2, the GSTCs relate the tangential fields ($\hat{y}$ and $\hat{z}$ components) on both sides of the metasurface as[5]

$$\begin{bmatrix} -\Delta H_z \\ \Delta H_y \end{bmatrix} = j\omega\varepsilon_0 \begin{bmatrix} \chi_{\mathrm{ee}}^{yy} & \chi_{\mathrm{ee}}^{yz} \\ \chi_{\mathrm{ee}}^{zy} & \chi_{\mathrm{ee}}^{zz} \end{bmatrix} \begin{bmatrix} E_y^{\mathrm{av}} \\ E_z^{\mathrm{av}} \end{bmatrix} + j\omega\sqrt{\mu_0\varepsilon_0} \begin{bmatrix} \chi_{\mathrm{em}}^{yy} & \chi_{\mathrm{em}}^{yz} \\ \chi_{\mathrm{em}}^{zy} & \chi_{\mathrm{em}}^{zz} \end{bmatrix} \begin{bmatrix} H_y^{\mathrm{av}} \\ H_z^{\mathrm{av}} \end{bmatrix} \tag{4.5a}$$

$$\begin{bmatrix} \Delta E_z \\ -\Delta E_y \end{bmatrix} = j\omega\mu_0 \begin{bmatrix} \chi_{\mathrm{mm}}^{yy} & \chi_{\mathrm{mm}}^{yz} \\ \chi_{\mathrm{mm}}^{zy} & \chi_{\mathrm{mm}}^{zz} \end{bmatrix} \begin{bmatrix} H_y^{\mathrm{av}} \\ H_z^{\mathrm{av}} \end{bmatrix} + j\omega\sqrt{\mu_0\varepsilon_0} \begin{bmatrix} \chi_{\mathrm{me}}^{yy} & \chi_{\mathrm{me}}^{yz} \\ \chi_{\mathrm{me}}^{zy} & \chi_{\mathrm{me}}^{zz} \end{bmatrix} \begin{bmatrix} E_y^{\mathrm{av}} \\ E_z^{\mathrm{av}} \end{bmatrix} \tag{4.5b}$$

where ω, ε_0, and μ_0 denote the angular frequency, permittivity and permeability of free space respectively. In the above GSTCs, the position vector $\boldsymbol{r}$ has been dropped for brevity. Assuming a given location on the metasurface, say $\boldsymbol{r}$, $\Delta u = \Delta u(\boldsymbol{r})$ (where $u \in \{E_y, E_z, H_y, H_z\}$) represents the difference between the tangential fields on the two sides of the metasurface at $\boldsymbol{r}$; i.e., $\Delta u = u^+ - u^-$ where u^+ is the tangential field on the output side (i.e., on $x = 0^+$) and u^- is the tangential field on the input side (i.e., on $x = 0^-$). On the other hand, $u_{\mathrm{av}} = u_{\mathrm{av}}(\boldsymbol{r})$ is the algebraic average of the tangential fields on both sides; i.e., $u_{\mathrm{av}} = (u^+ + u^-)/2$. Then, according to the GSTCs, these tangential fields are related through the surface susceptibilities at location $\boldsymbol{r}$ denoted by χ where the position vector has been dropped for brevity. These surface susceptibilities represent how an electric (e) or magnetic (m) field excitation (second subscript) in a given direction (second superscript) results in an electric (e) or magnetic (m) polarization response (first subscript) in a

[5]The normal susceptibility components have been ignored for simplicity. For the discussion on these normal susceptibilities see [88]. In addition, the GSTCs may be expressed in terms of surface impedances [29] or polarizabilities [86].

given direction (first superscript). For example, consider χ_{me}^{yz}: it represents how an electric field excitation in the z direction (i.e., second subscript and superscript) creates a magnetic polarization response in the y direction (first subscript and superscript).

Since we are considering tomographic imaging in the xy plane, we limit ourselves to the two-dimensional (2D) transverse magnetic (TM_z)[6] propagation as shown in Fig. 4.2. Thus, we only have three field components, namely E_z, H_y, and H_x. Since H_x is perpendicular to the metasurface, it is absent in the GSTCs. This simplifies (4.5) to

$$\Delta H_y = j\omega\varepsilon_0\chi_{ee}^{zz}E_z^{\text{av}} \; + \; j\omega\sqrt{\mu_0\varepsilon_0}\chi_{\text{em}}^{zy}H_y^{\text{av}}, \tag{4.6}$$

$$\Delta E_z = j\omega\mu_0\chi_{\text{mm}}^{yy}H_y^{\text{av}} + j\omega\sqrt{\mu_0\varepsilon_0}\chi_{\text{me}}^{yz}E_z^{\text{av}}. \tag{4.7}$$

Therefore, the metasurface design problem can be stated as follows: given a set of (desired) tangential fields on both sides of the metasurface, find the surface susceptibility values that satisfy (4.6) and (4.7).

[6]This is referred to as the TE polarized waves case in [89, 90], however, this configuration is relatively widely referred to as TM_z in the microwave imaging community; for example, see [46, 50, 91]. Note that the imaging domain lays in the xy plane and the field components with which we irradiate the object being imaged are E_z, H_x and H_y. Therefore, since $H_z = 0$ it is referred to as TM_z.

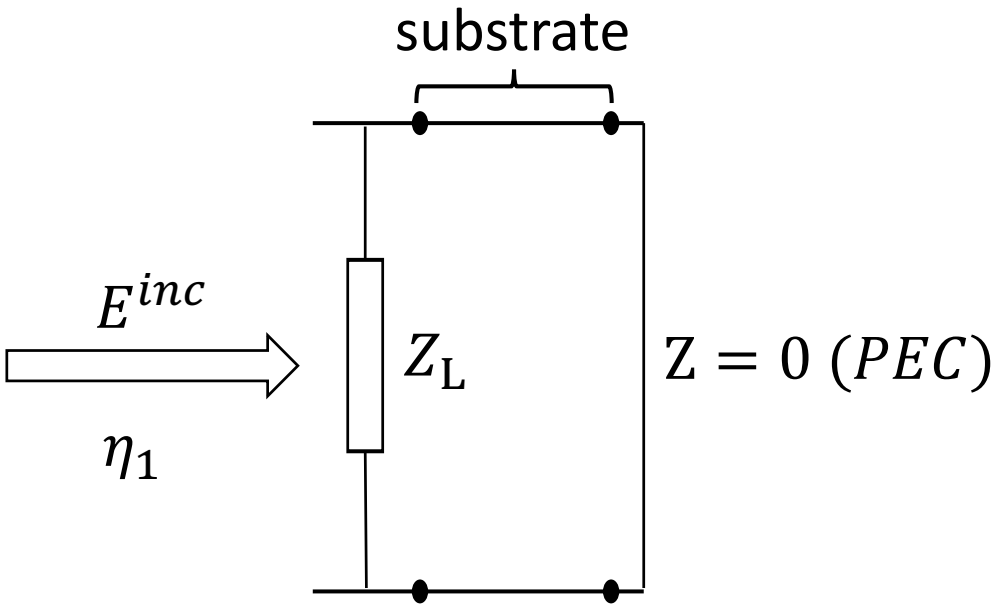

Fig. 4.3: The equivalent circuit form of a unit cell topology for a PEC-backed absorbing metasurface. The complex load Z_{L} may be implemented in different ways.

4.5 Absorbing Metasurface

Let us now apply the above GSTCs to an absorbing metasurface.

4.5.1 Illumination from $x = 0^-$ side

Considering Fig. 4.2, and assuming that the metasurface needs to act as an absorbing metasurface, the desired tangential fields on the input side ($x = 0^-$) of the metasurface must be equal to the incident field since the reflected field must ideally be zero. Therefore, noting that $E^{\mathrm{ref}} = H^{\mathrm{ref}} = 0$, the tangential fields on the input side will be

$$E_z^- = E_z^{\mathrm{inc}} \quad \text{and} \quad H_y^- = -H_y^{\mathrm{inc}} \cos\theta. \tag{4.8}$$

Note that in Section 4.3, we have assumed that the absorbing metasurface is metallic-backed. Assuming a perfect electric conductor (PEC) for the metal, the desired tangential fields on the output side ($x = 0^+$) will be zero; i.e., $E_z^+ = H_y^+ = 0$ (shielding). Since we

now know the tangential fields on both sides of the metasurface, we also know ΔE_z, ΔH_y, E_z^{av} and H_y^{av}. Substituting these into (4.6) and (4.7) and also using the plane wave relation $E^{\text{inc}} = \eta_1 H^{\text{inc}}$, we arrive at

$$\cos\theta = \frac{1}{2} j\omega\varepsilon_0\eta_1\chi_{\text{ee}}^{zz} - \frac{1}{2} j\omega\sqrt{\mu_0\varepsilon_0}\cos\theta\chi_{em}^{zy}, \tag{4.9}$$

$$-\eta_1 = -\frac{1}{2} j\omega\mu_0\cos\theta\chi_{\text{mm}}^{yy} + \frac{1}{2} j\omega\sqrt{\mu_0\varepsilon_0}\eta_1\chi_{me}^{yz}. \tag{4.10}$$

4.5.2 Illumination from $x = 0^+$ side

Let us now assume that an incident field illuminates the metasurface from the other side, i.e., from $x = 0^+$ side. Since we have assumed that the metasurface is PEC-backed, this incident field will be totally reflected (i.e., shielding for the MWI system). Due to the shielding effect of the PEC, the fields on $x = 0^-$ will be zero, i.e., $E_z^- = H_y^- = 0$. In addition, $E_z^+ = 0$, but $H_y^+ \neq 0$. Then, (4.6) and (4.7) turn into

$$H_y^+ = j\omega\sqrt{\mu_0\varepsilon_0}\chi_{\text{em}}^{zy}\frac{H_y^+}{2}, \tag{4.11}$$

$$0 = j\omega\mu_0\chi_{\text{mm}}^{yy}\frac{H_y^+}{2}. \tag{4.12}$$

4.5.3 Required Surface Susceptibilites

From (4.11) and (4.12), we need to have $\chi_{\text{mm}}^{yy} = 0$ and $\chi_{\text{em}}^{zy} = \frac{-2j}{k_0}$. Noting that the reciprocity requires $\chi_{\text{me}}^{yz} = -\chi_{\text{em}}^{zy}$ [16], then we will have $\chi_{\text{me}}^{yz} = \frac{2j}{k_0}$. Finally, χ_{ee}^{zz} can be found from (4.9) as

$$\chi_{ee}^{zz} = -\frac{4j\cos\theta}{\omega\varepsilon_0\eta_1}. \tag{4.13}$$

Noting that $\cos\theta > 0$ and assuming $\eta_1 \in \mathbb{R}$, this set of surface susceptibilities indicates a lossy metasurface as shown in Sec. 2.7 [56, Appendix B], which is expected for power

dissipation.[7]

4.5.4 Angular Dependency

As can be seen from (4.13), the required surface susceptibility χ_{ee}^{zz} depends on the incidence angle θ. Therefore, as it is well-known, the performance of the metasurface will have angular dependency. In MWI, since the object being imaged, represented by $O(\boldsymbol{r})$ in (4.2), is unknown, we cannot predict the incidence angle of the wave impinging on the enclosure Γ. Based on the plane wave spectrum concept [92, Ch. 4], the fields emanating from the object being imaged can be thought as the summation of many plane waves each of which with a different incidence angle. Therefore, ideally, for MWI applications, it is desired to have an angular-independent absorbing metasurface which might be possible with an active metasurface [93]. However, since we use passive metasurfaces, the MWI reconstruction will be prone to this angular dependency. However, note that this angular-dependent absorption is still better than typical casings such as a metallic casing based on the level of the reflected signals.

4.5.5 Unit Cell Topology

It has been shown in [85], [10, Sect. 4], (and references therein) that this type of absorbing metasurfaces can be implemented using the unit cell topology whose equivalent circuit form is shown in Fig. 4.3. As can be seen, this unit cell consists of a PEC-backed dielectric substrate with the load Z_{L} printed on the substrate. Assuming a lossless dielectric substrate and normal incidence ($\theta = 0$), the load Z_{L} will be

$$Z_{\mathrm{L}} = (\frac{1}{\eta_1} - \frac{1}{jZ_{\mathrm{sub}} \tan \beta_{\mathrm{sub}} t})^{-1}, \tag{4.14}$$

[7] The polarizabilities of this type of absorbing metasurfaces have been derived in [10, Appendix A]. These polarizabilities can then be converted to the surface susceptibilities using [57, Sect. 4].

where Z_{sub}, β_{sub}, and t denotes the substrate's characteristic impedance, wavenumber, and thickness respectively. Note that Z_{L} is a complex number. This load can be implemented in different ways, and therefore we may have different unit cell designs to achieve the same Z_{L}.

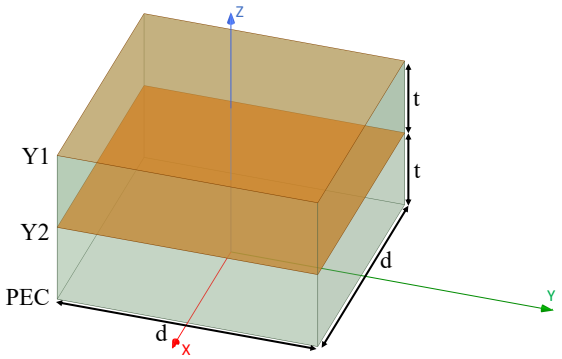

(a) Unit cell of Example I

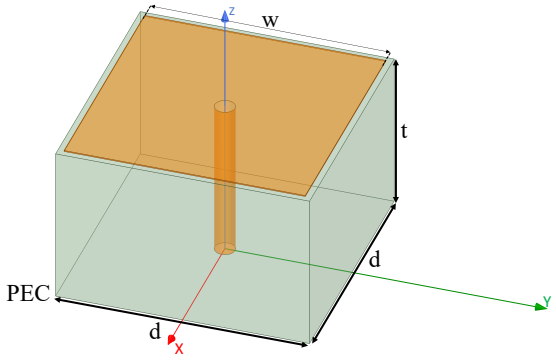

(b) Unit cell of Example II

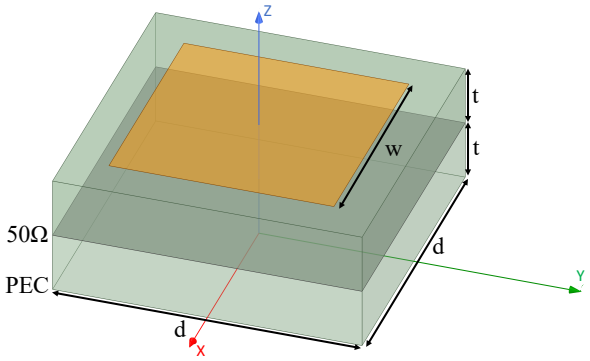

(c) Unit cell of Example III

Fig. 4.4: Three different unit cells for the three different imaging examples. (a) This unit cell consists of two Rogers RO3003 substrates with two admittance sheets denoted by Y_1 and Y_2 which are backed by a PEC plane. The size of the unit cell is denoted by d. The thickness of RO3003 substrate is denoted by t. (b) This unit cell, which is from [87], uses a PEC-backed lossy dielectric substrate of thickness $t = 3$ mm, a $W \times W$ square copper patch ($W = 4.75$ mm), and a cylindrical via of radius 0.2 mm. The unit cell size is $d = 5$ mm. (c) This unit cell consists of two RO3003 substrates. The top layer is a square PEC patch, and the middle layer consists of a resistive sheet.

4.6 Unit Cell Design

As will be seen later on, we will consider three imaging examples. Each of these examples use a different absorbing metasurface. Herein, the unit cell for each of these examples are presented. (Later in Section 4.7, these unit cells will be put together to form the enclosure Γ of the MWI system.) Unit cells are simulated using periodic boundary conditions and Floquet excitation ports in Ansys HFSS. The Floquet ports are placed sufficiently far from the unit cell to not include the effect of evanescent waves. Then, HFSS de-embedding is used to have the reference plane right on the unit cell structure. Due to the use of PEC-backed absorbing metasurfaces, only S_{11} parameter will be considered to represent the reflection coefficient of the metasurface at the frequency of operation.

4.6.1 Unit Cell I

As will be seen in Section 4.7.1, in the first imaging example, the absorbing metasurface needs to work in a background medium with the relative complex permittivity of $75.6 - j4$ (water) at 1 GHz. This specific frequency and background permittivity are chosen based on the fact that in the first imaging example, water is assumed to be our coupling liquid. Note that the loss of the coupling liquid, which is represented by its imaginary part of the complex permittivity, is relatively small. Therefore, in the unit cell design process, ε_b has been assumed to be 75.6 for simplicity. (In the imaging algorithm, the loss of the coupling liquid is taken into account.) The structure of the unit cell employed for the first imaging example is shown in Fig. 4.4(a) which consists of two admittance sheets Y_1 and Y_2. These two admittance sheets along with the PEC ground plane are on two identical Rogers RO3003 substrates with the thickness of $t = 1.52$ mm and the dielectric properties of $\varepsilon_r = 3$ and $\tan\delta = 0.001$. In addition, the size of the unit cell, denoted by d in Fig. 4.4(a), is chosen to be $d = \lambda_\mathrm{b}/10 = 3.45$ mm, where λ_b is the wavelength in the coupling liquid at the imaging frequency.

The design process requires determining the two admittance sheets Y_1 and Y_2. To this

end, the transmission line model is used to determine the input admittance of the unit cell as

$$Y_1 + \{Z_{\rm s}\frac{2j\tan(\beta_{\rm s}t)Z_2 - \tan^2(\beta_{\rm s}t)Z_{\rm s}}{j\tan(\beta_{\rm s}t)Z_{\rm s} + Z_2 - Z_2\tan^2(\beta_{\rm s}t)}\}^{-1}, \tag{4.15}$$

where $Z_{\rm s}$ is the characteristic impedance of the RO3003 substrate[8], $\beta_{\rm s}$ is the wavenumber within the substrate, and $Z_2 = Y_2^{-1}$. This input admittance then needs to be matched with the admittance of the background medium. For the transmission line model, the impedance of the background medium[9] will be $\eta_{\rm b} = 120\pi/(\sqrt{75.6}\cos\theta)$ [62]. Assuming $\theta = 0$ (normal incidence), we then require (4.15) to be equal to $\eta_{\rm b}^{-1}$ (impedance match) which results in

$$Z_1 = Y_1^{-1} = \eta_{\rm b}, \tag{4.16}$$

and

$$Z_2 = Y_2^{-1} = \frac{-jZ_{\rm s}\tan(\beta_{\rm s}t)}{1-\tan^2(\beta_{\rm s}t)}. \tag{4.17}$$

As can be seen, Z_1 and Z_2 are purely resistive and capacitive respectively. In simulation, Z_1 and Z_2 are realized by HFSS impedance boundary conditions. (The values of Z_1 and Z_2 are 43.3278 Ω and $-j12.0559$ Ω). As the incidence angle θ increases, the reflection coefficient ($|S_{11}|$) increases as shown in Fig. 4.5(a).[10] (Due to the use of impedance boundary conditions, as opposed to actual copper traces, this unit cell is less affected by the angular dependency.) Moreover, the frequency response of this unit cell has also been shown in Fig. 4.5(b) demonstrating its narrow bandwidth.

4.6.2 Unit Cell II

As will be seen in Section 4.7.2, the background medium for the second imaging example is air. Even with the air background medium, an enclosure is required to support the

[8] In the design process, $\tan\delta$ of the substrate, which is small, has been ignored for simplicity; however, in the HFSS simulations, it has been considered.

[9] As noted earlier, the imaginary part of the relative complex permittivity of the coupling liquid is ignored in the design process.

[10] Note that this is due to the fact that $\eta_{\rm b}$ will be $120\pi/(\sqrt{75.6}\cos\theta)$ instead of $120\pi/\sqrt{75.6}$.

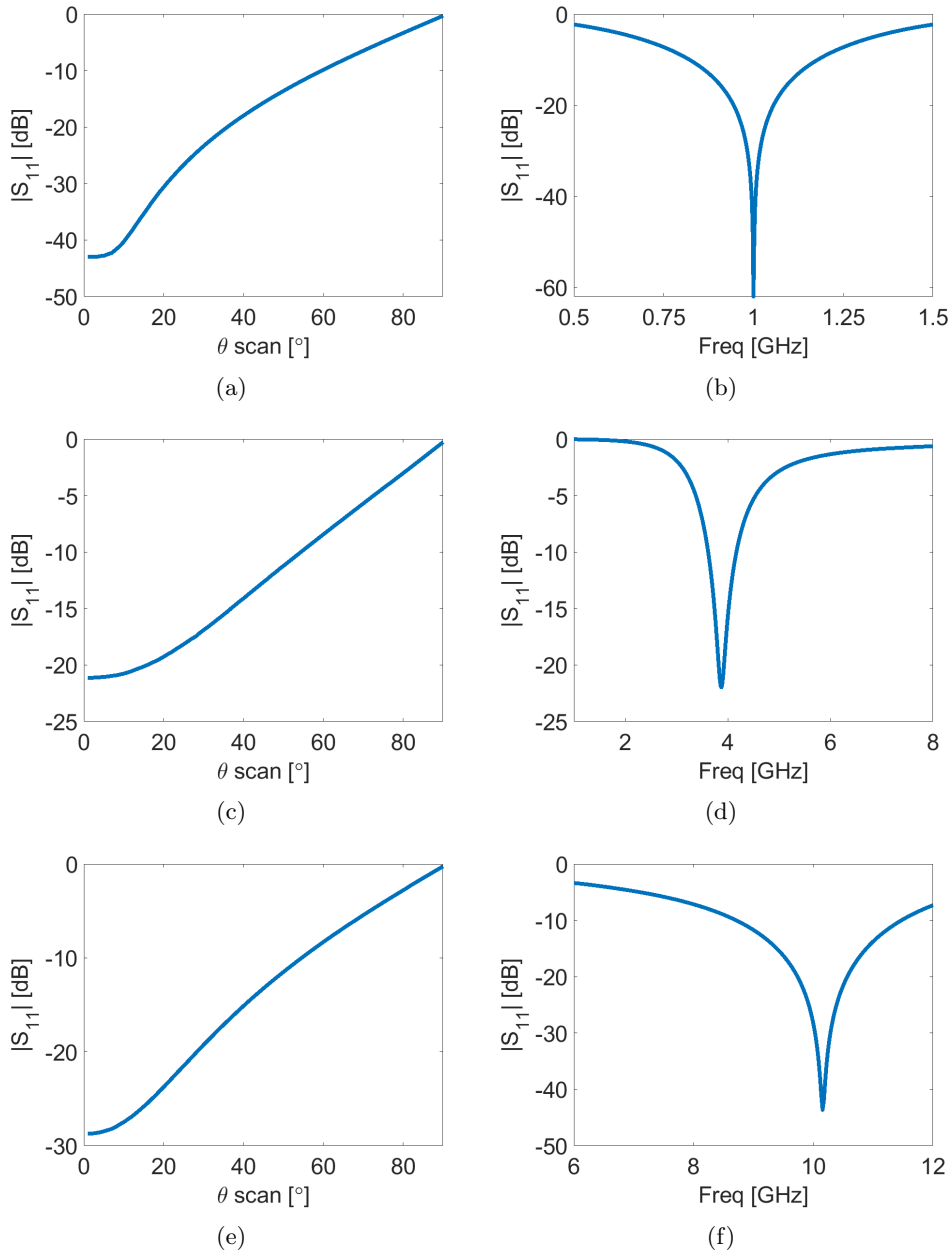

Fig. 4.5: Unit cell performance for the three examples: (Left Column) The reflection coefficient of the unit cell $|S_{11}|$ versus the incidence angle θ. (Right Column) $|S_{11}|$ response versus the frequency of operation (assuming normal incidence). (a)-(b) Example I, (c)-(d) Example II, and (e)-(f) Example III.

system and/or mount the antennas; e.g., see [47] where 24 Vivaldi antennas operating in air have been mounted on a plexiglass enclosure. Herein, we use the mushroom unit cell

proposed in [87] which operates at 3.844 GHz and is shown in Fig. 4.4(b). The mushroom structure consists of (i) a PEC-backed lossy substrate with a relative complex permittivity of $9 - j1.998$, (ii) a 4.75 mm $\times$ 4.75 mm square $\frac{1}{2}$oz (17 μm thickness). copper patch, and (iii) a cylindrical via with the radius of 0.2 mm. In addition, we have $d = 5$ mm and $t = 3$ mm. (The presence of the via makes the performance of the unit cell less angular dependent [87].) The reflection coefficient corresponding to different incidence angles can be found in Fig. 4.5(c). In addition, the frequency response of the unit cell is shown in Fig. 4.5(d).

4.6.3 Unit Cell III

As will be seen in Section 4.7.3, in the third imaging example, the frequency of operation is set to 10 GHz, and the background medium is assumed to be air. For this example, we use a topology similar to Unit Cell I with Rogers RO3003 substrates with only one difference: swapping the capacitive and resistive layers. That is, the top layer is now capacitive with the impedance of jX and the middle layer is now resistive with the impedance of R. (As will be seen in Section 4.8, we use this model for our fabricated metasurface.) From the transmission line model, R and X for the normal incidence and a real-valued $\eta_{\rm b}$ can be found as

$$R = \frac{\eta_{\rm b}\sec^2(\beta_{\rm s}t) \pm \sqrt{\eta_{\rm b}^2\sec^4(\beta_{\rm s}t) - 16Z_{\rm s}^2\tan^2(\beta_{\rm s}t)}}{8}, \tag{4.18}$$

$$X = \frac{\eta_{\rm b}Z_{\rm s}\tan(\beta_{\rm s}t)}{2R - \eta_{\rm b}}. \tag{4.19}$$

Note that the resulting R needs to be purely positive real ($R \in \mathbb{R}^+$) which requires $\eta_{\rm b}^2\sec^4(\beta_{\rm s}t) \geq 16Z_{\rm s}^2\tan^2(\beta_{\rm s}t)$. For a given substrate, this might not hold at certain frequencies. In fact, at our frequency of operation, this condition is not met, and therefore we perform optimization using HFSS to find appropriate values. For the final unit cell design, we use two Rogers RO3003 substrates, each of which with the thickness of $t = 1.52$ mm as shown in Fig. 4.4(c). On the top of the unit cell, there is a 5.73×5.73 mm^2 square

PEC patch, which provides our capacitive value. (The impedance value of the layers can be tested individually, see [28].) Furthermore, at the middle layer, there is a 50 Ω resistive sheet implemented using the HFSS impedance boundary condition.[11] At the bottom layer, there is a PEC layer which shields the metasurface. The unit cell response with respect to angle and frequency sweeps is presented in Figures 4.5(e) and (f) respectively. As can be seen in Fig. 4.5(f), due to the use of an approximated value for the middle layer impedance, the resonance frequency has a slight shift.

4.7 Synthetic Imaging Results

We consider three synthetic targets to demonstrate the performance of the absorbing metasurface enclosures. For all these example, we utilize line sources to illuminate the targets. We then use Ansys HFSS to collect the scattered field data E_z^{scat} on the measurement domain $\mathcal{S}$. These scattered data are then inverted by the imaging algorithm (e.g., the MR-GNI algorithm) to reconstruct the unknown dielectric profile $O(\boldsymbol{r})$ of the target. Since the imaging algorithms assume a 2D TM_z wave propagation, we place the simulation domain between two PEC planes to mimic an infinite length along the z axis, thus, satisfying the assumption for 2D TM_z propagation. To have references for comparison, we perform two other simulations for each target. For the first reference, we replace the absorbing metasurface enclosure with the HFSS perfectly matched layer (PML) boundary condition. The inversion of the data collected under the absorbing metasurface enclosure can then be compared with the inversion of the data collected under the PML boundary condition. For the second reference, we generate the scattered data set using a 2D MoM code that incorporates the green's function denoted in (4.3). The inversion of the data collected under the metasurface enclosure can also be compared with the inversion of the MoM free space data set.

[11] Rogers provides resistive foil on their RO3003 laminate, which comes in 25, 50, and 100 Ω per square (ps). Herein, the 50 Ω resistive sheet is chosen due to its availability and the fact that it results in a reasonable absorption for the normal incidence for this unit cell. As will be seen in Section 4.8, we have used the 50 Ω ps resistive foil for our fabricated metasurface.

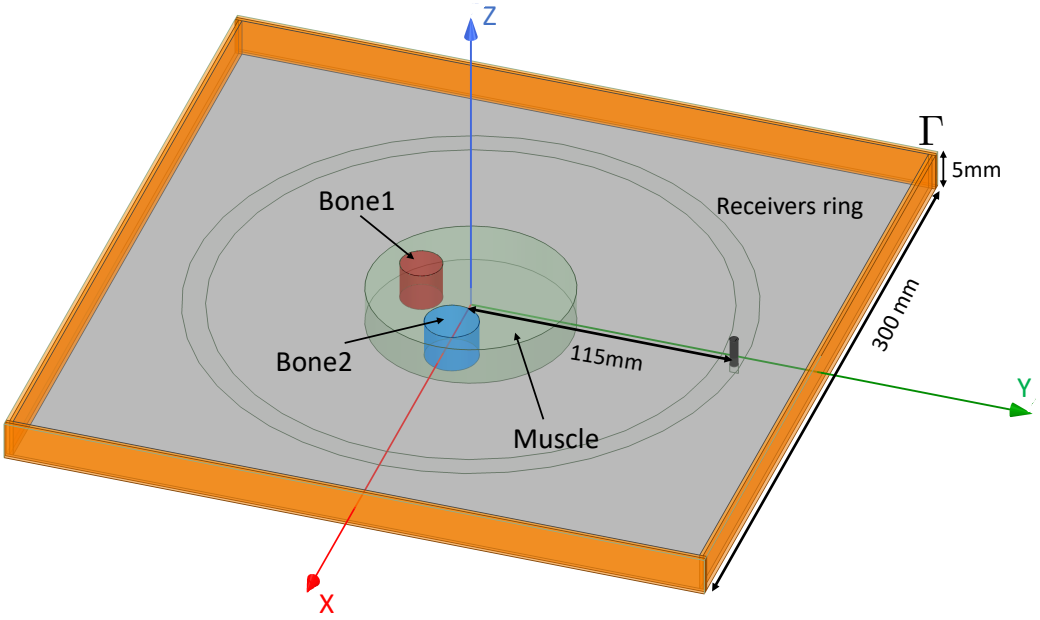

Fig. 4.6: Simulated MWI system for Target I. The enclosure of the system Γ is an absorbing metasurface consists of the unit cell presented in Fig. 4.4(a). The OI consists of a circular muscle tissue and two circular bones. The ring (measurement domain) over which the scattered data are measured and the transmitting line source located on the y axis is also shown.

In addition, note that the scale of the incident field in Ansys HFSS may be different than the scale of the incident field used in the imaging algorithm. To handle this, we utilize the incident field calibration [53,72] for all the data generated by Ansys HFSS. That is, for a given transmitter, we compare the incident field utilized in the imaging algorithm with the incident field in Ansys HFSS over the measurement domain $\mathcal{S}$. From this comparison, for each transmitter, a calibration coefficient is formed to match the maximum of the modeled incident field with that of the HFSS incident field. This calibration coefficients will then be applied to the scattered data collected in Ansys HFSS when that particular transmitter is on. Once this process is done for all the transmitters, we now have our calibrated scattered data which will be given to the imaging algorithm to be inverted.

4.7.1 Target I: Forearm

This target, which has been depicted in Fig. 4.6, consists of three cylinders. The large cylinder represents the muscle tissue that encloses two bone tissue types. The bone tissues which have been denoted by *Bone1* and *Bone2* are depicted in red and blue in Fig. 4.6 respectively. The relative complex permittivity of these two synthetic bones are $\varepsilon_r = 12.36 - j2.79$ and $\varepsilon_r = 20.58 - j6.54$ at 1 GHz respectively. The muscle tissue, shown in yellow, has a relative complex permittivity $\varepsilon_r = 56.66 - j18.60$ at 1 GHz. The radii of the cylinders associated with *Bone1*, *Bone2*, and muscle are 9 mm, 11.5 mm, and 44 mm respectively. This target has been immersed in a low-loss[12] coupling liquid having the relative complex permittivity of $\varepsilon_r = 75.6 - j4.0$ (water) at 1 GHz. The true real and imaginary parts of the relative complex permittivity of this target along with the background medium is shown in Fig. 4.7(a)-(b) respectively. This target is interrogated by 24 transceivers[13] (line sources) residing on receivers ring with the radius of 115 mm which is shown in Fig. 4.6 at 1 GHz. Once one antenna transmits, the emanating E_z field at the other 23 receiving locations are obtained.[14] This process results into 552 (24×23) collected total field data points. Subtracting the incident field E_z^{inc} from the total field data results in 552 scattered data points that are to be processed using an inverse scattering algorithm to yield a quantitative relative complex permittivity image. The imaging domain is a 14×14 cm^2 domain discretized into 80×80 square cells. The MR-GNI inversion results under the PML and the metasurface enclosure have been shown in Figures 4.7(e)-(h). The metasurface enclosure uses the unit cell described in Section 4.6.1 and shown in Fig. 4.4(a). As can be seen, the real-part reconstruction under the metasurface enclosure is close to that under the PML enclosure; however, the imaginary part reconstruction under the PML enclosure outperforms

[12] In previous works [52, 80], the imaginary part of the coupling liquid's relative complex permittivity needed to be about $-j15$ for successful imaging. Therefore, the use of a coupling liquid with an imaginary part of $-j4$ is considered to be low-loss for this imaging problem.

[13] These are not co-resident; thus, challenges such as mutual coupling between the antenna elements are not considered. This is also true for the other examples.

[14] Due to the direct collection of E_z field component, practical issues such as antenna impedance mismatch and mutual coupling are not considered.

the imaginary part reconstruction under the metasurface enclosure. This is expected since the imaginary part reconstruction for biological targets is typically more difficult than the real part reconstruction [94], and often requires better signal-to-noise ratio. We speculate that the $\mathrm{Im}(\varepsilon_r)$ reconstruction for the metasurface case is not as good as that for the PML case is due to the angle-dependency of absorption in the metasurface case. This contributes to the modelling error since the utilized green's function in the MR-GNI algorithm does not take into account such enclosure reflections. Note that the larger element of ε_r is less affected by the SNR value. However, the smaller imaginary parts as compared to larger real parts is more affected for a given SNR. The PML can be considered as an ideal absorbing enclosure. Therefore, its use is almost perfectly aligned with the assumption of unbounded medium green's function in the MR-GNI algorithm, thus, minimizing the modelling error. However, the metasurface due to its angle dependency of absorption naturally results in some modelling error. Therefore, we may think of the PML case as a higher SNR form of the metasurface case. Thus, the reconstructed smaller imaginary part suffers less for the PML case as compared to the metasurface case. Finally, to make sure that the above results are not dependent on this specific imaging algorithm (MR-GNI), we have also inverted the data sets using the MR-CSI algorithm shown in Figures 4.7(g)-(j). As can be seen, the results obtained with the MR-CSI algorithm are consistent with those obtained with the MR-GNI algorithm.

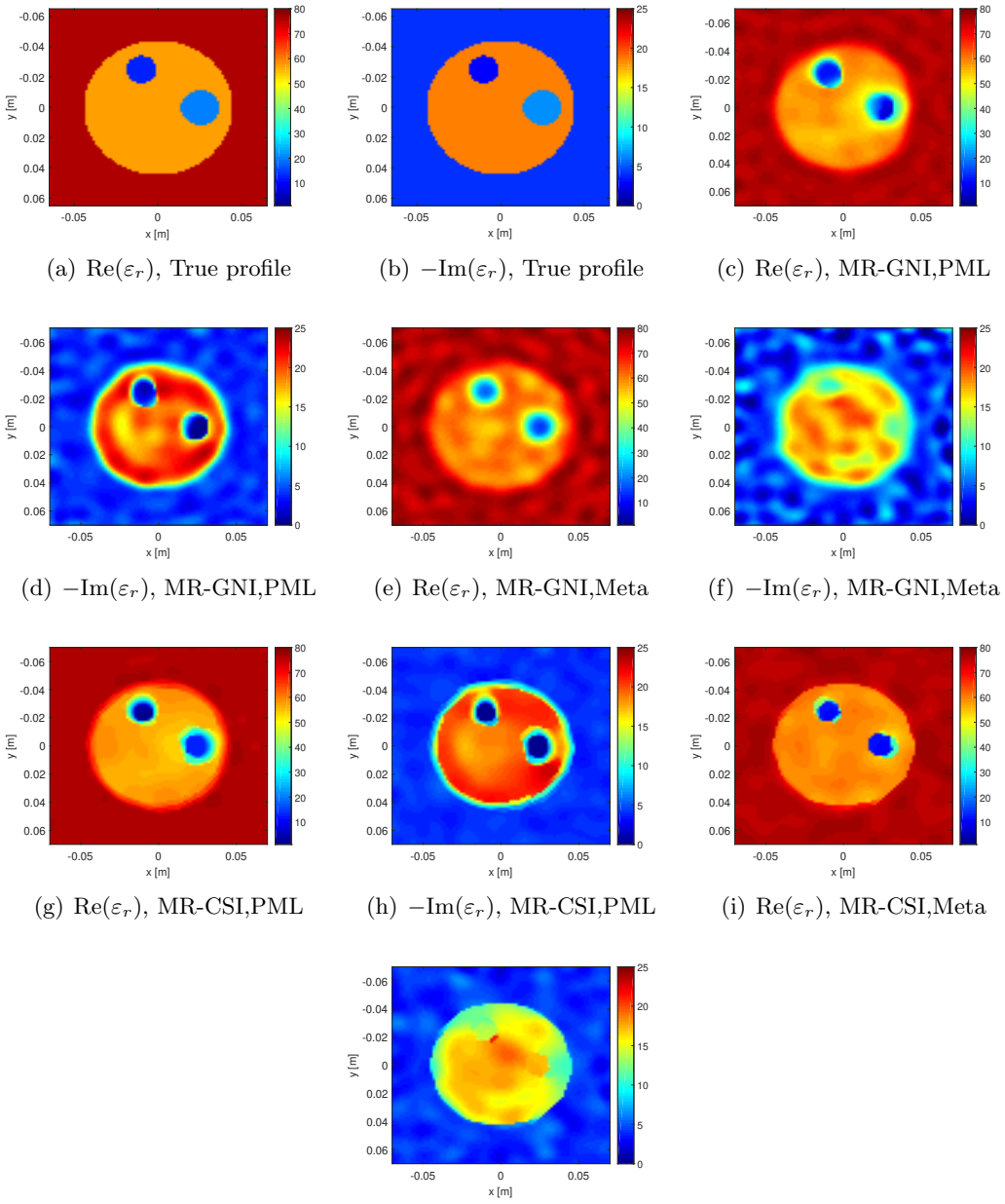

(a) $\mathrm{Re}(\varepsilon_r)$, True profile (b) $-\mathrm{Im}(\varepsilon_r)$, True profile (c) $\mathrm{Re}(\varepsilon_r)$, MR-GNI,PML

(d) $-\mathrm{Im}(\varepsilon_r)$, MR-GNI,PML (e) $\mathrm{Re}(\varepsilon_r)$, MR-GNI,Meta (f) $-\mathrm{Im}(\varepsilon_r)$, MR-GNI,Meta

(g) $\mathrm{Re}(\varepsilon_r)$, MR-CSI,PML (h) $-\mathrm{Im}(\varepsilon_r)$, MR-CSI,PML (i) $\mathrm{Re}(\varepsilon_r)$, MR-CSI,Meta

(j) $-\mathrm{Im}(\varepsilon_r)$, MR-CSI,Meta

Fig. 4.7: (a)-(b) True relative complex permittivity profile for the synthetic human forearm (Target I). ('Re' and 'Im' denote the real-part and imaginary-part operators.) The MR-GNI results under (c)-(d) PML and (e)-(f) metasurface enclosure. The MR-CSI results under (g)-(h) PML and (i)-(j) metasurface enclosure.

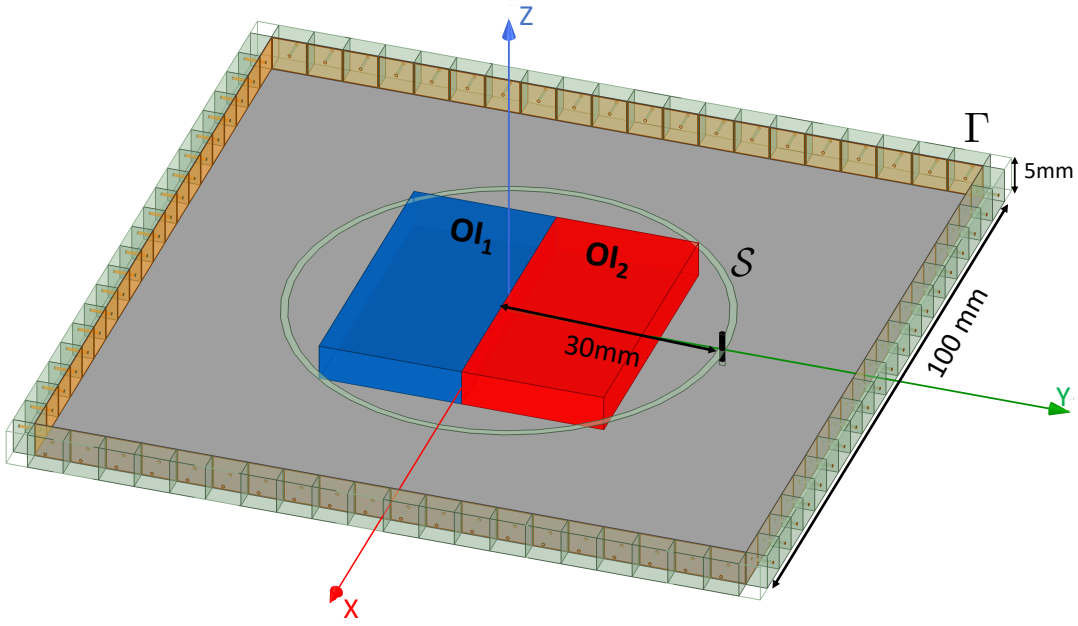

Fig. 4.8: Simulated MWI system for Target II. The enclosure of the system Γ is an absorbing metasurface consists of the unit cell presented in Fig. 4.4(b). The target consists of two lossy dielectric rectangles. The measurement domain $\mathcal{S}$ is also shown.

4.7.2 Target 2: Two rectangular boxes

This target, shown in Fig. 4.8, consists of two attached lossy rectangular dielectric boxes. These two rectangular boxes, denoted by OI_1 (in blue) and OI_2 (in red), have the relative complex permittivity of $\varepsilon_r = 4.0 - j1.0$ and $\varepsilon_r = 3.0 - j0.5$ at the frequency of operation respectively. These two rectangular boxes have the same size of 4×4 cm^2. The background medium in this case study is air. We use 24 transceivers, located on a circle with the radius of 30 mm, to irradiate this target at the frequency of 3.844 GHz. The metasurface enclosure uses the unit cell described in Section 4.6.2 and shown in Fig. 4.4(b). For the spatial prior scenario, the imaging domain size is 4×4 cm^2 discretized into 51×51 square cells. For the general imaging scenario, the imaging domain is 4.2×4.2 cm^2 discretized into 51×51 square cells. The true real and imaginary parts of the relative complex permittivity of this target are shown in Fig. 4.9(a)-(b) respectively. The MR-GNI results for the spatial prior case and the general scenario have been shown in Figures 4.9(c)-(f). As can be seen, the inversion

of the data collected under spatial prior condition is more accurate; however, the inversion of the data collected with the general imaging method still clearly shows the presence of the two dielectric rectangles with reasonable quantitative values. The artefacts are mainly caused by the limited size of imaging domain with regard to the OI. The gap between the edge of OI and imaging domain is only $\frac{\lambda}{75}$, which is too small for the algorithm to resolve the distance. (The MR-CSI results are also consistent with the MR-GNI results, and thus are not shown for brevity.)

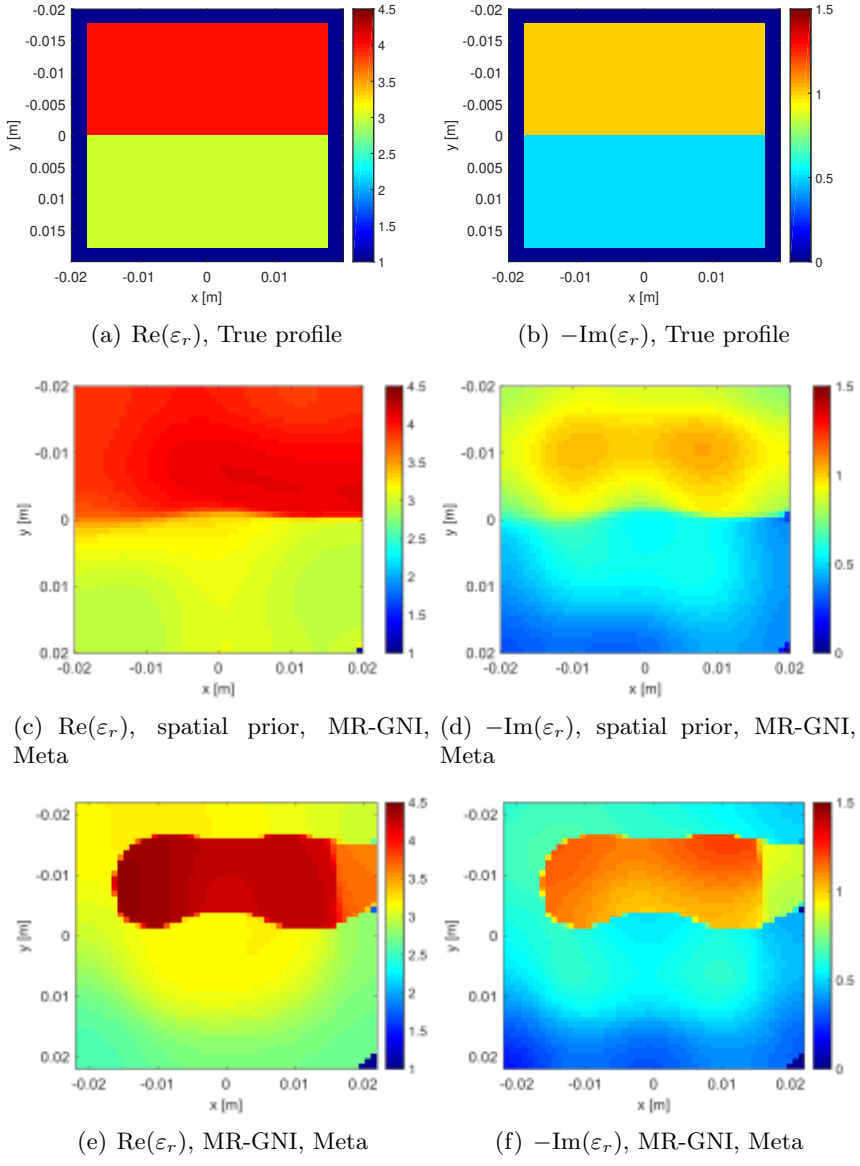

(a) $\mathrm{Re}(\varepsilon_r)$, True profile

(b) $-\mathrm{Im}(\varepsilon_r)$, True profile

(c) $\mathrm{Re}(\varepsilon_r)$, spatial prior, MR-GNI, Meta

(d) $-\mathrm{Im}(\varepsilon_r)$, spatial prior, MR-GNI, Meta

(e) $\mathrm{Re}(\varepsilon_r)$, MR-GNI, Meta

(f) $-\mathrm{Im}(\varepsilon_r)$, MR-GNI, Meta

Fig. 4.9: (a)-(b) True relative complex permittivity profile of Target II. The MR-GNI reconstruction of the data set collected with the metasurface enclosure with dimension of (c)-(d) $40 \times 40\mathrm{cm}^2$ and (e)-(f) $42 \times 42\mathrm{cm}^2$.

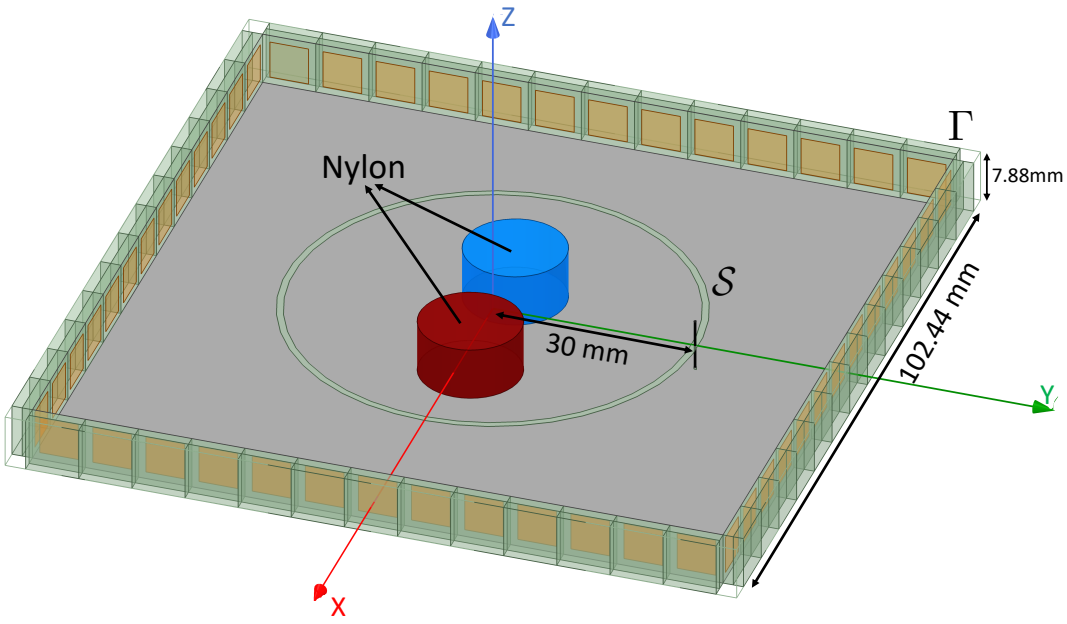

Fig. 4.10: Simulated MWI system for Target III. The enclosure of the system Γ is an absorbing metasurface consists of the unit cell presented in Fig. 4.4(c). The OI consists of two lossless circular cylinders. The measurement domain $\mathcal{S}$ is also shown.

4.7.3 Target 3: Two cylinders

This target, shown in Fig. 4.10, consists of two lossless dielectric cylinders each of which has a radius of 7.5 mm and the relative complex permittivity of $\varepsilon_r = 3.0$ (lossless) at the frequency of operation. These two cylinders have been separated from each other by 5 mm. The background medium in this case study is air. We use 24 transceivers, evenly distributed on a circle with the radius of 30 mm, to irradiate the target at the frequency of 10 GHz. The true target is shown in Fig. 4.11(a). (Since the object is lossless, the imaginary part of the relative complex permittivity is zero and is thus not shown for brevity.) The imaging domain is 3.8×3.8 cm^2 domain discretized into 70×70 square cells.

Three different scattering data sets are considered: (i) free space data set, (ii) data under the PML, and (iii) data under the metasurface enclosure with the unit cells described in Section 4.6.3 and shown in Fig. 4.4(c). The MR-GNI results for these three data sets are shown in Fig. 4.11(b)-(e). As can be seen, the inversion of the free space and PML data sets

are very accurate. In addition, the inversion of the data collected under the metasurface enclosure is also accurate but has some small artefacts.

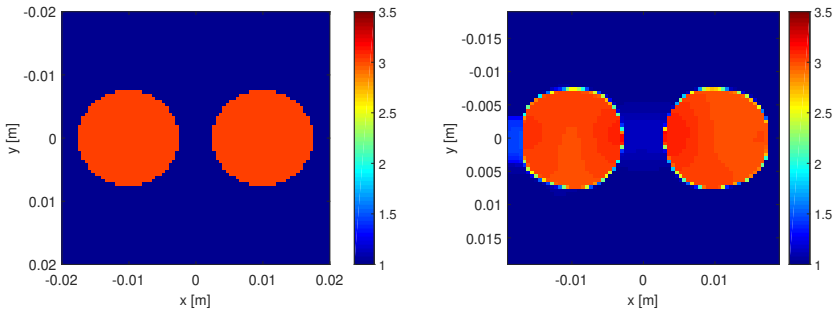

(a) Re(ε_r), True profile

(b) Re(ε_r), MR-GNI, Free space

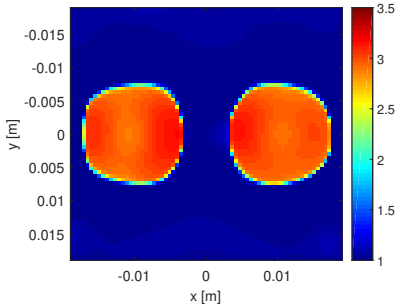

(c) Re(ε_r), MR-GNI, PML

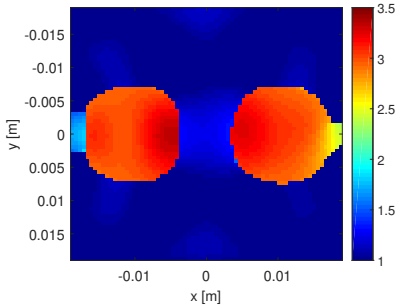

(d) Re(ε_r), MR-GNI, Meta

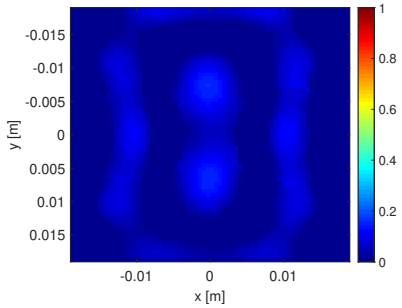

(e) -Im(ε_r), MR-GNI, Meta

Fig. 4.11: (a) True dielectric profile of Target III. (This target is lossless; thus, only one imaginary part of permittivity under metasurface enclosure is shown. Other figures are all for the real part of the permittivity.)The MR-GNI reconstruction of the data collected with the (b) free space condition, (c) PML boundary condition, and (d) real part for metasurface enclosure (e) imaginary part for metasurface enclosure.

4.8 Experimental Results

Herein, we first present the fabricated metasurface and then describe how we have measured its reflectivity for the normal incidence. (For information regarding the horn antenna used in this experiment, see Appendix D.)

4.8.1 Fabrication

An absorbing metasurface based on the configuration of Unit Cell III, described in Section 4.6.3, was fabricated, which is shown in Fig. 4.12(a). This metasurface consists of two Rogers RO3003 substrates (thickness of $t = 1.52$ mm and the dielectric properties of $\varepsilon_r = 3$ and $\tan\delta = 0.001$) which are bonded together by a Rogers RO2929 bondply. This bondply has a relative permittivity of 2.94 and a dissipation factor of 0.003 at 10 GHz. For our fabrication, we have used an RO2929 with the thickness of 3 mil which is about 0.08 mm. The length and width of the substrates are cut to 12 in (30.48 cm) and 9 in (22.86 cm), respectively. On the top substrate, there exist 551 (29×19) $\frac{1}{2}$oz (17 μm thickness) square copper patches. Similar to Section 4.6.3, the size of the patches is chosen to be 5.73×5.73 mm^2 with a separation of 2.15 mm between two neighboring patches. In addition, for ease of handling, some empty space from the outline of the square patches to the board outline has been left.

For the bottom substrate, we have used Rogers RO3003 that comes with a 50 ohms per square (ps) resistive foil. One side of this particular substrate consists of an OhmegaPly RCM, which stands for resistor-conductor material [95]. The other side of this substrate has a typical copper layer. The OhmegaPly layer consists of Nickel Phosphorous (NiP) metal alloy with the thickness of 18μm electrodeposited onto a copper layer [95]. This metal alloy serves as our resistive sheet. For our fabrication, we have removed the copper layer in the vicinity of the resistive foil. However, the other copper layer remains untouched as the absorbing metasurface is a metallic backed structure.

For the top substrate, we have used a typical RO3003 substrate (i.e., without any

resistive foil). For our fabrication, the copper layers on both sides of the top substrate have been removed. This top substrate is then bonded (using 3 mil Rogers RO2929 bondply) to the bottom substrate so as to form the final metasurface shown in Fig. 4.12(a). Thus, in summary, our metasurface consists of the followings

$$\begin{aligned}\text{Metasurface } &= \text{Copper layer (ground)} + \text{ RO3003 dielectric} \\ &+ 50\Omega \text{ ps Resistive foil } + \text{ RO2929 bondply} \\ &+ \text{ RO3003 dielectric } + \text{ Copper patches.}\end{aligned}$$

Finally, to experimentally evaluate the performance of the metasurface, we place it within an absorber panel as shown in Fig. 4.12(b). Based on this placement, we now merely see the array of 29×19 square patches.

4.8.2 Measurements

The schematic of the measurement setup is presented in Fig. 4.13 where a horn antenna is used to irradiate the metasurface. (Visually, we have tried to have the metasurface and the horn aperture in parallel.) The distance between the horn aperture to the metasurface is 66 cm.[15] The horn is fed through Port 1 of a vector network analyzer (VNA) which in our case is a Keysight PNA Network Analyzer N5224B. Fig. 4.14(a) shows the irradiation of the metasurface by the horn antenna assuming the normal incidence. One-port calibration (from 8 GHz to 12 GHz with 6401 points, 0 dBm power level, and an IF bandwidth of 10 KHz) was performed to have the reference plane at the feeding point of the horn antenna. The time-domain feature of the VNA was used to find the reflectivity of the metasurface, similar to [96]. Turning on the time-domain option, we noticed a reflected signal greater than -60 dB at around 5.19 nsec. Given that the distance from the feeding point (VNA calibrated reference plane) to the horn aperture is about 13 cm, the total round-trip distance

[15] At the frequency of 10 GHz, this distance corresponds to about 22λ where λ denotes the wavelength of operation. In addition, the $2D^2/\lambda$ far-field criterion where D denotes the maximum size of the horn antenna is about 58 cm. Therefore, based on the above two criteria, we can assume that the metasurface is in the far-field zone of the horn antenna.

from the reference plane to the metasurface will then be $2 \times (66 + 13)$ or 158 cm which corresponds to an arrival time of about 5.27 nsec. Therefore, we were convinced that this is the reflection emanating from the metasurface. The time gating[16] was then applied from 4.5 nsec to 7.5 nsec. That portion of this time interval which corresponds to reflections greater than or equal -70 dB is shown in Fig. 4.15(a) in blue (dashed curve). To be able to compare this reflection with a reference metallic reflecting surface, we place copper tape in front of the absorbing metasurface as shown in Fig. 4.14(b). Using the same time gating, the reflection emanating from this metallic surface is shown in Fig. 4.15(a) in red (solid curve).[17] In addition, to have a "free space" reference, we remove the metasurface from the absorber panel, thus, now having an absorber panel with a rectangular opening. To minimize possible reflections from the wall and nearby objects going toward the horn antenna through this rectangular opening, we then place an extra absorber panel behind the rectangular opening as shown in Fig. 4.14(c). We refer to this case as the "free space" case. Using the same time gating as above, the reflection from this configuration is shown in Fig. 4.15(a) in green (dotted curve). By comparing the three curves in Fig. 4.15(a), we can easily see that the reflection emanating from the metasurface (as a function of time) is smaller than that of the metallic surface but greater than the reflection in the free space case.

Having time gating on, we then go back to the frequency domain and look at the reflection coefficient as a function of frequency for both the absorbing metasurface (blue) and copper tape (red) as well as the free space (green) cases as shown in Fig. 4.15(b). As can be seen, around the frequency of 9.63 GHz, the absorbing metasurface has about 33 dB less reflection as compared to the reflection from the copper tape case. In addition, at the same frequency, the reflection from the metasurface is very similar to the reflection associated with the free space case. These two comparisons confirm that this is the operational frequency

[16]For the time gating, we have used the following VNA settings: *Gate Type* and *Gate Shape* are set to *Band Pass* and *Normal* respectively.

[17]To prevent the fabricated metasurface from possible damages, we just place the copper tape in front of the metasurface without peeling off its paper-backing. Therefore, the copper tape does not sit completely flush on the surface of the metasurface.

of the fabricated metasurface.

Finally, to compare the experimental performance of this metasurface with its simulated data, we need to calibrate our measured data. To this end, knowing that the reflection coefficient from a perfect electric conductor must be 0 dB, we apply additive calibration numbers (in dB) to each reflection value of the copper tape case (red) shown in Fig. 4.15(b) so as to convert it to a flat line at 0 dB as a function of frequency. We then apply the same additive calibration numbers to the curve associated with the reflections from the metasurface as a function of frequency. This will result in the blue curve (dashed) shown in Fig. 4.15(c) which is referred to as the calibrated reflection and varies from about -2 dB to -33 dB. The simulated reflection from this metasurface using Ansys HFSS has also been shown in red (solid) in Fig. 4.15(c)[18]. As can be seen, the simulated data has a similar trend to the measured data with the main difference being the shift in its frequency of operation. We speculate that one reason behind this shift in the operational frequency could be due to the change that the resistive value may undergo in the fabrication process. To investigate this possibility, we have performed simulations with four different sheet resistance values. As can be seen in Fig. 4.16, the calibrated measured reflection, shown in dashed (dark) blue, is quite close to the simulation result if the sheet resistance is considered to be 60 ohms per square (dashed-dot black) as opposed to the original 50 ohms per square (solid red).

[18]Note that as opposed to the simulation result presented in red in Fig. 4.15(c), the simulation result shown in Fig. 4.5(f) does not take into account the bondply, and also assumes PEC for the copper patches.

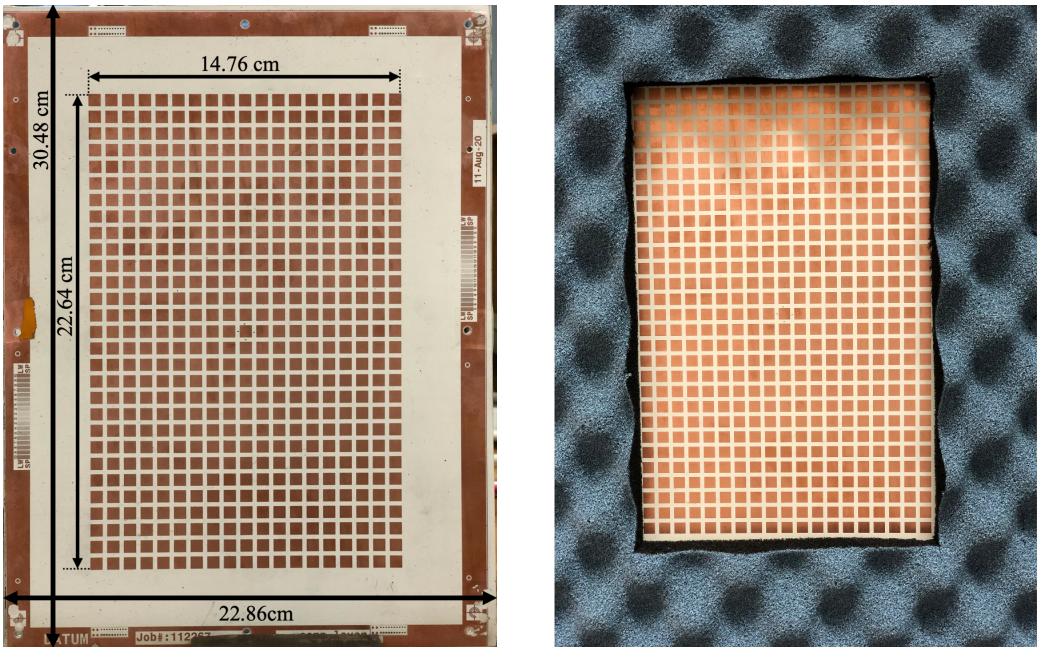

(a) (b)

Fig. 4.12: (a) The fabricated metasurface which uses two Rogers RO3003 substrates, one of which including a $50\ \Omega$ per square resistive foil bonded by an RO2929 bondply and (b) the same fabricated metasurface placed in an absorber panel to cover its margins, thus, only exposing its 29×19 square patch array.

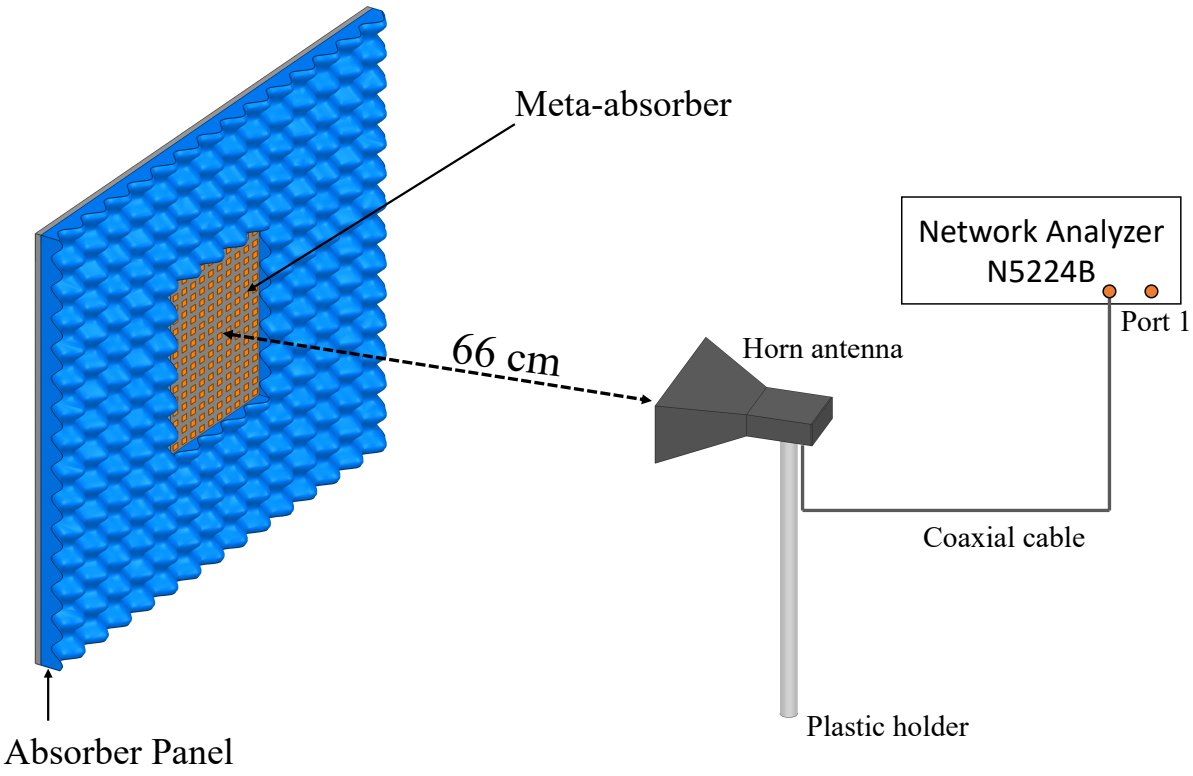

Fig. 4.13: The measurement setup. A horn antenna is used to irradiate the metasurface. A vector network analyzer, using its time-domain option (time gating), records the reflected signal from the metasurface for the normal incidence.

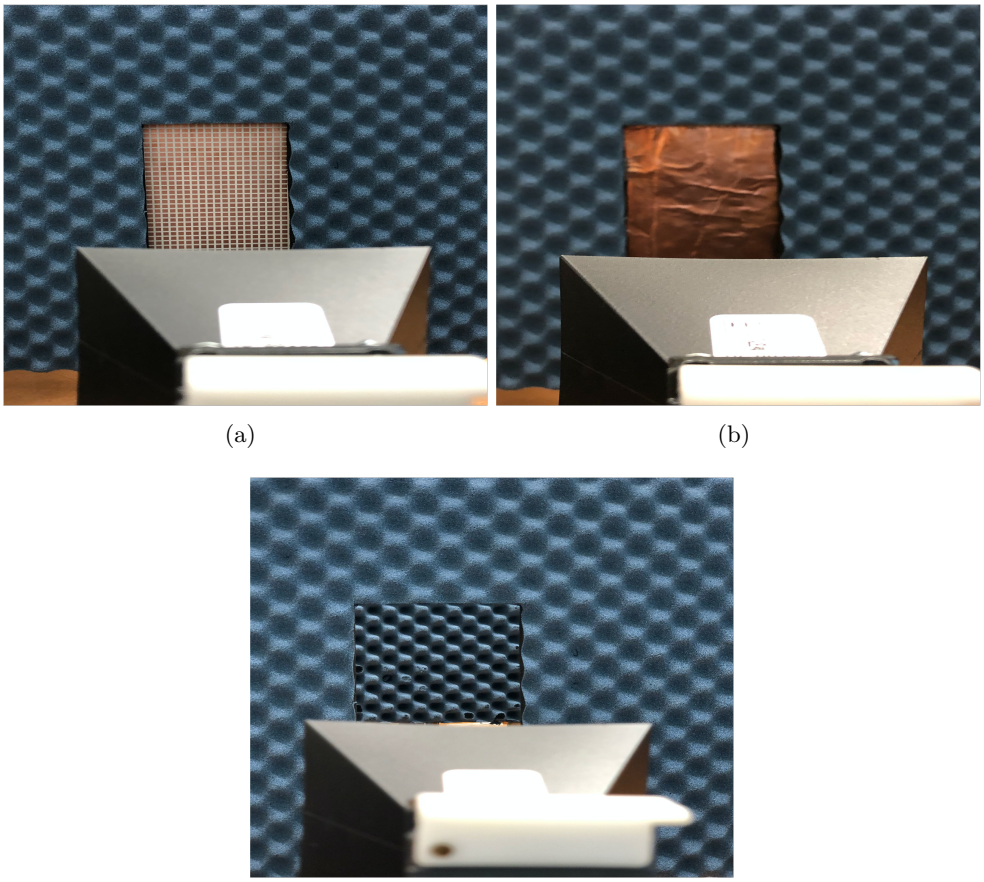

(a) (b)

(c)

Fig. 4.14: Horn antenna irradiating (a) the metasurface and (b) the copper tape placed in front of the metasurface. In the last case, i.e., the "free-space" case shown in (c), we have removed the metasurface from the absorber panel, thus having an absorbing panel with a rectangular opening. To reduce the reflections due to this opening, an extra absorbing panel has been placed behind the rectangular opening in (c).

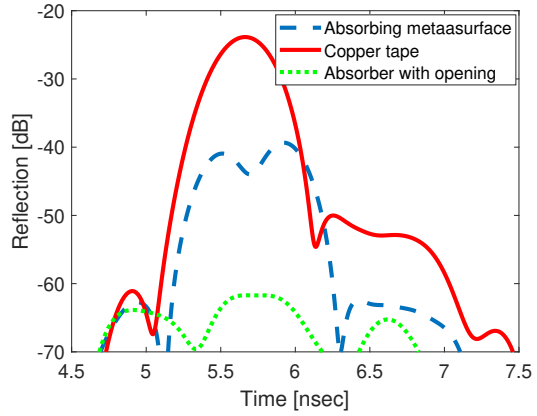

(a)

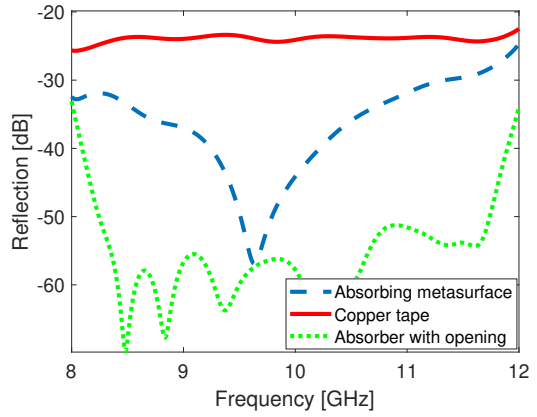

(b)

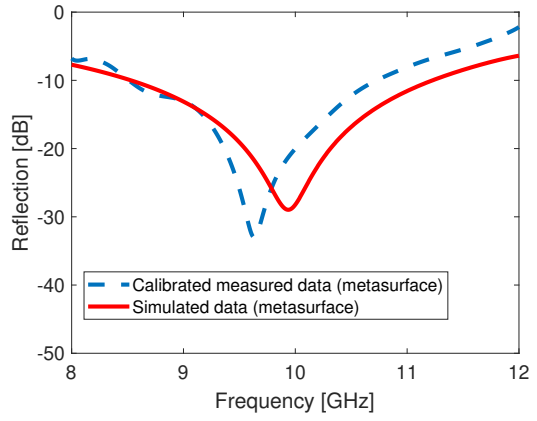

(c)

Fig. 4.15: (a) The reflection as a function of time for the absorbing metasurface, copper tape, and free space cases within the time gating interval. (b) The reflection as a function of frequency for these three cases when the time gating is on. (c) The calibrated measured reflection from the absorbing metasurface compared to its corresponding simulated data in Ansys HFSS.

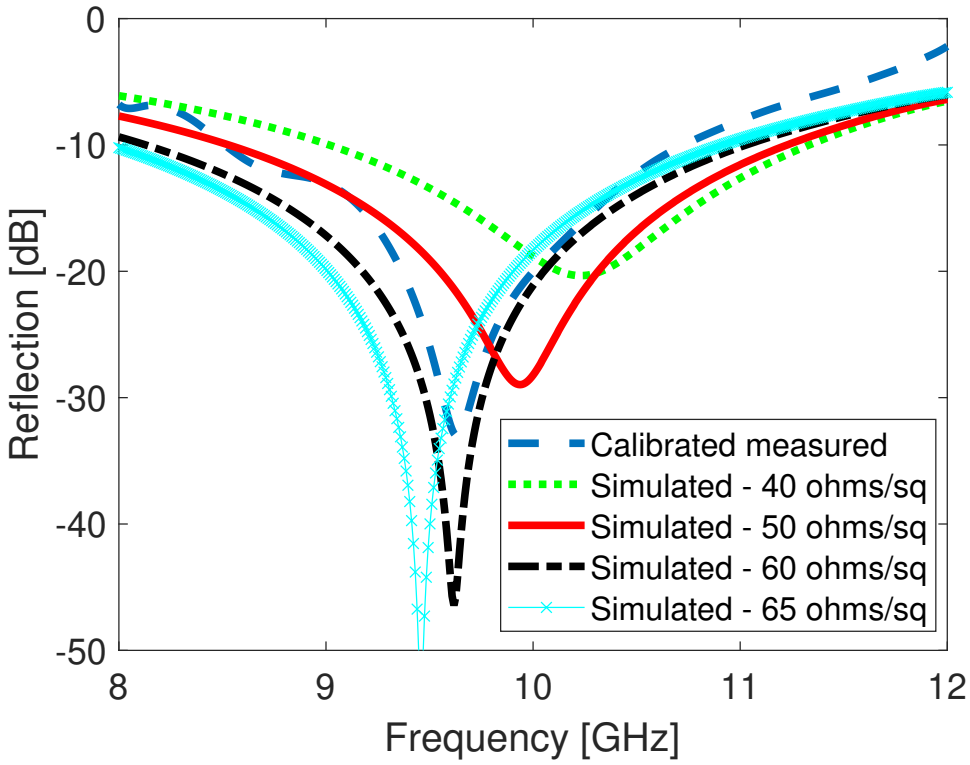

Fig. 4.16: The calibrated measured reflection from the absorbing metasurface compared to its corresponding simulated data in Ansys HFSS for varying sheet resistance value from 40 ohms per square to 65 ohms per square.

4.9 Conclusion

In MWI system design, it is often desired (i) to reduce the reflections happening at the enclosure of the imaging system, and (ii) to shield the imaging chamber from external interference. To this end, one option is to use a metallic enclosure in conjunction with a lossy coupling liquid such as salt water. The undesired reflected waves from the enclosure will then need to go through a lossy background medium to arrive back at the receivers, thus being weakened. The main advantage of this approach is the simplicity of its implementation which has also shown successful experimental imaging results. On the other hand, its main disadvantage is its negative effect on the desired signal level, and consequently worsening the overall signal-to-noise ratio of the measured data. This paper proposes an alternative approach which does not require a lossy background medium. To this end, PEC-backed absorbing metasurfaces were utilized as the enclosure of simulated MWI systems. The PEC-backed structure shields the imaging chamber from external interference. In addition, the absorbing metasurface reduces the level of the reflected waves from the enclosure. This approach comes with its own disadvantage: narrow bandwidth. In addition, the absorption of these metasurfaces is a function of incidence angles, which is a challenge for complex scattering events in the imaging chamber. To alleviate this in this paper, the transmitting antenna was placed not too close to the metasurface enclosure.

Herein, three different unit cell models have been considered. Except Unit Cell II, the other two models use Ansys HFSS' impedance boundary conditions for the implementation of the resistive layer (and, the capacitive layer in Unit Cell I). It is expected that these simple models produce better results than what can be obtained using practical implementations of the resistive and capacitive components. Therefore, the imaging results obtained under these simulated metasurfaces need to be treated as the upper bounds of the achievable image accuracy. Nevertheless, this paper shows that the use of absorbing metasurfaces in microwave imaging can be useful for shielding the imaging system from external interference, and at the same time, reducing the undesired reflections from the system casing. In

particular, for those microwave imaging applications where the background medium must be air and yet the system needs to be shielded by an enclosure, such PEC-backed absorbing metasurfaces can be employed as the system enclosure.

Finally, an absorbing metasurface using two bonded Rogers substrates was fabricated and measured for the normal incidence. The preliminary results are promising. However, we still need to experimentally investigate the performance of this absorbing metasurface in an imaging chamber, which is a much more complex environment, to see how close this enclosure can mimic a free space condition while still shielding the imaging chamber from external interference.

Chapter 5

Matching Metasurfaces in Microwave Imaging

Preface

In this chapter, metasurfaces are proposed to be used as impedance matching transformers to better couple microwave energy into the object of interest (OI) for microwave imaging (MWI). Firstly, the objectives and the motivations behind this work are described in Section 5.1 which is followed by a brief discussion for the theory of MWI. Secondly, the GSTCs for matching metasurfaces based on the surface susceptibility model is presented in Section 5.2 Thirdly, three unit cell topology designs are proposed for matching metasurfaces in Section 5.3. Fourthly, the matching metasurfaces are used in conjunction with simulated MWI as impedance transformers to better couple microwave energy into the OI; the synthetic imaging results are presented in Section 5.4. Finally, one matching metasurface example is fabricated and measured for the normal incidence in Section 5.5.

The material presented in this chapter is based on a conference paper submitted to the 2021 IEEE AP-S Symposium on Antennas and Propagation and USNC-URSI Radio Science Meeting [74]:

- Ziqi Liu and Puyan Mojabi, "Investigating the Use of Matching Metasurfaces in Microwave Imaging," *IEEE AP-S Symposium on Antennas and Propagation and USNC-URSI Radio Science Meeting (Submitted)*, Singapore, Dec 2021.

Consequently, some of the sentences, paragraphs, and figures of this chapter might be identical to the above paper.

5.1 Introduction

Microwave imaging (MWI) is an imaging modality that can use inverse scattering algorithms to reconstruct images of the relative complex permittivity profile of an object of interest (OI) [42–46, 97]. To successfully reconstruct images, it often requires that the OI is interrogated with a sufficient (and, safe) level of electromagnetic power such that the resulting scattered field data are sensitive to the OI's features of interest. For example, consider MWI of human forearms at 1 GHz where the forearm is modeled merely by muscle tissue with a relative complex permittivity ε_r of $56.7 - j18.6$. For a normally incident plane wave, the (Fresnel) reflection coefficient at the air-muscle interface (assuming half spaces) will be about 77%. Alternatively, if we use water as the background medium (with an ε_r of $75.6 - j4$), the reflection coefficient will be about 9%. This shows the importance of using a proper background medium to achieve sufficient interrogation. Thus, matching fluids (also known as coupling fluids) are often used to couple microwave energy into the OI. The main advantage of using matching fluids is that the interrogation is angle independent. On the other hand, the disadvantages are that (i) matching fluids must be contained within a chamber, and changed regularly, especially for biomedical applications such as breast imaging, (ii) it might not be practical to immerse a given OI in the fluid, and (iii) the fluids are often lossy, so they affect the signal-to-noise ratio of the measured data. By employing matching metasurfaces as impedance transformers [25, 98] for interrogation of the OI in WMI, the necessity of having matching fluids can be removed or alleviated.

As described in Chapter 2, electromagnetic metasurfaces [1–3] are structures of sub-

wavelength thickness consisting of a set of sub-wavelength unit cells, which can achieve various functionalities such as polarization control [7, 8] and wavefront manipulation [6, 31, 65]. The metasurfaces considered in this chapter are matching metasurfaces that serve as impedance transformers between two different media [25,98,99]. For example, a recent work has demonstrated a wideband metasurface to match the impedance of two dielectric media for normal plane wave incidence [25]. The proposed metasurface has a wire-loop topology, in which it consists of one substrate and two layers. The topology is straightforward due to that the wire and the loop directly control the electric and magnetic currents across the metasurface. In another work, a design approach to tailor wavefront in two different media is presented [98]. In this work, a focused beam has been formed by illuminating a normally incident plane wave on matching metasurfaces when passing from air ($\varepsilon_r = 1$) into water($\varepsilon_r = 78$) without incurring reflections. In a different work, matching metasurfaces have been proposed for the purpose of stroke detection in microwave brain imaging [73]. These approaches, however, do not focus on the angle dependency of metasurfaces. On the other hand, in MWI, we need to not only couple the incident field into the OI, but also extract the scattered fields outside the imaging domain. Due to the OI being unknown, this is a more complex environment. Thus, we need to perform at least one of the followings: (i) make the metasurfaces angle independent, (ii) take the angle dependency into account in the inverse scattering algorithms, (iii) use calibration techniques to alleviate angle dependency. In this work, we use the scattered field calibration technique [72] to alleviate the angle dependency issue. This scattered field calibration is done by placing a known object in the imaging domain and compare its measured scattered fields at each receiver with those simulated by the forward solver. A set of complex-valued calibration factors is formed for each receiver, and the angle dependency can be alleviated by applying these calibration coefficients to the data collected from the OI.

The advantages of using matching metasurfaces are the followings:

- Metasurfaces are thin and light weight. To have a widely accessible MWI systems,

the system needs to be portable and light.

- Metasurfaces are easy to fabricate in microwave frequencies. It can be done by standard printed circuit board (PCB) fabrication.

- They alleviate the necessity of having a relatively lossy coupling liquid. This can improve the signal-to-noise ratio, and thus enhances the overall performance.

In addition to their angle dependency, another disadvantages of the matching metasurface considered herein is its narrow bandwidth, which is not a major issue for narrowband MWI systems. In addition, our proposed structures are planar, and cannot be conformed to an arbitrary shape of OI.

In our approach, we still contain the OI in a MWI chamber with a low-loss matching fluid, but the transceivers are placed outside the container in air. The matching metasurfaces are attached on the container and used for illumination and reception. Thus, the OI is interrogated by an incident plane wave illuminated from one side and the scattered field data are collected by a set of receivers on the opposite side (along a straight line orthogonal with the incidence wave propagation path). The scattered fields are then processed by an inversion algorithm, named Gauss-Newton inversion (GNI), with spatial priors under the assumption of infinite background medium [100]. This inverse scattering algorithm involves a nonlinear inverse scattering process and a regularization scheme that takes into account prior information about the object being imaged.

Let us now review the microwave imaging formulation with a particular focus on the setup to be considered in this chapter. A schematic of an MWI system is shown in Figure 5.1. In our case, the OI is interrogated by an incident plane wave. The OI resides in the imaging domain denoted by $\mathcal{D}$. The enclosure of the MWI system is denoted by Γ. In this study, it is assumed that the enclosure is not shielded (no metallic layers); thus, the energy can get out of Γ and be collected by the receiver antennas located along a straight line just outside Γ. This collection line is referred to as the measurement domain $\mathcal{S}$.

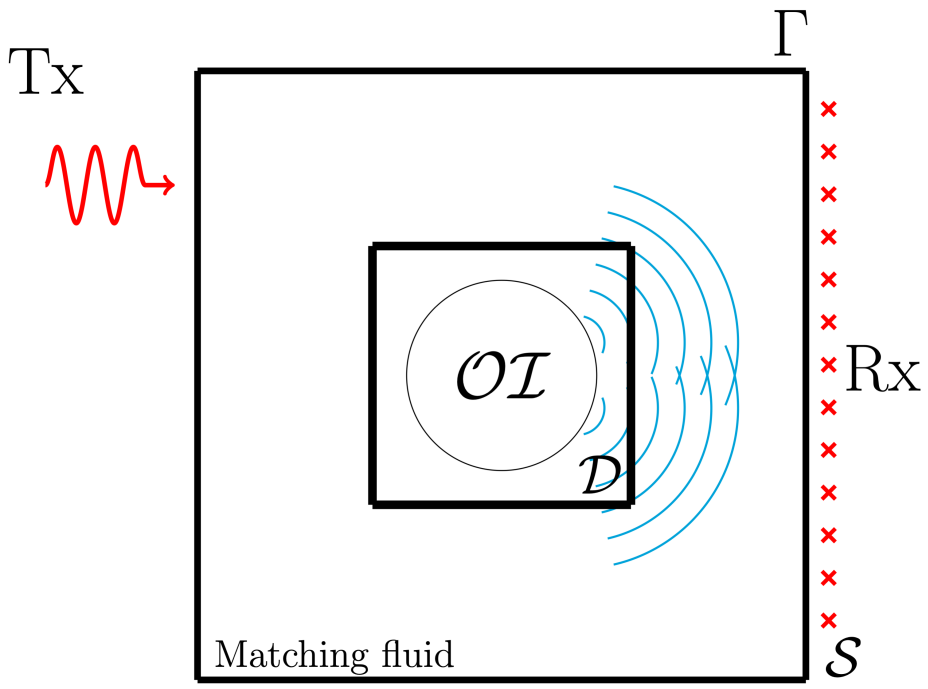

Fig. 5.1: The schematic of the MWI which is interrogated by a incident plane wave. The system consisting of three domains: (I) the imaging domain $\mathcal{D}$, (II) the measurement domain $\mathcal{S}$ (the red crosses show the locations of antennas on $\mathcal{S}$), and (III) the enclosure of the system Γ. We might have some reflections from Γ back to the imaging environment.

To couple the irradiating energy into the OI, matching fluids are often used and contained in the enclosure. For example, for biological tissues imaging, like human forearm, water can be used as the coupling liquid [52]. One option is to have a plexiglass enclosure [47, 101]. Let us now assume that a plexiglass enclosure has been used to contain the water as the matching fluid of the system and the antennas are located outside the enclosure in the air. Due to the impedance mismatch of the matching fluid with the enclosure and the outside medium (air), most of the energy are reflected at the air-plexiglass-water interface. To alleviate this, matching metasurfaces can be used as impedance transformers in MWI to couple microwave energy into the imaging domain.

For simplicity, we consider a TM_z MWI system where the imaging domain lies in the xy plane, and the material and source are invariant with respect to the z direction. Consequently, under the TM_z polarization, we have E_z, H_x, and H_y components. Therefore,

we can formulate the scattering problem merely in terms of the E_z component. To review what was noted in Section 3, we write the equation that governs the scattered field in this MWI system as

$$\begin{aligned} &\nabla^2 E_z^{\text{scat}} + k_b^2 E_z^{\text{scat}} = -k_b^2 w, \text{ (in the imaging system)} \\ &\text{subject to the 'Appropriate Boundary Conditions' (or ABCs)} \end{aligned} \tag{5.1}$$

As noted in (3.4), w denotes the contrast sources [50] in the OI which can be expressed as

$$w(\boldsymbol{r}) \triangleq O(\boldsymbol{r}) E_z(\boldsymbol{r}) \tag{5.2}$$

where $\mathbf{r}$ is the position vector. $O(\boldsymbol{r})$ denotes the relative complex permittivity contrast of the OI and expressed as

$$O(\boldsymbol{r}) \triangleq \frac{\varepsilon(\boldsymbol{r}) - \varepsilon_b}{\varepsilon_b} \tag{5.3}$$

where ε_b is the relative permittivity of the background medium and ε is the unknown relative complex permittivity of the OI.

If the contrast is too large, e.g., greater than 4, it will be difficult for the inverse scattering algorithms to reconstruct the permittivity distribution. One reason behind this difficulty is reflection at the permittivity discontinuity interface. This is the main reason of using matching metasurfaces in MWI.

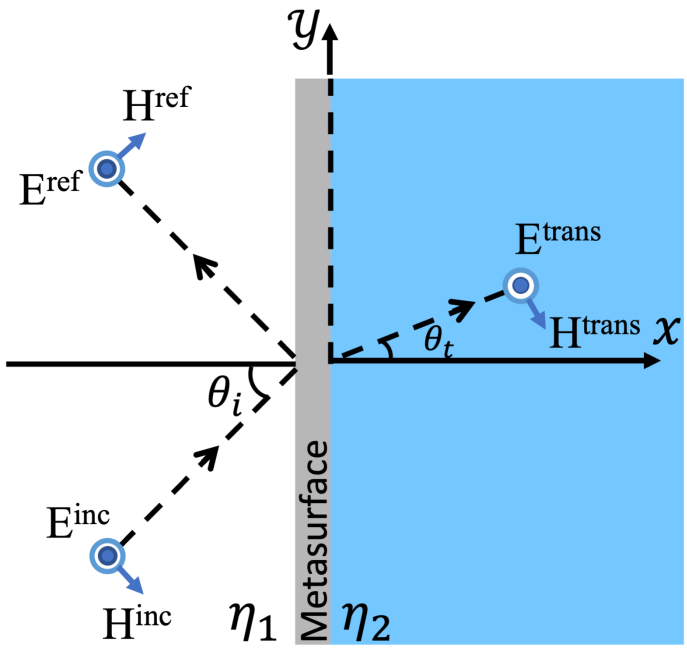

Fig. 5.2: A metasurface is located along the y axis, and a TM_z wave illuminate the metasurface from the left side, which can result in transmission and reflection. Additionally, η_1 and η_2 denote intrinsic impedances of the two media, respectively.

5.2 Matching Metasurface Theory

As described in Chapter 2, a metasurface provides a boundary condition that relates the tangential electric and magnetic fields on the both sides of metasurface. This is expressed by the generalized sheet transition conditions (GSTCs) [11, 15, 16, 27]. Let us assume that the metasurface is along the y axis and the wave propagates in the two-dimensional (2D) TM_z mode. That is, the electrical field is along the z axis (E_z) and the tangential magnetic field on the metasurface is along the y axis (H_y) as shown in Fig. 5.2. Herein, in order to perfectly match the medium impedance on both sides of the metasurface, the reflected field must be ideally zero.

As noted in Chapter 2, metasurfaces can be categorized into mono-anisotropic and bi-anisotropic. Bi-anisotropic metasurfaces have asymmetric structures and provide an extra degree of freedom to manipulate electromagnetic field properties. Let us now review this

within the context of impedance transformer.

As noted in Section 2.4, the GSTCs for mono-anisotropic metasurfaces under the TM_z propagation case will be

$$\Delta H_y \;=\; j\omega\varepsilon_0\chi_{\mathrm{ee}}^{zz}E_{z,av} \tag{5.4a}$$

$$\Delta E_z \;=\; j\omega\mu_0\chi_{\mathrm{mm}}^{yy}H_{y,av} \tag{5.4b}$$

We may then write the above equation as

$$H_y^+ \;-\; H_y^- \;=\; A\chi_{\mathrm{ee}}^{zz}(E_z^+ \;+\; E_z^-) \tag{5.5}$$

$$E_z^+ \;-\; E_z^- \;=\; C\chi_{\mathrm{mm}}^{yy}(H_y^+ \;+\; H_y^-) \tag{5.6}$$

where $A = \frac{j\omega\varepsilon_0}{2}$ and $C = \frac{j\omega\mu_0}{2}$ are used for notation simplicity. By re-arranging the above GSTCs to impedance parameters of a two-port circuit network, the GSTCs can be rewritten as

$$\begin{bmatrix} E_z^- \\ E_z^+ \end{bmatrix} \;=\; \begin{bmatrix} \overbrace{-1 - AC\chi_{\mathrm{ee}}^{zz}\chi_{\mathrm{mm}}^{yy}}^{Z_{11}} & \overbrace{-1 + AC\chi_{\mathrm{ee}}^{zz}\chi_{\mathrm{mm}}^{yy}}^{Z_{12}} \\ \underbrace{-1 + AC\chi_{\mathrm{ee}}^{zz}\chi_{\mathrm{mm}}^{yy}}_{Z_{21}} & \underbrace{-1 - AC\chi_{\mathrm{ee}}^{zz}\chi_{\mathrm{mm}}^{yy}}_{Z_{22}} \end{bmatrix} \begin{bmatrix} H_y^- \\ -H_y^+ \end{bmatrix} \tag{5.7}$$

As can be seen, $Z_{11} = Z_{22}$. This shows that the structure of the metasurface is symmetric.

Furthermore, the image impedances at the input and output ports denoted by Z_{i1} and Z_{i2} respectively[1] for a two-port network can be expressed as [25]:

$$Z_{i1} \;=\; \sqrt{\frac{Z_{11}}{Z_{22}}(Z_{11}Z_{22} \;-\; Z_{12}Z_{21})} \tag{5.8}$$

$$Z_{i2} \;=\; \sqrt{\frac{Z_{22}}{Z_{11}}(Z_{11}Z_{22} \;-\; Z_{12}Z_{21})} \tag{5.9}$$

[1]The procedure to find the image impedances are as follows. If we terminate port 2 with a load impedance equal to Z_{i2}, the impedance seen from port 1 is Z_{i1}, and similarly, if we terminate port 1 with a load impedance equal to Z_{i1}, the impedance seen from port 2 is Z_{i2}.

A reciprocal and full-transmission (i.e., matched) metasurface requires $Z_{i1} = Z_{01}$ and $Z_{i2} = Z_{02}$. Since we are considering two different media, $Z_{01} \neq Z_{02}$; therefore, Z_{i1} and Z_{i2} must be naturally different. However, as this network is symmetric and reciprocal (i.e., $Z_{11} = Z_{22}$ and $Z_{12} = Z_{21}$), the image impedances are identical. Therefore, the above matched condition cannot be met. To handle this problem, another degree of design freedom, which is magnetoelectric coupling, is needed to fulfill this requirement.

Now that we know that the design of a matching metasurface is not possible using the mono-anisotropic metasurface, let us turn our attention to bi-anisotropic metasurfaces. To this end, the desired scattering parameters for the equivalent two-port network of the metasurface unit cell should be [25]

$$[S]^{\text{desired}} = \begin{bmatrix} 0 & 1e^{j\varphi} \\ 1e^{j\varphi} & 0 \end{bmatrix} \tag{5.10}$$

where φ is the phase shift across the metasurface, and the unity (1) shows 100% transmission for S_{21} and S_{12}.

Herein, for simplicity, we assume the surrounding media are lossless with purely real medium impedance values. Under the TM_z illumination, the impedance values on the left and right sides of the metasurface can be expressed as $Z_{01} = \frac{\eta_1}{\cos\theta_i}$ and $Z_{02} = \frac{\eta_2}{\cos\theta_t}$ respectively [62] where θ_i and θ_t are the incident and transmit angles as shown in Figure 5.2. (η_1 and η_2 are the intrinsic impedances of the two media.) Furthermore, with the input and output impedance representations, the desired S parameters (5.10) can be converted to equivalent desired impedance parameters (Z) or transmission parameters (T) [68]. For example, the desired Z parameters can be written as [25]

$$[Z]^{\text{desired}} = \begin{bmatrix} jZ_{01}\cot\varphi & \frac{j\sqrt{Z_{01}Z_{02}}}{\sin\varphi} \\ \frac{j\sqrt{Z_{01}Z_{02}}}{\sin\varphi} & jZ_{02}\cot\varphi \end{bmatrix} \tag{5.11}$$

Now let us turn our attention to the GSTCs. For the TM_z case shown in Fig. 5.2, the

GSTCs for a reciprocal Omega-bianisotropic metasurface can be expressed as

$$\hat{x} \times \Delta H_y \;=\; j\omega\varepsilon_0\chi_{\mathrm{ee}}^{zz}E_{z,av} \;+\; j\omega\sqrt{\mu_0\varepsilon_0}\chi_{\mathrm{em}}^{zy}H_{y,av} \tag{5.12}$$

$$\Delta E_z \times \hat{x} \;=\; j\omega\mu_0\chi_{\mathrm{mm}}^{yy}H_{y,av} \;+\; j\omega\sqrt{\mu_0\varepsilon_0}\chi_{\mathrm{me}}^{yz}E_{z,av} \tag{5.13}$$

As noted in Chapter 2, under the reciprocity assumption, $\chi_{\mathrm{em}}^{zy} = -\chi_{\mathrm{me}}^{yz}$. To map the GSTCs with impedance parameters of a two-port network [26], (5.12) can be rewritten as

$$\begin{bmatrix} E_z^- \\ E_z^+ \end{bmatrix} \;=\; \begin{bmatrix} Z_{11} & Z_{12} \\ Z_{21} & Z_{22} \end{bmatrix} \begin{bmatrix} H_y^- \\ -H_y^+ \end{bmatrix} \tag{5.14}$$

where

$$Z_{11} = \frac{-AC\chi_{\mathrm{ee}}^{zz}\chi_{\mathrm{mm}}^{yy} - \left(1 + B\chi_{\mathrm{em}}^{zy}\right)^2}{2A\chi_{\mathrm{ee}}^{zz}} \tag{5.15a}$$

$$Z_{12} = \frac{AC\chi_{\mathrm{ee}}^{zz}\chi_{\mathrm{mm}}^{yy} + \left(B\chi_{\mathrm{em}}^{zy}\right)^2 - 1}{2A\chi_{\mathrm{ee}}^{zz}} \tag{5.15b}$$

$$Z_{21} = \frac{AC\chi_{\mathrm{ee}}^{zz}\chi_{\mathrm{mm}}^{yy} + \left(B\chi_{\mathrm{em}}^{zy}\right)^2 - 1}{2A\chi_{\mathrm{ee}}^{zz}} \tag{5.15c}$$

$$Z_{22} = \frac{-AC\chi_{\mathrm{ee}}^{zz}\chi_{\mathrm{mm}}^{yy} - \left(B\chi_{\mathrm{em}}^{zy} - 1\right)^2}{2A\chi_{\mathrm{ee}}^{zz}} \tag{5.15d}$$

where we have assumed $A = \frac{j\omega\varepsilon_0}{2}$, $B = \frac{j\omega\sqrt{\mu_0\varepsilon_0}}{2}$, and $C = \frac{j\omega\mu_0}{2}$ for the simplicity of notation.

By equating (5.15) with the desired Z parameters (5.11), the surface susceptibilities for lossless reciprocal Omega-bianisotropic matching metasurfaces under the TM_z illumination and lossless medium assumption can be obtained in terms of the input and output wave impedances (Z_{01} and Z_{02}), and the phase shift (φ) as[2]

$$\chi_{\mathrm{ee}}^{zz} = \frac{2}{\omega\varepsilon_0}\frac{2\sqrt{Z_{01}Z_{02}}\sin\varphi - (Z_{01}+Z_{02})\cos\varphi\sin\varphi}{2Z_{01}Z_{02}\sin^2\varphi - \frac{(Z_{01}-Z_{02})^2}{2}\cos^2\varphi}, \tag{5.16a}$$

[2]In [25], the relation among lossless medium impedances, phase shift of metasurface, surface parameters is presented based on surface impedance model with normal incidence.

$$\chi_{\rm mm}^{yy} = \frac{2}{\omega\mu_0}\frac{2\sqrt{Z_{01}Z_{02}}\sin\varphi - (Z_{01}+Z_{02})\cos\varphi\sin\varphi}{2\sin^2\varphi - \frac{(Z_{01}-Z_{02})^2}{2Z_{01}Z_{02}}\cos^2\varphi}, \tag{5.16b}$$

$$\chi_{\rm em}^{zy} = \frac{2j}{\omega\sqrt{\varepsilon_0\mu_0}}\frac{2\sqrt{Z_{01}Z_{02}}\cos\varphi - (Z_{01}+Z_{02})\cos^2\varphi}{(Z_{01}-Z_{02})\cos^2\varphi - 4\frac{Z_{01}Z_{02}}{Z_{01}-Z_{02}}\sin^2\varphi}, \tag{5.16c}$$

$$\chi_{\rm me}^{yz} = -\chi_{\rm em}^{zy} \tag{5.16d}$$

Note that the relation among the surface susceptibilities, phase shift, input and output medium impedances shown in (5.16) is only valid for a reciprocal, lossless, and zero-reflection Omega-bianisotropic metasurface under the TM_z illumination in lossless media.

To implement the above surface susceptibilites, we can use the cascaded layer topology described in Section 2.5. To remind the reader, we briefly explain the procedure here. The GSTCs are re-arranged as

$$\begin{bmatrix} E_z^- \\ H_y^- \end{bmatrix} = \begin{bmatrix} T_{11} & T_{12} \\ T_{21} & T_{22} \end{bmatrix} \begin{bmatrix} E_z^+ \\ H_y^+ \end{bmatrix} = \begin{bmatrix} 1 & 0 \\ Y_1 & 1 \end{bmatrix} [M] \begin{bmatrix} 1 & 0 \\ Y_2 & 1 \end{bmatrix} [N] \begin{bmatrix} 1 & 0 \\ Y_3 & 1 \end{bmatrix} \begin{bmatrix} E_z^+ \\ H_y^+ \end{bmatrix} \tag{5.17}$$

where according to (2.42)

$$T_{11} = -\frac{AC\chi_{\rm ee}^{zz}\chi_{\rm mm}^{yy} + (1+B\chi_{\rm em}^{zy})^2}{AC\chi_{\rm ee}^{zz}\chi_{\rm mm}^{yy} + (B\chi_{\rm em}^{zy})^2 - 1} \tag{5.18a}$$

$$T_{12} = \frac{2C\chi_{\rm mm}^{yy}}{AC\chi_{\rm ee}^{zz}\chi_{\rm mm}^{yy} + (B\chi_{\rm em}^{zy})^2 - 1} \tag{5.18b}$$

$$T_{21} = \frac{2A\chi_{\rm ee}^{zz}}{AC\chi_{\rm ee}^{zz}\chi_{\rm mm}^{yy} + (B\chi_{\rm em}^{zy})^2 - 1} \tag{5.18c}$$

$$T_{22} = -\frac{AC\chi_{\rm ee}^{zz}\chi_{\rm mm}^{yy} + (1-B\chi_{\rm em}^{zy})^2}{AC\chi_{\rm ee}^{zz}\chi_{\rm mm}^{yy} + (B\chi_{\rm em}^{zy})^2 - 1} \tag{5.18d}$$

and the 2×2 matrices M and N describe the utilized substrates with their expressions given in (2.55a). In addition, Y_1, Y_2, and Y_3 are the admittances of the three layers as described in Section 2.5.

As described in Section 2.5, the required admittance value of each layer can be analyt-

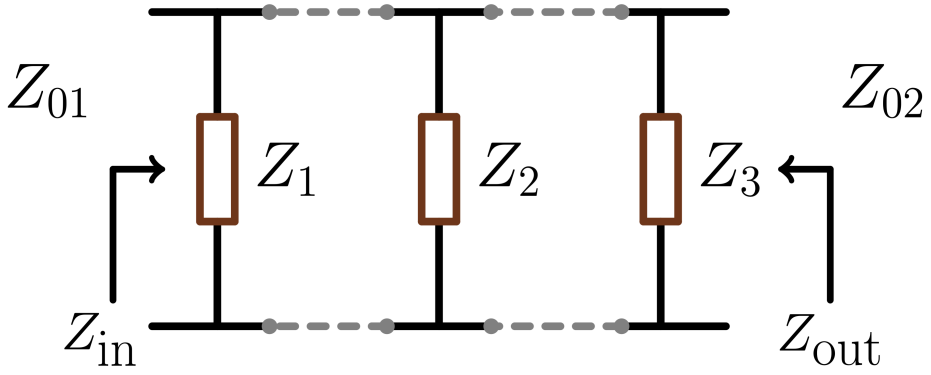

Fig. 5.3: The equivalent circuit form of the cascaded layer topology for a non-reflected metasurface. The input and output medium impedance are shown as η_1 and η_2 respectively.

ically solved as

$$Y_1 = \frac{T_{22} - N_{12}M_{21} - N_{12}M_{22}Y_2 - M_{22}N_{22}}{M_{11}N_{12} + Y_2M_{12}N_{12} + M_{12}N_{22}} \tag{5.19a}$$

$$Y_2 = \frac{T_{12} - M_{11}N_{12} - M_{12}N_{22}}{M_{12}N_{12}} \tag{5.19b}$$

$$Y_3 = \frac{T_{11} - N_{11}M_{11} - N_{11}M_{12}Y_2 - M_{12}N_{21}}{M_{11}N_{12} + Y_2M_{12}N_{12} + M_{12}N_{22}} \tag{5.19c}$$

For realizing the impedance value of each layer, several shapes of copper traces have been proposed such as dogbone [26] and spider [29]. In our case, the matching metasurface is designed for normal wave propagation from air into water without reflections where the liquid (water) is held within a container. By considering the container wall as our second "substrate", the effect of the enclosure can be incorporated into the design. Furthermore, for the simplicity of fabrication, the third admittance layer is removed (i.e., $Y_3 = 0$). The reasons of enforcing the third layer to be zero are that

- It is challenging to print copper traces on the container.
- It is challenging to realize the equivalent surface impedance in high permittivity media due to the small medium wavelength. Since the copper trace structures are designed with respect to the medium wavelength, a smaller wavelength requires a higher fabri-

cation accuracy.

- On the other hand, removing one layer will lose one degree of freedom to manipulate the electromagnetic field properties, in which it causes a constant phase shift across the metasurface. However, this is not a major issue for MWI as the data collected by receivers can be analytically calibrated by the data calibration algorithms [72].[3] Furthermore, substituting $Y_3 = 0$ into (5.19c), the constant phase shift φ can be found as

$$\varphi \;=\; \sin^{-1}\left(-\frac{M_{12}\det(N)}{\sqrt{\frac{Z_{01}}{Z_{02}}N_{12}^2 \;-\; Z_{01}Z_{02}N_{11}^2}}\right) \;-\; \tan^{-1}\left(\frac{N_{12}}{jZ_{02}N_{11}}\right) \tag{5.20}$$

  Note that there exists two possible solutions of phase shift that can make $Y_3 = 0$ and match two medium impedances. Finally, by substituting (5.20) into (5.19a) and (5.19b), the top and middle layer impedance values (i.e., Y_1 and Y_2) can be systematically calculated.

As can be seen from the above discussion, our cascaded layer topology is designed based on a single frequency of operation. The narrow bandwidth of this structure will limit us to single-frequency microwave imaging, which is not a major issue for narrow-band MWI systems. From (5.16), the required surface susceptibilities depend on the input and output medium impedances. Furthermore, the medium impedance is a function of propagation angles via $Z_{01} = \frac{\eta_1}{\cos\theta_i}$ and $Z_{02} = \frac{\eta_2}{\cos\theta_t}$. Thus, the performance of these metasurfaces has a form of angle dependency. In MWI, the directions of the fields are not known a priori due to the presence of the unknown OI. To alleviate the angle dependency issue, we have at least three approaches.

- The first one is to use angle-independent metasurfaces, which may require the metasurface to be active and nonreciprocal [93].

- The second approach is to include the metasurface model in the inversion algorithm,

[3] In MWI, the data calibration technique typically compare the measured data with those simulated in the forward solver, and then a set of calibration coefficients are formed.

e.g., by changing the Green's function shown in (3.3).

- The third approach is to use the scattered field calibration technique [72] to alleviate the effect of the angle dependency [72].

In this work, the third approach, which is using the scattered field calibration technique, is considered.

5.3 Unit Cell Design

In Sec. 5.2, it has been shown that the matching metasurface unit cells can be realized by implementing the equivalent circuit model shown in Fig. 5.3. As we remove the third impedance layer for simplicity of fabrication, this unit cell finally consists of two impedance layers and two substrates in which the second substrate is the container. Herein, the container is chosen to be plexiglass. In this section, three different unit cell topologies are proposed. The unit cells are simulated in a full-wave simulation software, ANSYS HFSS, using periodic boundary conditions and excited by Floquet ports. The excitation ports are placed sufficiently far from the unit cell (2λ in the corresponding medium at the operating frequency) so as to not include the effect of evanescent waves. Lastly, the reference plane are de-embedded [27] right on the unit cell structure to obtain the scattering parameters as shown in Fig. 5.4(a). Later in Sec. 5.4, the metasurface consisting of Unit Cell I will be used in MWI as impedance matching transformers, and synthetic imaging results will be presented to verify the performance.

5.3.1 Unit Cell I

The first example of the matching metasurface unit cell is presented in Fig. 5.4(b). This design uses impedance sheet boundaries in ANSYS HFSS. For this example, the unit cell is designed to match the medium impedance from free space ($\varepsilon_r = 1$) to the water $\varepsilon_r = 75.6 - j4$ [59] at the frequency of 1 GHz under the normally incident plane wave assumption.

Due to the fact that the loss of water (i.e., the imaginary component of the relative complex permittivity) at 1 GHz is relatively small, we assume that the water is lossless and its approximate relative permittivity is 75.6 in the design process. Note that in the unit cell simulation, the loss of the water will be taken into account.

The unit cell consists of a 6.4 mm thick Rogers RO3010 ($\varepsilon_r = 10.2$, $\tan\delta = 0.0035$), a 4.5 mm thick plexiglass ($\varepsilon_r = 3.4$, $\tan\delta = 0.001$), and two impedance sheets placed on both sides of the Rogers RO3010 substrate shown in Fig. 5.4(b)[4]. By setting $Y_3 = 0$, impedance values of the two layers and the phase shift can be analytically solved from (5.19) and (5.20), in which one set of solution is

* $Z_1 = Z_{\text{top}} = -j37.052\Omega$

* $Z_2 = Z_{\text{mid}} = -j13.472\Omega$

* $\varphi = 157.812^\circ$

Note that the subscripts "top", and "mid" are used to indicate the first, and second layers in a different fashion.

The dimensions of the unit cell are 50×50 mm ($\lambda/6$ in free space). The unit cell simulation system setup is presented in Fig. 5.4(a). As the incidence angle θ increases, the reflection coefficient ($|S_{11}|$) worsens.[5] Also note that due to the use of impedance sheet boundaries in HFSS, as opposed to actual copper traces, the angular dependency might not have been fully considered as compared to a practical copper trace implementation. The narrow frequency response and the angle dependency of this unit cell have been shown in Fig. 5.6(a)

[4]Note that in the design process, $\tan\delta$ of the substrate, which is small, has been ignored for simplicity; however, in the HFSS simulations, it has been considered.

[5]Note that this is due to the fact that the impedance value is inversely proportional to $\cos(\theta)$, which is $120\pi/(\sqrt{\varepsilon_r}\cos(\theta))$

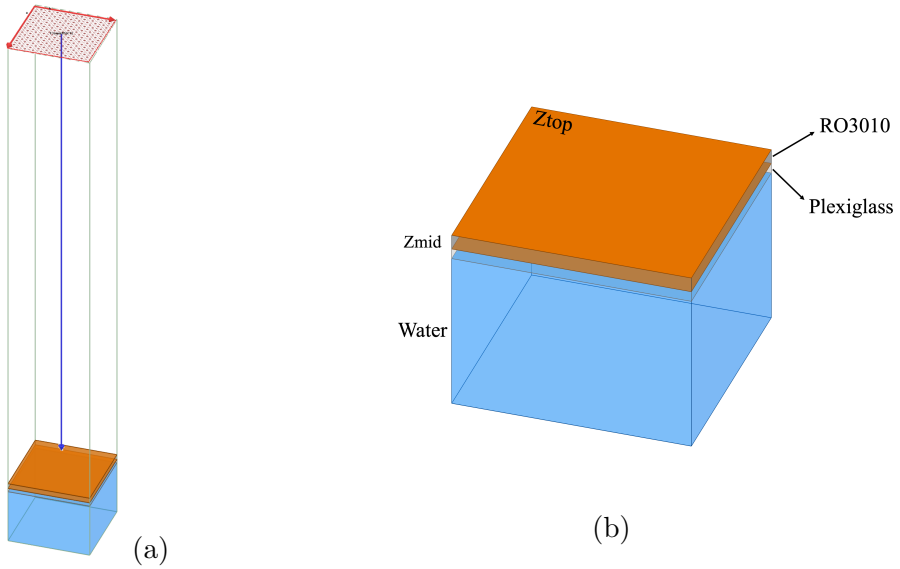

Fig. 5.4: (a) Unit cell simulation system using periodic boundary conditions and Floquet excitation ports. (b) Unit cell topology

5.3.2 Unit Cell II

The second example is a unit cell structure that is designed to match the free space ($\varepsilon_r = 1$) to deionized water ($\varepsilon_r = 78.4 - j4$) at 1 GHz [102] under the normally incident plane wave. The unit cell consists of a 15 mm thick Rogers RO3010 ($\varepsilon_r = 10.2$, $\tan\delta = 0.0035$) substrate, a 4.5 mm thick plexiglass ($\varepsilon_r = 3.4$, $\tan\delta = 0.001$), and two copper traces with 17μm thickness printed on both sides of RO3010 substrate in Ansys HFSS. The top and middle copper layers are shown in Fig. 5.5(a) and Fig. 5.5(b), respectively. Since the loss of water is small, the imaginary component of the relative complex permittivity is not considered in the design process. Following the same manner as Unit Cell I, the equivalent impedance values of the two layers can be calculated as

* $Z_{\text{top}} = -j112.284\Omega$

* $Z_{\text{mid}} = -j28.726\Omega$

Herein, the phase shift (φ) has not been specified to a desired value as it is not an issue for MWI and can be calibrated out by the utilized data calibration algorithm. The size of

	G (mm)	W (mm)	L (mm)	S (mm)
Top	21.096	38.379	34.200	33.153
Middle	39.984	40.341	44.910	39.380

Table 5.1: Dimensions of the copper traces for Unit Cell II

the unit cell is $D = 53.55$ mm ($\approx \lambda/6$ in free space). The specific dimensions of the copper traces for realizing the corresponding impedance sheet values are presented in Table 5.1 denoted by G, W, L, and S. The unit cell simulation setup follows the same manner as Unit Cell I. The $|S_{11}|$ parameter response with respect to the frequency and incidence angles are presented in Fig. 5.6(b).

5.3.3 Unit cell III

In the third example, the unit cell is designed at 10.5 GHz, and the impedance layers are realized using dogbone [26, 28] copper traces. It is also designed for the normal incidence plane wave penetrating from free space into deionized (DI) water at 10.5 GHz, in which the relative complex permittivity of DI water is $59.48 - j31.92$ at that frequency [102]. Since the water is lossy at 10.5 GHz (i.e., the relative complex permittivity has a non-negligible imaginary component) the desired T parameters are found from the desired S parameters as [68]

$$T_{11} = \frac{(Z_{01}^* + S_{11}Z_{01})(1 - S_{22}) + S_{12}S_{21}Z_{01}}{2S_{21}(R_{01}R_{02})^{1/2}} \tag{5.21a}$$

$$T_{12} = \frac{(Z_{01}^* + S_{11}Z_{01})(Z_{02}^* + S_{22}Z_{02}) - S_{12}S_{21}Z_{01}Z_{02}}{2S_{21}(R_{01}R_{02})^{1/2}} \tag{5.21b}$$

$$T_{21} = \frac{(1 - S_{11})(1 - S_{22}) - S_{12}S_{21}}{2S_{21}(R_{01}R_{02})^{1/2}} \tag{5.21c}$$

$$T_{22} = \frac{(1 - S_{11})(Z_{02}^* + S_{22}Z_{02}) + S_{12}S_{21}Z_{02}}{2S_{21}(R_{01}R_{02})^{1/2}} \tag{5.21d}$$

where the superscript $*$ denotes the complex conjugate operator, R_{01} and R_{02} are the real components of the media impedances (Z_{01} and Z_{02}), respectively. By enforcing $Y_3 = 0$ and

	G (mm)	W (mm)	L (mm)	S (mm)
Top	0.617	3.044	4.168	2.711
Middle	0.141	3.987	3.288	2.932

Table 5.2: Dimensions of dogbone copper traces for Unit Cell III

equating the desired T parameters with the those of GSTCs, the impedance values for the cascaded top and middle layers can be analytically solved as

- $Z_{\text{top}} = -j43.885\Omega$
- $Z_{\text{mid}} = -j81.135\Omega$

The simulation system setup follows the same manner as the previous cases. The size of the unit cell is 5.1 mm ($\approx \lambda/6$ in free space at 10.5 GHz) denoted by D. The unit cell consists of a 1.28 mm thick Rogers RO3010 substrate, a 4.5 mm thick plexiglass, and 17μm thick dogbone copper traces printed on both sides of the RO3010 substrate. The top and middle layers are shown in Fig. 5.5(c) and Fig. 5.5(d), respectively. The specific dimensions of the structures denoted by G, W, L, and S can be found in Table 5.2. Lastly the reflection coefficient ($|S_{11}|$) with respect to the frequency span and the incidence angles are presented in Fig. 5.6(c).

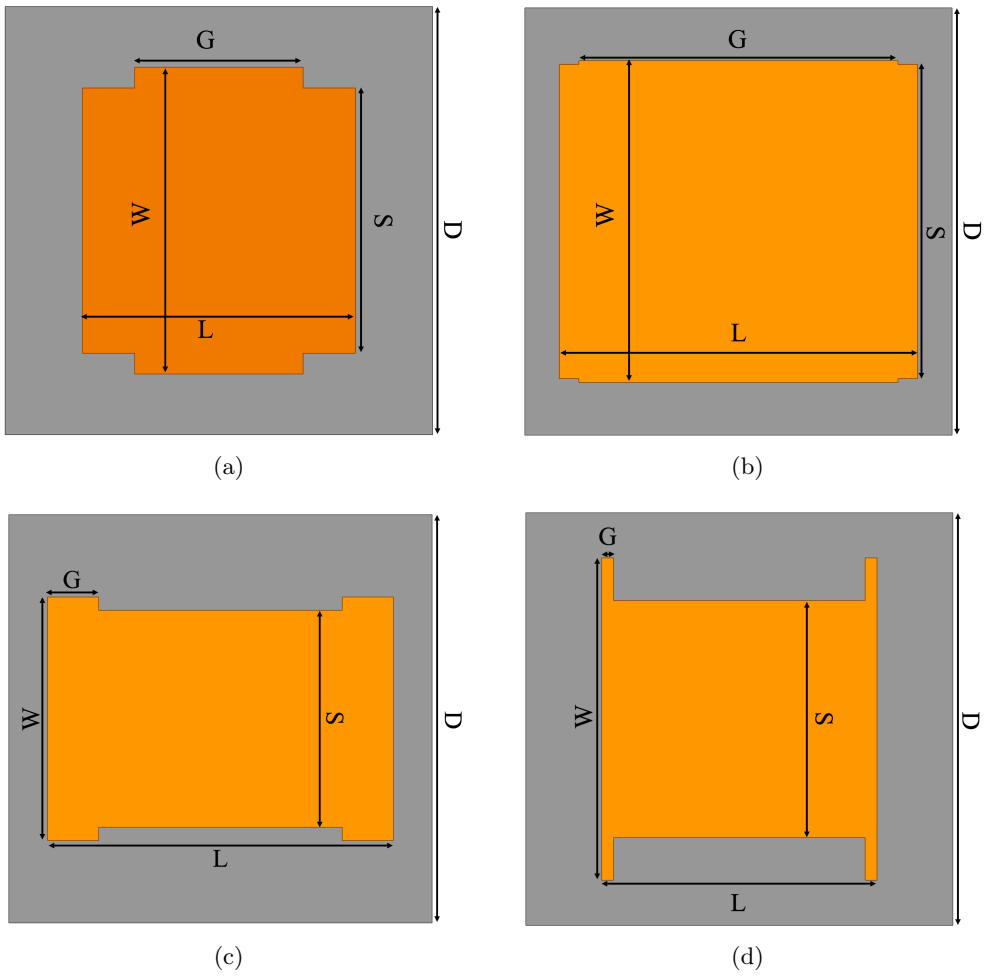

Fig. 5.5: Two different unit cell topologies for impedance matching metasurface from free space to the water at 1 GHz and 10.5 GHz. The unit cell consist of one Rogers RO3010 substrate, one 4.5 mm thick plexiglass container, and two $\frac{1}{2}$oz copper traces (17μm thickness) printed on both sides of the RO3010 substrate. The size of the unit cell is denoted by D ($\approx \lambda/6$ in free space at the operating frequency). The dimensions of the copper trace are denoted by G, W, L, and S. (Left column) top layer; (Right column) middle layer for the unit cell

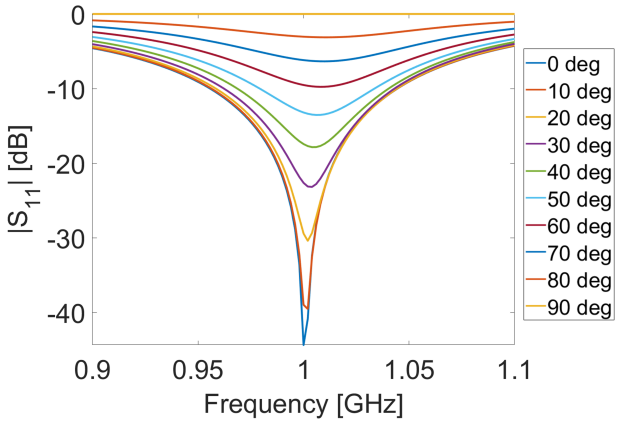

(a)

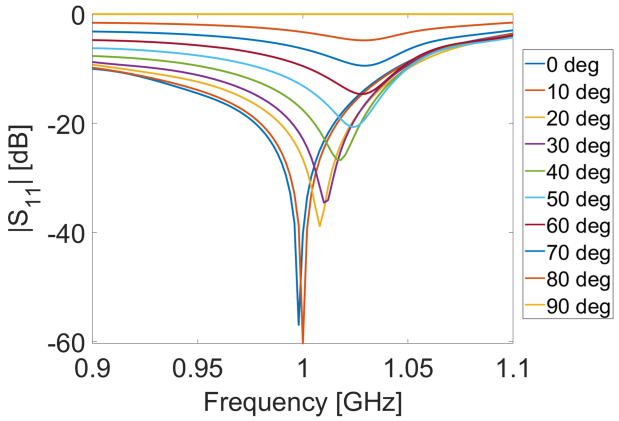

(b)

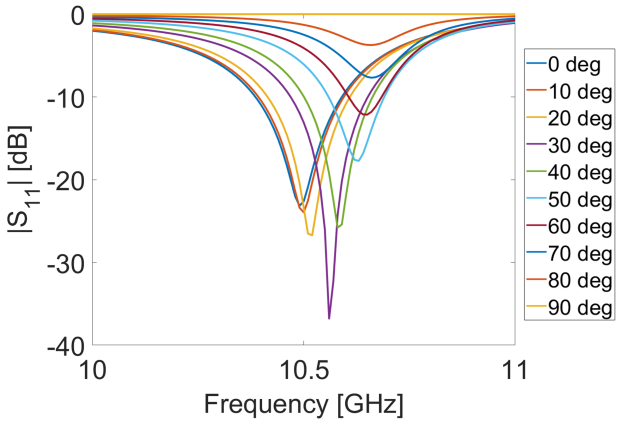

(c)

Fig. 5.6: Unit cell performance: The reflection coefficient $|S_{11}|$ with respect to the frequency span and the incidence angle scan θ from from 0 to $90°$.

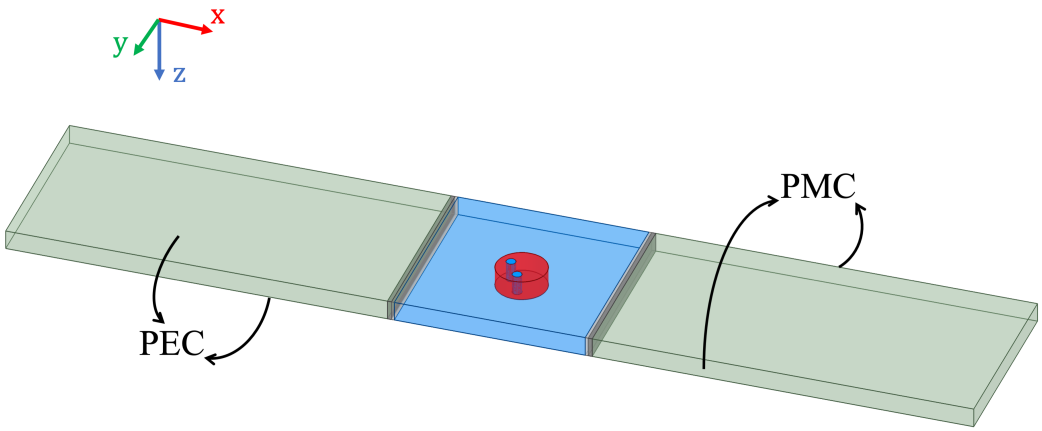

Fig. 5.7: Overview of the simulated MWI system. Two PEC planes are placed at the top and bottom of the simulation domain to create a 2D TM_z MWI setup, and two PMC planes are placed on the sides of domain. Two ends are set as wave ports in ANSYS HFSS.

5.4 Synthetic Imaging Results

Consider the simulation domain shown in Figure 5.7 where a plane wave illuminates the first matching metasurface from air, and then the scattered data are collected at the receivers located in air just outside the second metasurface (61 receivers 3.3 mm away from the second metasurface). The OI is a human forearm model. To satisfy the 2D wave propagation assumption associated with the tomographic configuration, two perfect electric conductor (PEC) planes are placed at the top and bottom of the simulation domain to mimic an infinite length along the z axis. In addition, two perfect magnetic conductor (PMC) planes are placed on the sides of the domain so that a wave port can be used to illuminate the metasurfaces with a plane wave.

The target, which has been depicted in Fig. 5.8, consists of three cylinders. The large cylinder depicted in red represents the muscle tissue with a radius of 40 mm and a relative complex permittivity of $\varepsilon_r = 20.6 - j6.5$ at 1 GHz. Two bones which are enclosed in the muscle are depicted in blue with radii of 7.5 mm and a relative complex permittivity of $\varepsilon_r = 20.6 - j6.5$ at 1 GHz. The targets are immersed in a low-loss matching fluid (water)

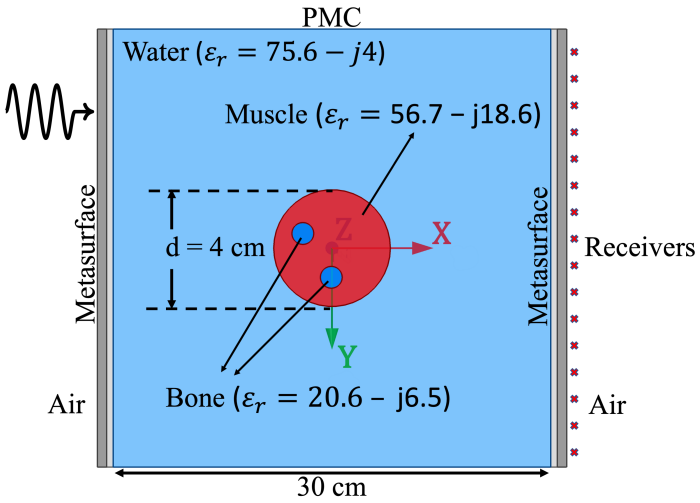

Fig. 5.8: Simulated MWI system. The matching metasurfaces are attached on the wall of the container. The OI consists of a circular muscle tissue denoted in red and two circular bones denoted in blue. The incidence is a plane wave illuminate towards $\hat{x}$ direction. The receivers are located outside of the imaging domain on a straight line orthogonal with the incidence direction along y direction.

with the relative complex permittivity of $\varepsilon_r = 75.6 - j4.0$ at 1 GHz[6].

Furthermore, the whole imaging system is contained in a plexiglass container whose dimension is 300×300 mm excluding the metasurfaces. The matching metasurfaces, which help the electromagnetic energy penetrate into the water medium and also get out from the water medium to air, are attached to the outside of the enclosure.

The utilized inversion algorithm assumes that the background medium is water that extends to infinity. However, in the MWI system presented, the receivers are located outside of the coupling liquid. As noted earlier, one way to solve this issue is to modify the inversion algorithm so that the metasurfaces can be taken into account in the inversion process. An alternative approach is to use the scattered field calibration technique [72] to compute calibration factors for each transmit-receiver pair, in which the factors take into account the transformation coefficient of the metasurface and its angle dependency. The calibration factors are formed by placing a known scatterer and comparing its scattered fields collected

[6]In previous works [52, 80], the imaginary part of the coupling liquid's relative complex permittivity needed to be about $-j15$ for successful imaging. However, high loss can decrease the desired signal levels. Therefore, the coupling fluid with an imaginary part of $-j4$ is considered to be used.

at the receivers outside of metasurface with the fields calculated from numerical model at the same location but in the coupling liquid background medium that extends to infinity. Herein, we use the scattered field calibration technique.

Since only one transmitter is used, after collecting the scattered field data E_z^{scat} at the receivers, the data are then inverted with the help of spatial prior information [100, 103] to compensate for the lack of multi-view data. (That is, the unknowns are merely three relative complex permittivity values.) In particular, we use the inversion algorithm developed in [100], which is entitled the multiplicative regularized (MR) Gauss-Newton inversion (GNI) with spatial priors (SP). This algorithm may be abbreviated as the MRSP-GNI.

The spatial priors tell the inversion algorithm about the location of different permittivity values. In other words, the inversion algorithm knows about the shape and location but has no idea about the permittivity values and then processes the scattered field data to yield quantitative relative complex permittivity values for each region within the imaging domain. In this example, the imaging domain is a 5×5 cm^2 domain discretized into 50×50 square cells. To alleviate the angle dependency issue of the metasurface, we have relied on the loss within the imaging domain as well as the scattered field calibration technique [72]. The calibration object was a circular cylinder with the diameter of 6 cm and a relative complex permittivity of $\varepsilon_r = 23.4 - j20.3$ placed at the origin and immersed in water. For the calibration target, the scattered field data collected in HFSS (red) and that collected by the numerical model (blue), which assumes an infinite water background, are shown in Figure 5.9.

The calibration vector is a complex vector of length 61, which is formed by point-by-point matching of these two curves. The calibration vector is then applied to the vector of scattered field data collected from the OI via element-wise vector multiplication. The inversion results can be found in Figure 5.10(a)-(b). We also noticed that if we truncate the inversion algorithm before its full convergence, a more accurate reconstructed (real-part)

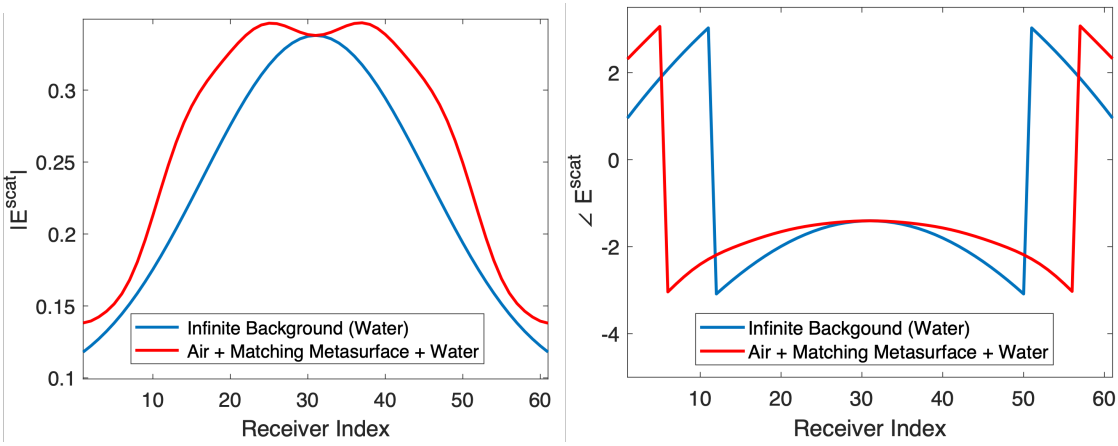

(a) magnitude (b) phase

Fig. 5.9: The scattered field calibration process: comparing the scattered field from a known target within the system (red) with the scattered field due to the same known target within the numerical model (blue). The blue and red curves are then matched using calibration coefficients. The same calibration coefficients are then used for the data collected from the unknown object of interest (OI).

permittivity value for bones can be obtained as shown in Figure 5.10(c)-(d).

Finally, we note that this example has been chosen to demonstrate this possibility; however, we have also observed other examples where the calibration process, and thus the inversion process, fail. That is, the above procedure is currently dependent on the OI and the calibration object. To alleviate this, in future work, the presence of the metasurfaces should be included within the inversion algorithm (i.e., in the forward and inverse solvers).

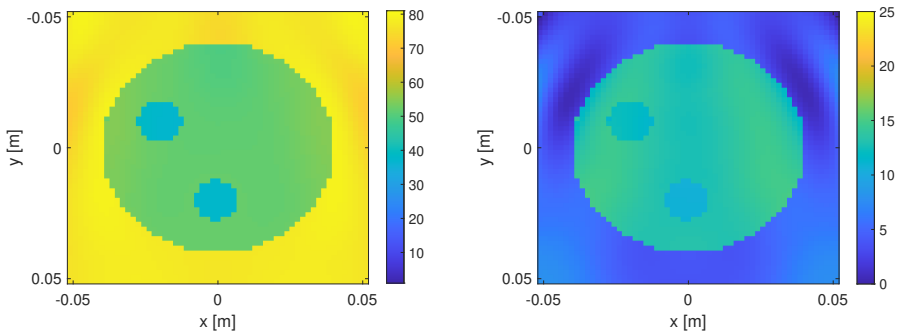

(a) $\mathrm{Re}(\varepsilon_r)$ (b) $-\mathrm{Im}(\varepsilon_r)$

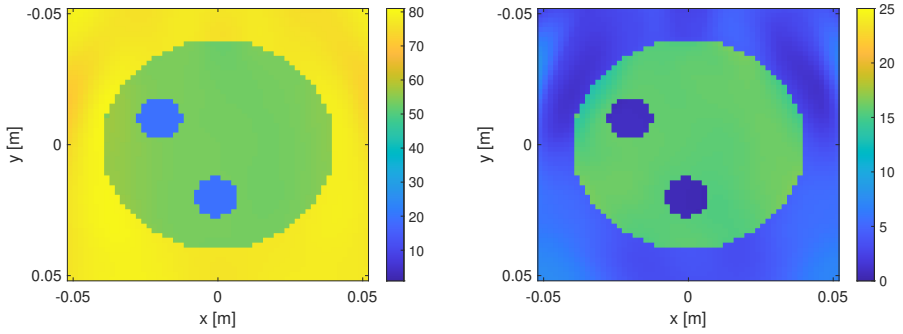

(c) $\mathrm{Re}(\varepsilon_r)$ (d) $-\mathrm{Im}(\varepsilon_r)$

Fig. 5.10: Reconstruction with spatial priors (a)-(b) after full convergence; and (c)-(d) for early truncation.

5.5 Experimental Results

A matching metasurface has been fabricated and measured. The details of this experimental evaluation are now presented.

5.5.1 Fabrication

A matching metasurface consisting of Unit Cell III, described in Sec. 5.3.3, is fabricated. This metasurface consists of a 1.28 mm thick Rogers R03010 substrate with the dimension of 22.85×30.5 cm^2 attached on a $30.47 \times 38.12 \times 3$ cm plexiglass container as shown in Fig. 5.11. A total number of 2200 unit cells (40×55) having dogbone copper traces of 17μm thickness are printed on each side of the substrate respectively. The dogbone dimensions

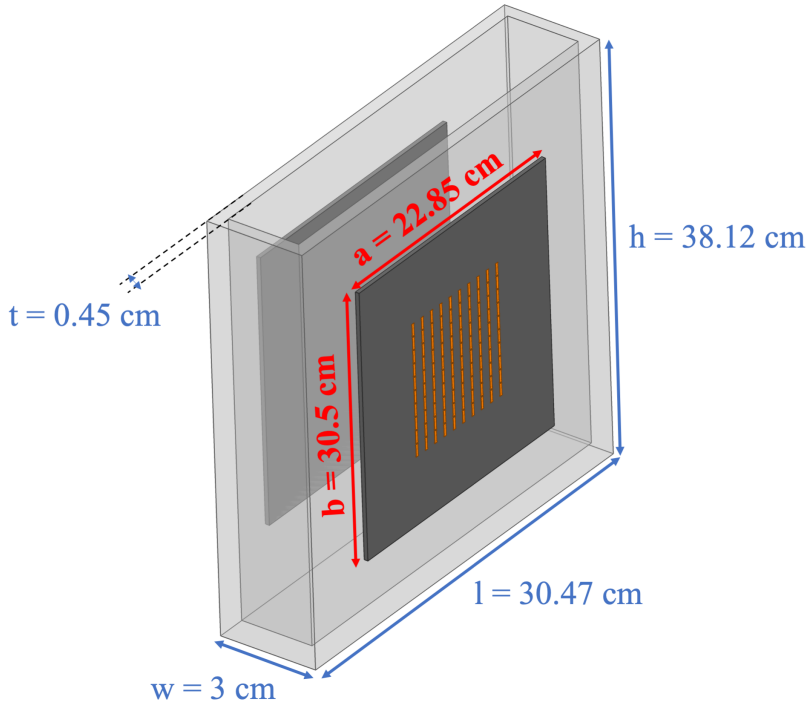

Fig. 5.11: Dimension of the plexiglass container and the metasurface attached to it.

are consistent with the dimensions of Unit Cell III listed in Table 5.2. In addition, for ease of handling, 0.5 inch empty space has been left from the printed circuit board (PCB) outline.

To experimentally evaluate the transmission of electromagnetic energy through the system, we first measured S_{21} with two horn antennas normally facing both sides of the container with the presence of two matching metasurfaces. DI water was filled in the container, and the designed operating frequency is set to 10.5 GHz. The separation between the horn antennas and the container was initially set to 66 mm, and the power illuminated from the horn antenna was 0 dBm. Since the DI water is very lossy at 10.5 GHz, with a relative complex permittivity of $59.48 - j31.92$ [102], the received signal by the second horn antenna was buried in the noise level. To understand this, let us assume a plane wave propagation in the DI water. The length that the plane wave travel in the DI water is

$(3 - 2 \times 0.45)$ cm. In addition, the complex wavenumber in the DI water is

$$k = \frac{\omega}{c_0/\sqrt{\epsilon_r}} = \frac{2\pi \times 10.5 \times 10^9 \times \sqrt{59.48 - j31.92}}{3 \times 10^8} = 1.7523 \times 10^3 - j4.4048 \times 10^2 \quad (5.22)$$

Therefore, the attenuation of the field within the DI water will be

$$\text{Field attenuation} = e^{-4.4048\times10^2\times\text{length}_{\text{DI}}} = e^{-4.4048\times10^2\times(3-2\times0.45)\times10^{-2}} = 9.6113 \times 10^{-5} \quad (5.23)$$

Thus, the power attenuates as $(9.6113 \times 10^{-5})^2$ which is about -80.34 dB. In other words, most of the energy was dissipated in the DI water and the system can be considered as a microwave absorber at 10.5 GHz. The measurement was also repeated with a separation distance of 33 cm from horn antennas to the container. However, the received signal did not improve.

We then needed to verify our assumption that the reason for not receiving signal is due to power dissipation in the lossy DI. In other words, we needed to verify that most of the power has already penetrated into the water. To this end, we focused on investigating the reflection coefficient S_{11} of the metasurface. Naturally if $|S_{11}|$ is small, we can then conclude that the metasurface has acted properly, and have efficiently transferred the electromagnetic energy from air to the DI water.

To measure the reflection parameter S_{11}, the horn antenna is placed 70 cm away from the metasurface. The distance from the coaxial port of the horn antenna to the horn aperture is 13 cm. Thus, the distance from the port of the horn antenna to the metasurface is 83 cm (13cm + 70cm). The length of the cable from the vector network analyzer (VNA) to the excitation port of the horn antenna has already been calibrated out. Therefore, in the time-domain feature of the VNA, the reflection from the metasurface is expected to occur at around 5.53 nsec based on the following equation

$$t = \frac{d_{\text{round-trip}}}{c_0} = \frac{2 \times (13 \text{ cm} + 70 \text{ cm})}{c_0} \quad (5.24)$$

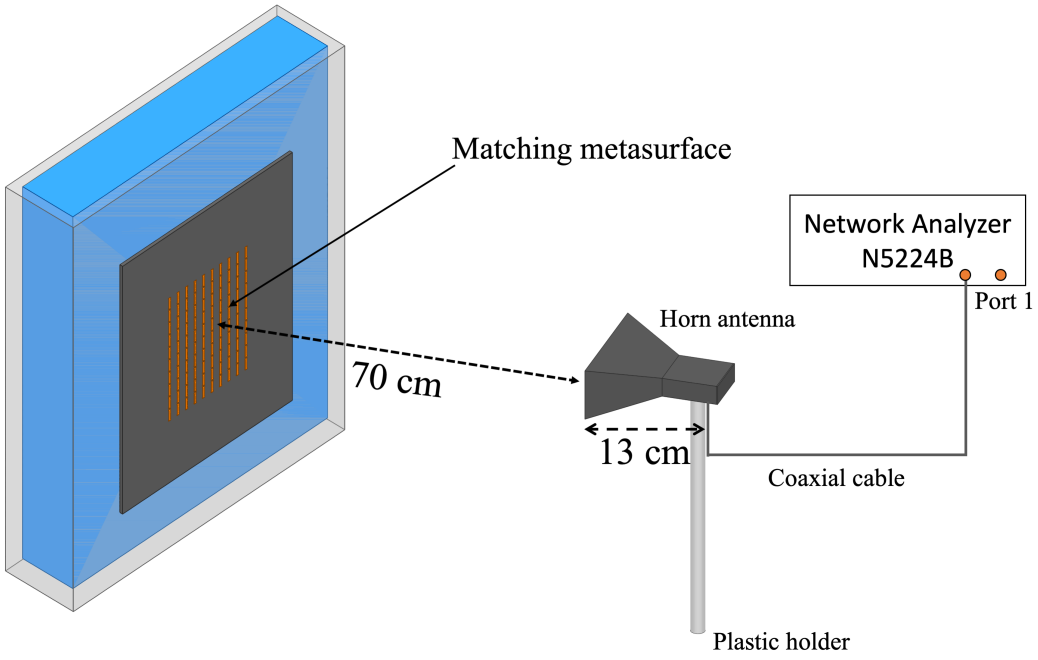

Fig. 5.12: The measurement setup. A horn antenna is used to irradiate the metasurface. A vector network analyzer, using its time-domain option (time gating), records the reflected signal from the metasurface for the normal incidence.

Consequently, the time gating for the S_{11} VNA measurement was set from 4 nsec to 10 nsec to cover the reflection caused by the matesurface.

5.5.2 Measurements

The schematic of the measurement setup is presented in Fig. 5.12 where a horn antenna is used to irradiate the metasurface. (The horn antenna is visually placed such that its incident plane wave is normal to the metasurface.) The distance between the horn aperture to the metasurface is 70 cm.[7] The horn is fed through Port 1 of a VNA which in our case is a Keysight PNA Network Analyzer N5224B. One-port calibration was performed to have the reference plane at the feeding point of the horn antenna. The VNA was setup to measure from 8 GHz to 12 GHz with 6401 points, 0 dBm power level, and an IF bandwidth

[7] At the frequency of 10.5 GHz, this distance in terms of wavelength is about 24.5λ where λ denoted the wavelength in free space at the operating frequency. We consider this to be within the far-field zone, and thus the incident field can be assumed to be a plane wave.

of 10 KHz.

The VNA initially measured the response in the frequency domain, in which various sources of reflections are mixed with the reflection of interest. These undesired reflections could be for example the reflections from the wall, VNA's desk, transition from the WR90 waveguide feed to the horn aperture, human body of the operator, etc. The time-domain feature of the VNA was then used to consider the reflection of interest (i.e., the reflection emanating from the metasurface) and filter out the undesired signals [96].

Turning on the time-domain option of the VNA, we noticed a reflected signal greater than -60 dB at around 5.46 nsec as shown in Fig. 5.13. Note that this is close to our expected arrival time (5.53 nsec) based on (5.24). Thus, this reflection is considered as the reflection emanating from the metasurface. The time gating was then set from 4 nsec to 10 nsec with the following specifications[8]: *Normal Gate Shape* and *Band Pass Gate Type*. The reflection signal of the matching metasurface case is presented in Fig. 5.13(a) by the black curve. The system setup, with the metasurface present, is also presented in Fig. 5.14(a).

To be able to evaluate the performance of the metasurface, the reflections due to the presence of the metasurface are compared with two more cases: when the metasurface is replaced with a metallic layer (copper tape) and when the metasurface is removed, and we do not replace it with any other materials. The experiment with a metallic layer is important as it represents our reference for the total (100%) reflection. The measured time-domain signal when the copper tape is installed instead of the metasurface is shown by the red curve in Fig. 5.13(a). The experimental system when measuring the reflected signal

[8]The received signal after time gating can be thought as

$$r(t) \;=\; x(t) \;\cdot\; \mathrm{rect}(\frac{t \;-\; t_0}{T})$$

where $x(t)$ is the actual signal in the time domain, 'rect' is the rectangular function controlling the time gating, and $r(t)$ is the reflected signal after the application of time gating. Consequently, the above relation in the frequency domain will be

$$R(\omega) \;=\; X(\omega) \;*\; \frac{T}{2\pi} e^{-j\omega t_0} \mathrm{sinc}(\frac{\omega T}{2})$$

where $*$ denotes the convolution operator.

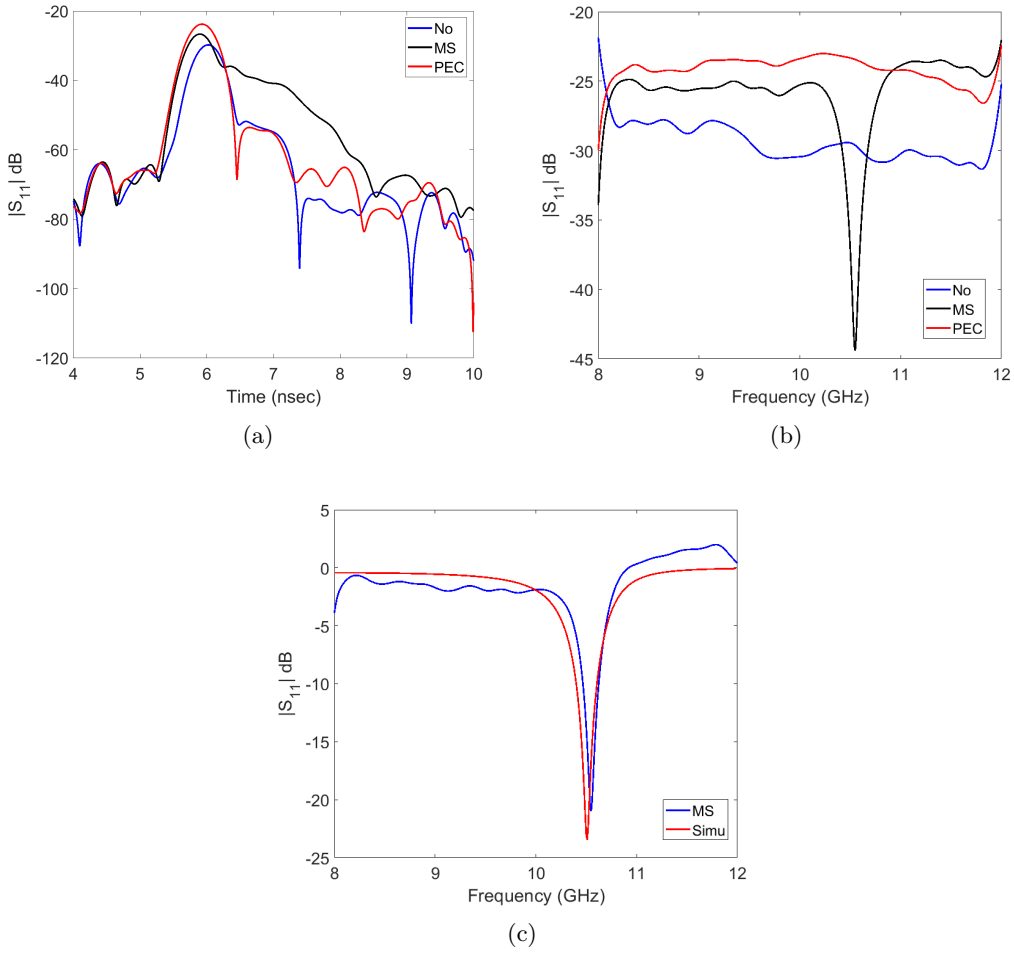

Fig. 5.13: (a) The reflection as a function of time collected by the time-domain feature of the VNA for the matching metasurface, copper tape, and no metasurface cases within the chosen time gating interval. (b) The reflection as a function of frequency collected for these three cases as the time gating is on. (c) The calibrated measured reflection from the matching metasurface compared with its corresponding simulated data in ANSYS HFSS.

from the copper tape is also shown in Fig. 5.14(b).

Lastly, we obtain the time-domain reflected signal in the absence of the metasurface. That is, the metasurface was removed from the container; this is referred to as "no metasurface". The reflected signal for this case has been shown in Fig. 5.13(a) by the blue curve. Also, Fig. 5.14(c) shows the physical setup of the measurement.

By comparing the three time-domain curves in Fig. 5.13(a), the following two items can

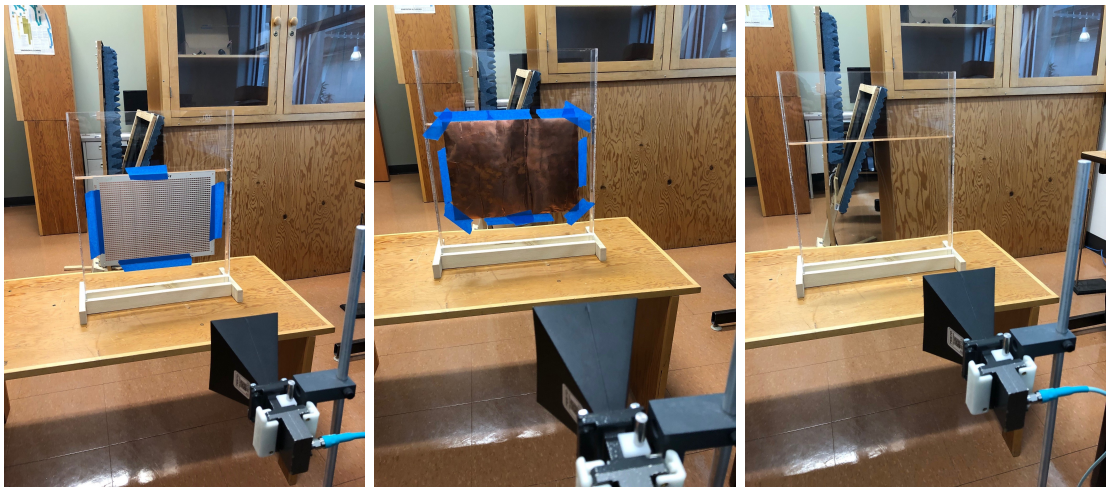

(a) (b) (c)

Fig. 5.14: Horn antenna irradiating (a) the metasurface (b) the copper tape placed in front of the metasurface and (c) container without metasurface. In the last case, the metasurface has been removed from the container.

be noted:

- The time-domain curves representing the 'no metasurface' and the metallic layer cases are relatively similar. This is expected as the interface of air-plexiglass-water is expected to have a significant reflection, similar to the 100% reflection expected from the metallic layer. (The magnitude of the Fresnel reflection coefficient at the air-DI water interface is 78.9%.)

- The time-domain curve representing the metasurface case is wider as compared to the other two cases. This is an indication that in the frequency domain, the curve would be sharper. This can be regarded as the possibility of a resonance-type behavior in the frequency domain response when the metasurface is used.

Lastly, to compare the experimental performance of the metasurface with the simulated data, we need to calibrate our measured data based on the reference reflection associated with the metallic surface. This is based on knowing that the reflection coefficient from a perfect electric conductor (PEC) must be 100% or 0 dB. Thus, the additive calibration

numbers (in dB) at each point are obtained to convert reflected signal from the metallic layer (in the frequency domain), shown in red in Figure 5.13 to a flat 0 dB line. The same calibration numbers are then applied to the curve associated with the reflections from the metasurface as a function of frequency shown in Fig. 5.13(b) in black. The calibrated measured data from the metasurface is shown in blue in Figure 5.13(c) in which the signal varies from about 0 dB to -20.86 dB. (Note that the calibrated measured data goes above 0 dB which is obviously wrong due to the passive nature of the system. This is due to the non-ideal form of the calibration process.) The simulated reflection signal of the metasurface using ANSYS HFSS is presented in Fig. 5.13(c) red curve. As the plot shown, the simulated data has a similar trend with the measured data. Only the resonance frequency has a little shift from 10.51 GHz to 10.55 GHz.

Chapter 6

Conclusions and Future Work

6.1 Conclusions

In conclusion, this thesis aims to investigate the use of metasurfaces in MWI applications. To achieve this goal, we first summarized the boundary conditions of metasurfaces, which are known as generalized sheet transition conditions (GSTCs). In particular, the GSTCs were expressed in terms of the surface polarizability model, surface susceptibility model, and surface impedance model. We then focused our attention on the GSTCs that would be relevant to the 2D microwave imaging (MWI), which is typically known as the TM_z microwave imaging. We further restricted ourselves to reciprocal metasurfaces for the ease of implementation, and also considered the bi-anisotropic metasurfaces for the increased degree of design freedom.

We then considered two applications of metasurface in MWI: (i) absorbing metasurfaces used as the casing of the system, and (ii) matching metasurfaces used as impedance transformers.

- **Absorbing metasurfaces for MWI:** In MWI, *lossy* matching fluids are typically used to mitigate the reflections occurring at the enclosure. The main problem of this approach is that the desired signal is also attenuated. The metallic-backed absorbing

metasurfaces were investigated as the casing of MWI systems. In particular, three topologies of absorbing metasurfaces were considered. Using simulated data in Ansys HFSS, it was shown that metallic-backed absorbing metasurfaces can be used to shield the system and also reduce the reflections at the enclosure. An absorbing metasurface was fabricated and the reflectivity was experimentally tested for the normal incidence. The preliminary result is promising. However, the metasurfaces are still needed to be tested in a real imaging chamber to verify their imaging performance.

- **Matching metasurfaces for MWI:** MWI systems typically rely on matching fluids to couple microwave energy into the OI. One of the challenges with the use of matching fluids is that they need to be changed on a regular basis. To alleviate the necessity of having matching fluids, the use of matching metasurfaces was investigated as impedance transformers in MWI. Similar to the absorbing metasurfaces, the main disadvantage of this approach is the angular dependency of metasurfaces. To alleviate this, the scattered field calibration technique was used in an attempt to reduce this effect. Furthermore, spatial priors were employed to compensate for the lack of multi-view data. By properly setting up the MWI system with the proposed metasurfaces in Ansys HFSS, the simulated scattered field data were collected and processed by the inversion algorithm. The imaging result with the use of spatial priors was reasonable when illuminating a high dielectric value target directly from air (using the matching metasurface). Lastly, a matching metasurface was fabricated and measured to evaluate its performance for the normal incidence. This showed reasonable matching performance in a narrow frequency band.

6.2 Future Work

Several improvements can be investigated in the future. The future work can be categorized into (i) metasurface synthesis, (ii) metasurface design, and (iii) other MWI applications.

- **Metasurface Synthesis:** The GSTCs considered in Chapter 2 ignore the normal susceptibilities (normal to the surface) for simplicity. In addition, the considered GSTCs are of first order. However, by incorporating the normal susceptibilities, more complicated design scenarios may be realized [88]. In addition, by representing the metasurface discontinuity with higher order terms, the field transformation may be better controlled [104]. Thus, in the future, these can be investigated for MWI applications.

- **Metasurface Design:** A passive and reciprocal metasurface cannot provide full control of field transformation. To provide further field control in the future work, active metasurfaces can be investigated. For example, a software controlled intelligent metasurface [105, 106] and space-time metasurfaces [107, 108] can be investigated in the context of MWI applications. For example, by using such techniques, we may achieve an angle-independent metasurface to be used in MWI.

- **Other MWI applications:** Metasurfaces can be used in MWI applications to tailor the transmit and receive patterns of the antennas, e.g., to create focused beams [76]. These can be further investigated in conjunction with matching metasurfaces such that a single metasurface system provides both matching and focusing capabilities, e.g., see [98].

Bibliography

[1] C. Pfeiffer and A. Grbic, "Metamaterial Huygens surfaces: tailoring wave fronts with reflectionless sheets," *Physical review letters*, vol. 110, no. 19, p. 197401, 2013.

[2] C. L. Holloway, E. F. Kuester, J. A. Gordon, J. O'Hara, J. Booth, and D. R. Smith, "An overview of the theory and applications of metasurfaces: The two-dimensional equivalents of metamaterials," *IEEE Antennas and Propagation Magazine*, vol. 54, no. 2, pp. 10–35, 2012.

[3] M. Selvanayagam and G. V. Eleftheriades, "Discontinuous electromagnetic fields using orthogonal electric and magnetic currents for wavefront manipulation," *Optics express*, vol. 21, no. 12, pp. 14 409–14 429, 2013.

[4] K. Achouri and C. Caloz, *Electromagnetic Metasurfaces: Theory and Applications*. John Wiley & Sons, 2021.

[5] T. Brown, C. Narendra, Y. Vahabzadeh, C. Caloz, and P. Mojabi, "On the use of electromagnetic inversion for metasurface design," *IEEE Transactions on Antennas and Propagation*, vol. 68, no. 3, pp. 1812–1824, 2020.

[6] V. G. Ataloglou, A. H. Dorrah, and G. V. Eleftheriades, "Design of compact Huygens metasurface pairs with multiple reflections for arbitrary wave transformations," *IEEE Transactions on Antennas and Propagation*, vol. 68, no. 11, pp. 7382–7394, 2020.

[7] C. Pfeiffer and A. Grbic, "Bianisotropic metasurfaces for optimal polarization control: Analysis and synthesis," *Physical Review Applied*, vol. 2, no. 4, p. 044011, 2014.

[8] K. Achouri and O. J. Martin, "Fundamental Properties and Classification of Polarization Converting Bianisotropic Metasurfaces," *IEEE Transactions on Antennas and Propagation*, 2021.

[9] Y. Ra'di, V. S. Asadchy, and S. A. Tretyakov, "Tailoring reflections from thin composite metamirrors," *IEEE Transactions on Antennas and Propagation*, vol. 62, no. 7, pp. 3749–3760, 2014.

[10] Y. Ra'di, C. Simovski, and S. Tretyakov, "Thin perfect absorbers for electromagnetic waves: theory, design, and realizations," *Physical Review Applied*, vol. 3, no. 3, p. 037001, 2015.

[11] T. Niemi, A. O. Karilainen, and S. A. Tretyakov, "Synthesis of polarization transformers," *IEEE Transactions on Antennas and Propagation*, vol. 61, no. 6, pp. 3102–3111, 2013.

[12] Y. Ra'di and S. A. Tretyakov, "Balanced and optimal bianisotropic particles: maximizing power extracted from electromagnetic fields," *New Journal of Physics*, vol. 15, no. 5, p. 053008, 2013.

[13] T. Brown, Z. Liu, and P. Mojabi, "Full-wave verification of an electromagnetic inversion metasurface design method," in *2020 IEEE International Symposium on Antennas and Propagation and North American Radio Science Meeting*, 2020, pp. 971–972.

[14] M. M. Idemen, *Discontinuities in the electromagnetic field*. John Wiley & Sons, 2011, vol. 40.

[15] E. F. Kuester, M. A. Mohamed, M. Piket-May, and C. L. Holloway, "Averaged transition conditions for electromagnetic fields at a metafilm," *IEEE Transactions on Antennas and Propagation*, vol. 51, no. 10, pp. 2641–2651, 2003.

[16] K. Achouri, M. A. Salem, and C. Caloz, "General metasurface synthesis based on susceptibility tensors," *IEEE Transactions on Antennas and Propagation*, vol. 63, no. 7, pp. 2977–2991, 2015.

[17] M. Albooyeh, S. Tretyakov, and C. Simovski, "Electromagnetic characterization of bianisotropic metasurfaces on refractive substrates: General theoretical framework," *Annalen der Physik*, vol. 528, no. 9-10, pp. 721–737, 2016.

[18] X. Jia, Y. Vahabzadeh, C. Caloz, and F. Yang, "Synthesis of spherical metasurfaces based on susceptibility tensor GSTCs," *IEEE Transactions on Antennas and Propagation*, vol. 67, no. 4, pp. 2542–2554, 2019.

[19] V. S. Asadchy, A. Díaz-Rubio, and S. A. Tretyakov, "Bianisotropic metasurfaces: physics and applications," *Nanophotonics*, vol. 7, no. 6, pp. 1069–1094, 2018.

[20] V. S. Asadchy, I. A. Faniayeu, Y. RaDi, S. Khakhomov, I. Semchenko, and S. Tretyakov, "Broadband reflectionless metasheets: frequency-selective transmission and perfect absorption," *Physical Review X*, vol. 5, no. 3, p. 031005, 2015.

[21] C. L. Holloway, A. Dienstfrey, E. F. Kuester, J. F. OHara, A. K. Azad, and A. J. Taylor, "A discussion on the interpretation and characterization of metafilms/metasurfaces: The two-dimensional equivalent of metamaterials," *Metamaterials*, vol. 3, no. 2, pp. 100–112, 2009.

[22] A. Epstein and G. V. Eleftheriades, "Passive lossless Huygens metasurfaces for conversion of arbitrary source field to directive radiation," *IEEE Transactions on Antennas and Propagation*, vol. 62, no. 11, pp. 5680–5695, 2014.

[23] T. Brown, C. Narendra, C. Niu, and P. Mojabi, "On the use of electromagnetic inversion for near-field antenna measurements: A review," in *2018 IEEE Conference on Antenna Measurements & Applications (CAMA)*, 2018, pp. 1–4.

[24] G. Lavigne, K. Achouri, V. S. Asadchy, S. A. Tretyakov, and C. Caloz, "Susceptibility derivation and experimental demonstration of refracting metasurfaces without spurious diffraction," *IEEE Transactions on Antennas and Propagation*, vol. 66, no. 3, pp. 1321–1330, 2018.

[25] A. H. Dorrah, M. Chen, and G. V. Eleftheriades, "Bianisotropic Huygens metasurface for wideband impedance matching between two dielectric media," *IEEE Transactions on Antennas and Propagation*, vol. 66, no. 9, pp. 4729–4742, 2018.

[26] A. Epstein and G. V. Eleftheriades, "Arbitrary power-conserving field transformations with passive lossless omega-type bianisotropic metasurfaces," *IEEE Transactions on Antennas and Propagation*, vol. 64, no. 9, pp. 3880–3895, 2016.

[27] M. Chen, E. Abdo-Sánchez, A. Epstein, and G. V. Eleftheriades, "Theory, design, and experimental verification of a reflectionless bianisotropic Huygens' metasurface for wide-angle refraction," *Physical Review B*, vol. 97, no. 12, p. 125433, 2018.

[28] G. Xu, S. V. Hum, and G. V. Eleftheriades, "Augmented Huygens metasurfaces employing baffles for precise control of wave transformations," *IEEE Transactions on Antennas and Propagation*, vol. 67, no. 11, pp. 6935–6946, 2019.

[29] A. Epstein and G. V. Eleftheriades, "Huygens metasurfaces via the equivalence principle: design and applications," *JOSA B*, vol. 33, no. 2, pp. A31–A50, 2016.

[30] B. O. Raeker and A. Grbic, "Compound metaoptics for amplitude and phase control of wave fronts," *Physical Review Letters*, vol. 122, no. 11, p. 113901, 2019.

[31] T. Brown and P. Mojabi, "Cascaded metasurface design using electromagnetic inversion with gradient-based optimization," *TechRxiv. preprint Techrxiv.12743663.v1*, 2020.

[32] A. M. Wong and G. V. Eleftheriades, "Perfect anomalous reflection with a bipartite Huygens metasurface," *Physical Review X*, vol. 8, no. 1, p. 011036, 2018.

[33] X. Liu, K. Fan, I. V. Shadrivov, and W. J. Padilla, "Experimental realization of a terahertz all-dielectric metasurface absorber," *Optics express*, vol. 25, no. 1, pp. 191–201, 2017.

[34] X. Wang, A. Díaz-Rubio, V. S. Asadchy, G. Ptitcyn, A. A. Generalov, J. Ala-Laurinaho, and S. A. Tretyakov, "Extreme asymmetry in metasurfaces via evanescent fields engineering: Angular-asymmetric absorption," *Physical Review Letters*, vol. 121, no. 25, p. 256802, 2018.

[35] G. Perrakis, O. Tsilipakos, G. Kenanakis, M. Kafesaki, C. M. Soukoulis, and E. N. Economou, "Perfect optical absorption with nanostructured metal films: design and experimental demonstration," *Optics express*, vol. 27, no. 5, pp. 6842–6850, 2019.

[36] G. Xu, G. V. Eleftheriades, and S. V. Hum, "Discrete-fourier-transform-based framework for analysis and synthesis of cylindrical omega-bianisotropic metasurfaces," *Physical Review Applied*, vol. 14, no. 6, p. 064055, 2020.

[37] N. M. Estakhri and A. Alù, "Ultra-thin unidirectional carpet cloak and wavefront reconstruction with graded metasurfaces," *IEEE Antennas and Wireless Propagation Letters*, vol. 13, pp. 1775–1778, 2014.

[38] Y. Yang, L. Jing, B. Zheng, R. Hao, W. Yin, E. Li, C. M. Soukoulis, and H. Chen, "Full-polarization 3D metasurface cloak with preserved amplitude and phase," *Advanced Materials*, vol. 28, no. 32, pp. 6866–6871, 2016.

[39] C. Huang, J. Yang, X. Wu, J. Song, M. Pu, C. Wang, and X. Luo, "Reconfigurable metasurface cloak for dynamical electromagnetic illusions," *Acs Photonics*, vol. 5, no. 5, pp. 1718–1725, 2017.

[40] J. Park, J.-H. Kang, S. J. Kim, X. Liu, and M. L. Brongersma, "Dynamic reflection phase and polarization control in metasurfaces," *Nano letters*, vol. 17, no. 1, pp. 407–413, 2017.

[41] G. Minatti, F. Caminita, E. Martini, M. Sabbadini, and S. Maci, "Synthesis of modulated-metasurface antennas with amplitude, phase, and polarization control," *IEEE Transactions on antennas and propagation*, vol. 64, no. 9, pp. 3907–3919, 2016.

[42] P. M. Meaney, M. W. Fanning, T. Raynolds, C. J. Fox, Q. Fang, C. A. Kogel, S. P. Poplack, and K. D. Paulsen, "Initial clinical experience with microwave breast imaging in women with normal mammography," *Academic radiology*, vol. 14, no. 2, pp. 207–218, 2007.

[43] N. K. Nikolova, *Introduction to Microwave Imaging*. United Kingdom: Cambridge University Press, 2017.

[44] M. Pastorino, *Microwave Imaging*. New Jersey: John Wiley & Sons, 2010.

[45] E. C. Fear, S. C. Hagness, P. M. Meaney, M. Okoniewski, and M. A. Stuchly, "Enhancing breast tumor detection with near-field imaging," *IEEE Microwave magazine*, vol. 3, no. 1, pp. 48–56, 2002.

[46] R. Palmeri, M. T. Bevacqua, L. Crocco, T. Isernia, and L. D. Donato, "Microwave imaging via distorted iterated virtual experiments," *IEEE Transactions on Antennas and Propagation*, vol. 65, no. 2, pp. 829–838, Feb 2017.

[47] C. Gilmore, P. Mojabi, A. Zakaria, M. Ostadrahimi, C. Kaye, S. Noghanian, L. Shafai, S. Pistorius, and J. LoVetri, "A wideband microwave tomography system with a novel frequency selection procedure," *IEEE Transactions on Biomedical Engineering*, vol. 57, no. 4, pp. 894–904, April 2010.

[48] A. Abubakar, T. M. Habashy, G. Pan, and M. K. Li, "Application of the multiplicative regularized Gauss Newton algorithm for three-dimensional microwave imaging," *IEEE Transactions on Antennas and Propagation*, vol. 60, no. 5, pp. 2431–2441, May 2012.

[49] P. Mojabi and J. LoVetri, "Microwave biomedical imaging using the multiplicative regularized Gauss–Newton inversion," *IEEE Antennas and Wireless Propagation Letters*, vol. 8, pp. 645–648, 2009.

[50] A. Abubakar, P. M. Van den Berg, and J. J. Mallorqui, "Imaging of biomedical data using a multiplicative regularized contrast source inversion method," *IEEE Transactions on Microwave Theory and Techniques*, vol. 50, no. 7, pp. 1761–1771, 2002.

[51] P. Mojabi and J. LoVetri, "Overview and classification of some regularization techniques for the Gauss-Newton inversion method applied to inverse scattering problems," *IEEE Transactions on Antennas and Propagation*, vol. 57, no. 9, pp. 2658–2665, Sept 2009.

[52] M. Ostadrahimi, P. Mojabi, A. Zakaria, J. LoVetri, and L. Shafai, "Enhancement of Gauss-Newton inversion method for biological tissue imaging," *IEEE Transactions on Microwave Theory and Techniques*, vol. 61, no. 9, pp. 3424–3434, Sept 2013.

[53] A. Abubakar, P. M. van den Berg, and T. M. Habashy, "Application of the multiplicative regularized contrast source inversion method on TM-and TE-polarized experimental fresnel data," *Inverse Problems*, vol. 21, no. 6, p. S5, 2005.

[54] F. S. Cuesta, I. A. Faniayeu, V. S. Asadchy, and S. A. Tretyakov, "Planar broadband Huygens metasurfaces for wave manipulations," *IEEE Transactions on Antennas and Propagation*, vol. 66, no. 12, pp. 7117–7127, 2018.

[55] S. A. Tretyakov, F. Mariotte, C. R. Simovski, T. G. Kharina, and J.-P. Heliot, "Analytical antenna model for chiral scatterers: comparison with numerical and experimental data," *IEEE Transactions on Antennas and Propagation*, vol. 44, no. 7, pp. 1006–1014, 1996.

[56] K. Achouri, "Synthesis and applications of electromagnetic metasurfaces," Ph.D. dissertation, École Polytechnique de Montréal, 2017.

[57] V. Asadchy, "Spatially dispersive metasurfaces," Ph.D. dissertation, Aalto University, Espoo, Finland, 2017.

[58] K. Achouri and C. Caloz, "Design, concepts, and applications of electromagnetic metasurfaces," *Nanophotonics*, vol. 7, no. 6, pp. 1095–1116, 2018.

[59] Z. Liu, N. Bayat, and P. Mojabi, "On the use of absorbing metasurfaces in microwave imaging," *TechRxiv preprint Techrxiv.13063925.v1*, Oct 2020.

[60] C. Caloz and A. Sihvola, "Electromagnetic chirality, part 1: the microscopic perspective [electromagnetic perspectives]," *IEEE Antennas and Propagation Magazine*, vol. 62, no. 1, pp. 58–71, 2020.

[61] V. G. Ataloglou, M. Chen, M. Kim, and G. V. Eleftheriades, "Microwave Huygens metasurfaces: Fundamentals and applications," *IEEE Journal of Microwaves*, vol. 1, no. 1, pp. 374–388, 2021.

[62] J. P. Wong, A. Epstein, and G. V. Eleftheriades, "Reflectionless wide-angle refracting metasurfaces," *IEEE Antennas and Wireless Propagation Letters*, vol. 15, pp. 1293–1296, 2015.

[63] C. Pfeiffer and A. Grbic, "Millimeter-wave transmitarrays for wavefront and polarization control," *IEEE Transactions on Microwave Theory and Techniques*, vol. 61, no. 12, pp. 4407–4417, 2013.

[64] K. Achouri, G. Lavigne, and C. Caloz, "Comparison of two synthesis methods for birefringent metasurfaces," *Journal of Applied Physics*, vol. 120, no. 23, p. 235305, 2016.

[65] T. Brown, Y. Vahabzadeh, C. Caloz, and P. Mojabi, "Electromagnetic inversion with local power conservation for metasurface design," *IEEE Antennas and Wireless Propagation Letters*, vol. 19, no. 8, pp. 1291–1295, 2020.

[66] D. M. Pozar, *Microwave engineering*. John wiley & sons, 2011.

[67] M. B. Steer, *Foundations of Interconnect and Microstrip Design*. John Wiley & Sons, 2000.

[68] D. A. Frickey, "Conversions between S, Z, Y, H, ABCD, and T parameters which are valid for complex source and load impedances," *IEEE Transactions on Microwave Theory and Techniques*, vol. 42, no. 2, pp. 205–211, 1994.

[69] C. Caloz and A. Sihvola, "Electromagnetic chirality, part 2: The macroscopic perspective [electromagnetic perspectives]," *IEEE Antennas and Propagation Magazine*, vol. 62, no. 2, pp. 82–98, 2020.

[70] P. C. Hansen, *Rank-deficient and discrete ill-posed problems: numerical aspects of linear inversion*. SIAM, 1998.

[71] ——, "Regularization tools: a Matlab package for analysis and solution of discrete ill-posed problems," *Numerical algorithms*, vol. 6, no. 1, pp. 1–35, 1994.

[72] M. Ostadrahimi, P. Mojabi, C. Gilmore, A. Zakaria, S. Noghanian, S. Pistorius, and J. LoVetri, "Analysis of incident field modeling and incident/scattered field calibration techniques in microwave tomography," *IEEE Antennas and Wireless Propagation Letters*, vol. 10, pp. 900–903, 2011.

[73] E. Razzicchia, I. Sotiriou, H. Cano-Garcia, E. Kallos, G. Palikaras, and P. Kosmas, "Feasibility study of enhancing microwave brain imaging using metamaterials," *Sensors*, vol. 19, no. 24, p. 5472, 2019.

[74] Z. Liu and P. Mojabi, "Investigating the use of matching metasurfaces in microwave imaging," in *IEEE International Symposium on Antennas and Propagation and USNC-URSI Radio Science Meeting (submitted)*, 2021, pp. 1–2.

[75] A. Grbic, L. Jiang, and R. Merlin, "Near-field plates: Subdiffraction focusing with patterned surfaces," *Science*, vol. 320, no. 5875, pp. 511–513, 2008.

[76] N. Bayat and P. Mojabi, "On the use of focused incident near-field beams in microwave imaging," *Sensors*, vol. 18, no. 9, p. 3127, 2018.

[77] Z. Liu, N. Bayat, and P. Mojabi, "On microwave imaging with absorbing metasurface enclosure," in *2020 IEEE International Symposium on Antennas and Propagation and North American Radio Science Meeting*, 2020, pp. 1223–1224.

[78] ——, "On the use of absorbing metasurfaces in microwave imaging," in *IEEE transactions on antennas and propagation (under review)*, 2020, pp. 1–6.

[79] P. M. Meaney, C. J. Fox, S. D. Geimer, and K. D. Paulsen, "Electrical characterization of glycerin: Water mixtures: Implications for use as a coupling medium in microwave tomography," *IEEE transactions on microwave theory and techniques*, vol. 65, no. 5, pp. 1471–1478, 2017.

[80] C. Gilmore, A. Zakaria, J. LoVetri, and S. Pistorius, "A study of matching fluid loss in a biomedical microwave tomography system," *Medical physics*, vol. 40, no. 2, p. 023101, 2013.

[81] T. Rubæk, P. M. Meaney, P. Meincke, and K. D. Paulsen, "Nonlinear microwave imaging for breast-cancer screening using Gauss–Newton's method and the CGLS inversion algorithm," *IEEE Transactions on Antennas and Propagation*, vol. 55, no. 8, pp. 2320–2331, 2007.

[82] P. M. van den Berg and J. T. Fokkema, "Removal of undesired wavefields related to the casing of a microwave scanner," *IEEE Transactions on Microwave Theory and Techniques*, vol. 51, no. 1, pp. 187–192, 2003.

[83] M. Asefi, A. Baran, and J. LoVetri, "An experimental phantom study for air-based quasi-resonant microwave breast imaging," *IEEE Transactions on Microwave Theory and Techniques*, vol. 67, no. 9, pp. 3946–3954, 2019.

[84] M. Del Mastro, M. Ettorre, and A. Grbic, "Dual-band, Orthogonally-Polarized LP-to-CP Converter for Satcom Applications," *IEEE Transactions on Antennas and Propagation*, vol. 68, no. 9, pp. 6764–6776, 2020.

[85] N. Engheta, "Thin absorbing screens using metamaterial surfaces," in *IEEE APS International Symposium*, vol. 2, June 2002, pp. 392–395.

[86] Y. Ra'di, V. S. Asadchy, and S. A. Tretyakov, "Total absorption of electromagnetic waves in ultimately thin layers," *IEEE Transactions on Antennas and Propagation*, vol. 61, no. 9, pp. 4606–4614, Sep. 2013.

[87] O. Luukkonen, F. Costa, C. R. Simovski, A. Monorchio, and S. A. Tretyakov, "A thin electromagnetic absorber for wide incidence angles and both polarizations," *IEEE Transactions on Antennas and Propagation*, vol. 57, no. 10, pp. 3119–3125, 2009.

[88] K. Achouri and O. J. Martin, "Angular scattering properties of metasurfaces," *IEEE Transactions on Antennas and Propagation*, vol. 68, no. 1, pp. 432–442, 2019.

[89] J. A. Stratton, *Electromagnetic theory*. John Wiley & Sons, 2007, vol. 33.

[90] R. F. Harrington, *Time-harmonic electromagnetic fields*. McGraw-Hill, 1961.

[91] C. Estatico, A. Fedeli, M. Pastorino, and A. Randazzo, "Quantitative microwave imaging method in Lebesgue spaces with nonconstant exponents," *IEEE Transactions on Antennas and Propagation*, vol. 66, no. 12, pp. 7282–7294, 2018.

[92] S. Gregson, J. McCormick, and C. Parini, *Principles of planar near-field antenna measurements*. IET, 2007, vol. 53.

[93] G. Lavigne and C. Caloz, "Angle-independent nongyrotropic metasurfaces," in *2019 Thirteenth International Congress on Artificial Materials for Novel Wave Phenomena (Metamaterials)*, 2019, pp. X–209–X–211.

[94] P. Mojabi and J. LoVetri, "A prescaled multiplicative regularized Gauss-Newton inversion," *IEEE Transactions on Antennas and Propagation*, vol. 59, no. 8, pp. 2954–2963, Aug 2011.

[95] Ohmega Technologies, Inc., "Ohmegaply product selection guide," https://ohmega.com/wp-content/uploads/Ohmega-Brochure-01012016.pdf.

[96] M. Yoo and S. Lim, "Polarization-independent and ultrawideband metamaterial absorber using a hexagonal artificial impedance surface and a resistor-capacitor layer," *IEEE transactions on antennas and propagation*, vol. 62, no. 5, pp. 2652–2658, 2014.

[97] P. Mojabi, M. Ostadrahimi, L. Shafai, and J. LoVetri, "Microwave tomography techniques and algorithms: A review," in *2012 Fifteenth International Symposium on Antenna Technology and Applied Electromagnetics*, 2012, pp. 1–4.

[98] F. Yang, B. O. Raeker, D. T. Nguyen, J. D. Miller, Z. Xiong, A. Grbic, and J. S. Ho, "Antireflection and wavefront manipulation with cascaded metasurfaces," *Physical Review Applied*, vol. 14, no. 6, p. 064044, 2020.

[99] W. Zheng and T. Hao, "Transmission enhancement by antireflective metasurface for ground penetrating radar applications," in *2019 Thirteenth International Congress on Artificial Materials for Novel Wave Phenomena (Metamaterials)*. IEEE, 2019, pp. X–489.

[100] N. Bayat and P. Mojabi, "Incorporating spatial priors in microwave imaging via multiplicative regularization," *IEEE Transactions on Antennas and Propagation*, vol. 68, no. 2, pp. 1107–1118, 2020.

[101] M. Ostadrahimi, P. Mojabi, S. Noghanian, J. LoVetri, and L. Shafai, "A multiprobe-per-collector modulated scatterer technique for microwave tomography," *IEEE Antennas and Wireless Propagation Letters*, vol. 10, pp. 1445–1448, 2011.

[102] U. Kaatze, "Complex permittivity of water as a function of frequency and temperature," *Journal of Chemical and Engineering Data*, vol. 34, no. 4, pp. 371–374, 1989.

[103] N. Bayat and P. Mojabi, "A multiplicative regularizer augmented with spatial priors for microwave imaging," *IEEE Transactions on Antennas and Propagation*, vol. 69, no. 1, pp. 606–611, 2021.

[104] K. Achouri and O. J. Martin, "Multipolar modeling of spatially dispersive metasurfaces," *arXiv preprint arXiv:2103.10345*, 2021.

[105] F. Liu, O. Tsilipakos, A. Pitilakis, A. C. Tasolamprou, M. S. Mirmoosa, N. V. Kantartzis, D.-H. Kwon, J. Georgiou, K. Kossifos, M. A. Antoniades, M. Kafesaki, C. M. Soukoulis, and S. A. Tretyakov, "Intelligent metasurfaces with continuously tunable local surface impedance for multiple reconfigurable functions," *Physical Review Applied*, vol. 11, no. 4, p. 044024, 2019.

[106] K. M. Kossifos, L. Petrou, G. Varnava, A. Pitilakis, O. Tsilipakos, F. Liu, P. Karousios, A. C. Tasolamprou, M. Seckel, D. Manessis, N. V. Kantartzis, D.-H. Kwon, M. A. Antoniades, and J. Georgiou, "Toward the realization of a programmable metasurface absorber enabled by custom integrated circuit technology," *IEEE Access*, vol. 8, pp. 92 986–92 998, 2020.

[107] C. Caloz and Z.-L. Deck-Léger, "Spacetime metamaterials," *arXiv preprint arXiv:1905.00560*, 2019.

[108] S. Taravati and G. V. Eleftheriades, "Full-duplex nonreciprocal beam steering by time-modulated phase-gradient metasurfaces," *Physical Review Applied*, vol. 14, no. 1, p. 014027, 2020.

[109] V. Rodriguez, *Anechoic Range Design for Electromagnetic Measurements*. Artech House, 2019.

[110] J. M. Sill and E. C. Fear, "Tissue sensing adaptive radar for breast cancer detectionexperimental investigation of simple tumor models," *IEEE Transactions on Microwave theory and Techniques*, vol. 53, no. 11, pp. 3312–3319, 2005.

Appendix A

Relation Between the Susceptibility and Impedance Models

The GSTCs based on the susceptibility model in (2.30) are

$$\boldsymbol{J}_{\mathrm{e},s} = j\omega\varepsilon_0\overline{\overline{\chi}}_{\mathrm{ee}}\boldsymbol{E}_t^{\mathrm{av}} + j\omega\sqrt{\varepsilon_0\mu_0}\overline{\overline{\chi}}_{\mathrm{em}}\boldsymbol{H}_t^{\mathrm{av}} \tag{A.1a}$$

$$\boldsymbol{J}_{\mathrm{m},s} = j\omega\mu_0\overline{\overline{\chi}}_{\mathrm{mm}}\boldsymbol{H}_t^{\mathrm{av}} + j\omega\sqrt{\varepsilon_0\mu_0}\overline{\overline{\chi}}_{\mathrm{me}}\boldsymbol{E}_t^{\mathrm{av}} \tag{A.1b}$$

Assuming $\bar{\bar{A}} = j\omega\varepsilon_0\overline{\overline{\chi}}_{\mathrm{ee}}$, $\bar{\bar{B}} = j\omega\sqrt{\varepsilon_0\mu_0}\overline{\overline{\chi}}_{\mathrm{em}}$, $\bar{\bar{C}} = j\omega\sqrt{\varepsilon_0\mu_0}\overline{\overline{\chi}}_{\mathrm{me}}$, and $\bar{\bar{D}} = j\omega\mu_0\overline{\overline{\chi}}_{\mathrm{mm}}$ and the GSTCs can be written as

$$\boldsymbol{J}_{\mathrm{e},s} = \bar{\bar{A}}\boldsymbol{E}_t^{\mathrm{av}} + \bar{\bar{B}}\boldsymbol{H}_t^{\mathrm{av}} \tag{A.2a}$$

$$\boldsymbol{J}_{\mathrm{m},s} = \bar{\bar{D}}\boldsymbol{H}_t^{\mathrm{av}} + \bar{\bar{C}}\boldsymbol{E}_t^{\mathrm{av}} \tag{A.2b}$$

Therefore the averaged tangential electric field can be obtained by replacing $\boldsymbol{H}_t^{\text{av}}$ in (A.2a) from (A.2b)

$$\boldsymbol{J}_{\text{e},s} \;=\; \bar{\bar{A}}\boldsymbol{E}_t^{\text{av}} \;+\; \bar{\bar{B}}\bar{\bar{D}}^{-1}(\boldsymbol{J}_{\text{m},s} \;-\; \bar{\bar{C}}\boldsymbol{E}_t^{\text{av}})$$

and then writing it in the following form

$$(\bar{\bar{A}} \;-\; \bar{\bar{B}}\bar{\bar{D}}^{-1}\bar{\bar{C}})\boldsymbol{E}_t^{\text{av}} \;=\; \boldsymbol{J}_{\text{e},s} \;-\; \bar{\bar{B}}\bar{\bar{D}}^{-1}\boldsymbol{J}_{\text{m},s}$$

where the superscript '-1' denotes the inverse of the tensor.

Finally, the averaged tangential electric field is

$$\boldsymbol{E}_t^{\text{av}} \;=\; (\bar{\bar{A}} \;-\; \bar{\bar{B}}\bar{\bar{D}}^{-1}\bar{\bar{C}})^{-1}\boldsymbol{J}_{\text{e},s} \;-\; (\bar{\bar{A}} \;-\; \bar{\bar{B}}\bar{\bar{D}}^{-1}\bar{\bar{C}})^{-1}\bar{\bar{B}}\bar{\bar{D}}^{-1}\boldsymbol{J}_{\text{m},s}$$

Similarly, the average tangential magnetic field can be obtained by replacing $\boldsymbol{E}_t^{\text{av}}$ in (A.2a) from (A.2b)

$$\boldsymbol{J}_{\text{e},s} \;=\; \bar{\bar{A}}\bar{\bar{C}}^{-1}(\boldsymbol{J}_{\text{m},s} \;-\; \bar{\bar{D}}\boldsymbol{H}_t^{\text{av}}) \;+\; \bar{\bar{B}}\boldsymbol{H}_t^{\text{av}}$$

and then arrive at

$$(\bar{\bar{A}}\bar{\bar{C}}^{-1}\bar{\bar{D}} \;-\; \bar{\bar{B}})\boldsymbol{H}_t^{\text{av}} \;=\; \bar{\bar{A}}\bar{\bar{C}}^{-1}\boldsymbol{J}_{\text{m},s} \;-\; \boldsymbol{J}_{\text{e},s}$$

Finally, the averaged tangential magnetic field will be

$$\boldsymbol{H}_t^{\text{av}} \;=\; (\bar{\bar{A}}\bar{\bar{C}}^{-1}\bar{\bar{D}} \;-\; \bar{\bar{B}})^{-1}\bar{\bar{A}}\bar{\bar{C}}^{-1}\boldsymbol{J}_{\text{m},s} \;-\; (\bar{\bar{A}}\bar{\bar{C}}^{-1}\bar{\bar{D}} \;-\; \bar{\bar{B}})^{-1}\boldsymbol{J}_{\text{e},s}$$

Overall, the GSTCs can be re-expressed as

$$\begin{aligned}
\boldsymbol{E}_t^{\text{av}} \;&=\; (\bar{\bar{A}} \;-\; \bar{\bar{B}}\bar{\bar{D}}^{-1}\bar{\bar{C}})^{-1}\boldsymbol{J}_{\text{e},s} \;-\; (\bar{\bar{A}} \;-\; \bar{\bar{B}}\bar{\bar{D}}^{-1}\bar{\bar{C}})^{-1}\bar{\bar{B}}\bar{\bar{D}}^{-1}\boldsymbol{J}_{\text{m},s} \\
\boldsymbol{H}_t^{\text{av}} \;&=\; (\bar{\bar{A}}\bar{\bar{C}}^{-1}\bar{\bar{D}} \;-\; \bar{\bar{B}})^{-1}\bar{\bar{A}}\bar{\bar{C}}^{-1}\boldsymbol{J}_{\text{m},s} \;-\; (\bar{\bar{A}}\bar{\bar{C}}^{-1}\bar{\bar{D}} \;-\; \bar{\bar{B}})^{-1}\boldsymbol{J}_{\text{e},s}
\end{aligned}$$

The above equation can then be compared with (2.20) to find the relationship between

the impedance and susceptibility models.

Appendix B

Appandix Matlab code

```
% This code accepts scattering parameters of a metasurface unit cell
% with the cascaded layer topology simulated in Ansys HFSS and finds
% Y_1, Y_2, Y_3 or equivalent Z_1, Z_2, Z_3 from the S parameters

% INPUTS:
% c0 - Light speed
% Freq - Operating frequency
% permMedia - Permittivity of the background medium
% lambda - Wavelength in free space
% permSub - Permittivity of the substrate
% beta - Wave number in the substrate
% Zsub - Characteristic impedance of the substrate
% tsub - Thickness of the substrate
% Z0 - Medium impedance in free space
% ZS - Wave impedance on the source side
% ZL - Wave impedance on the output side
% MTL - T parameters of substrate
```

```
% perm_in - Relative permittivity of the medium on input side
% perm_out - Relative permittivity of the medium on output side
% inputAngle - Incident angle with respect to the metasurface
% outputAngle - Refracted angle with respect to the metasurface
% Layer - Which layer is about to solve
% polarization - The illuminating polarization
% 'S_Parameters.csv' is the S parameters directly exported from HFSS,
% the format is shown as follows
```

Freq [GHz]	S(1,1)[ ]	S(1,2)[ ]	S(2,1)[ ]	S(2,2)[ ]
1	0.078+0.242i	0.925-0.263i	0.925-0.263i	0.075+0.244i

Table B.1: S˙Parameters.csv

```
% OUTPUTS:
% Ztop - The impedance value for the top layer
% Zmid - Middle layer impedance value
% Zbot - Bottom layer impedance value
%
% Author: Ziqi Liu
% Date created: Oct. 13, 2019
% Revised: Jun. 1, 2021

%------------------------------------------------------------------------
clear all; close all; clc
%========================================================================
% Input values
%========================================================================
c0 = 1/sqrt(4*pi*1e-7 * 8.85 * 1e-12);
```

```
Freq = 1e9;
lambda = c0/(Freq);
permSub  =  3;
tsub = 1.52e-3;

inputAngle = 0;
outputAngle = 0;
perm_in = 1;
perm_out = 1;
polarization = 'TE'; % TM or TE

%=========================================================================
Z0 = 120 * pi;
if isequal(polarization,'TM')
    ZL = Z0 * cosd(outputAngle)/sqrt(perm_out);
elseif isequal(polarization,'TE')
    ZL = Z0 / cosd(outputAngle)/sqrt(perm_out);
else
    error('the polarization needs to be either TM or TE.')
end
if isequal(polarization,'TM')
    ZS = Z0 * cosd(inputAngle)/sqrt(perm_in);
elseif isequal(polarization,'TE')
    ZS = Z0 / cosd(inputAngle)/sqrt(perm_in);
else
    error('the polarization needs to be either TM or TE.')
end
```

```
beta = sqrt(permSub) * 2 * pi / lambda;
Zsub = 120 * pi / sqrt(permSub);

%=========================================================================
% S parameter obtain from HFSS
[num,txt,raw] = xlsread('S_Parameters.csv'); %The S parameters collected
                %from HFSS are save in the file, named 'S_Parameters.csv'

S = txt(2:end,2:end);
numofturns = size(num);
level = ["top","middle","bottom"]; % 'top' 'middle' or 'bottom' layer
layer = level(1);
for n = 1:numofturns
    %=====================================================================
    S11 = str2num(string(S(n,1)));
    S12 = str2num(string(S(n,2)));
    S21 = str2num(string(S(n,3)));
    S22 = str2num(string(S(n,4)));
    % Convert S parameters to T parameters
    T_11 = ((ZS'+S11*ZS)*(1-S22)+S12*S21*ZS)/(2*S21*sqrt(real(ZS)*real(ZL)));
    T_12 = ((ZS'+S11*ZS)*(ZL'+S22*ZL)-S12*S21*ZS*ZL)/(2*S21*sqrt(real(ZS)*real(ZL)));
    T_21 = ((1-S11)*(1-S22)-S12*S21)/(2*S21*sqrt(real(ZS)*real(ZL)));
    T_22 = ((1-S11)*(ZL'+S22*ZL)+S12*S21*ZL)/(2*S21*sqrt(real(ZS)*real(ZL)));
    Ttotal = [T_11,T_12;T_21,T_22];
    %=====================================================================
    % Substrate equation
```

```
    % In this case the substrates are the same with pure real characteristic
    % impedance value. Therefore, we assume MTL to represent substrate T parameters
    MTL = [cos(beta * tsub) ,1i*Zsub * sin(beta * tsub); (1i/Zsub) ...
                                    * sin(beta * tsub), cos(beta * tsub)];
    %=========================================================================
    % Impedance conversion
    if isequal(layer,'top')
        Y = (Ttotal/MTL)/MTL;
        Ztop(n) = 1/Y(2,1);
    elseif isequal(layer,'middle')
        Y = MTL\Ttotal/MTL;
        Zmiddle(n) = 1/Y(2,1);
    elseif isequal(layer,'bottom')
        Y = MTL\(MTL\Ttotal);
        Zbottom(n) = 1/Y(2,1);
    else
        error('the layer must be one of top, middle and bottom layers')
    end
end
```

Appendix C

Standard Absorbers and MWI

Standard absorber technology typically relies on one of the following two mechanisms for loss [109, Chapter 3], in which they are known to usually outperform metasurface absorber in terms of angular stability. However, the main problems of such absorbers are

- ***Electric Loss:*** A typical relative complex permittivity of such absorbers is about $\varepsilon_r = 1.8 - j1.7$. Based on this value, it is obvious that the purpose of such absorbers is to be matched to air ($\varepsilon_r = 1$). A half-space with this relative complex permittivity will have a reflection coefficient of about -10.64 dB for normal incidence from air, which is not sufficient for many applications. To further minimize the reflections, these absorbers are often designed in the form of pyramids so that the permittivity gradually changes, e.g., from 1 to $1.8 - j1.7$. This requires the height of the pyramidal absorber to be about 1λ to 5λ (or even more) where λ is the wavelength. Thus,
  - Standard absorbers with electric loss are designed to be matched to air. Consequently, they will not be able to work with arbitrary background medium such as the absorbing metasurface considered in this thesis. Note that the background medium in microwave imaging can be very different such as canola oil [110], water with different amounts of salt [80], different ratios of glycerin: water mixture [79], air [47], etc.

- Due to the pyramidal shape of these standard absorbers, they can be bulky, and are not appropriate for portable system. In addition, the tip of these absorbers is important and needs to be handled with care.
- Standard absorbers with electric loss come in other shapes. For example, if we decide to use flat laminate absorbers, their reflectivity will be limited to about -20 dB (but still for the air background medium). Finally, the use of wedge-shape absorbers with electric loss is not relevant for this case.

- ***Magnetic Loss:*** Ferrite tiles are compact (between 4 mm and 7 mm) due to their use of metal backing [109, Chapter 3]. However, they have the following disadvantages for microwave imaging:
  - They are mainly available from 10 MHz to 1.5 GHz. Depending on the object being imaged and the desired spatial resolution, one might needs to operate a microwave imaging system at a higher frequency. This will be a limitation of these standard absorbers with magnetic loss.
  - The permeability (and permittivity) of these absorbers are designed such that when used with metalic backing, they have small reflections. Therefore, these are still appropriate for air background medium, and cannot be used with an arbitrary background medium.

Appendix D

Horn Antenna Characterization

Herein, we will present the details of the horn antenna performance used in the experimental part of this thesis.

- We have measured the utilized horn antenna in a compact antenna test range (CATR) as shown in Figure D.1. A close up view is also shown in Figure D.2.
- The gain of this antenna has been obtained in the X-band using the gain comparison method.
- The measured maximum gain of this antenna versus frequency has been shown in Figure D.3.
  - Although the maximum gain as a function of frequency, shown in Figure D.3, is not flat, this non-uniformity is taken care of in the reported frequency-domain calibrated reflection coefficient for the metasurface shown in Fig. 4.16 of the thesis. This is due to the fact that the same horn antenna is used to illuminate the PEC (copper tape), and calibration coefficients are formed to map the results of the PEC reflection measurement to the expected reflection from PEC (0 dB flat line as a function of frequency). When the same calibration coefficients are applied to the metasurface measurements, the non-uniformity of gain versus

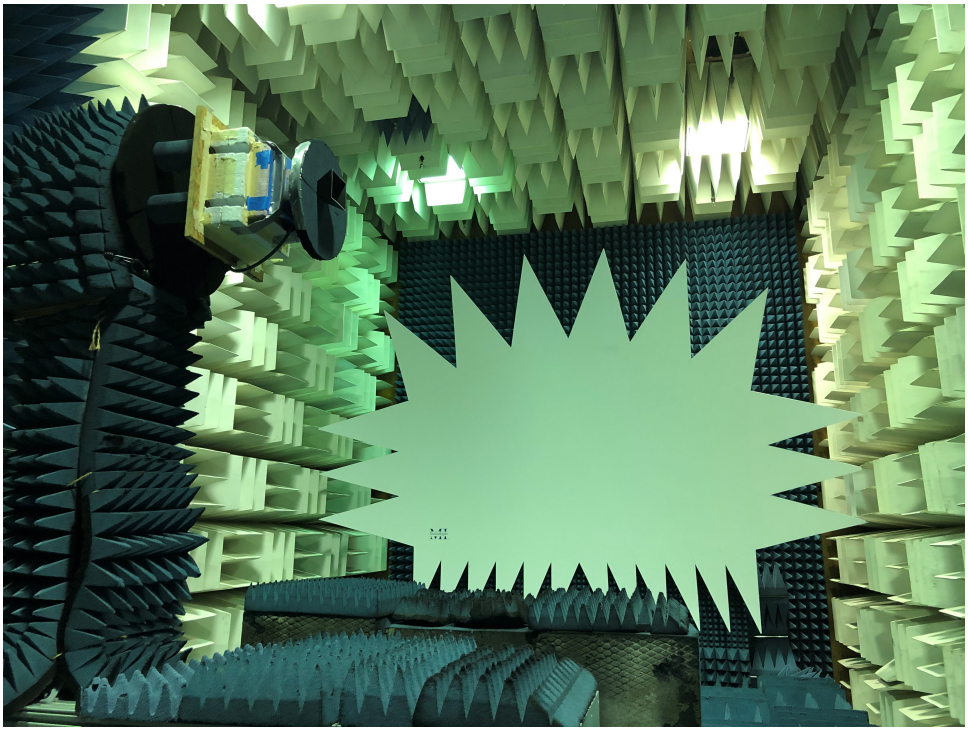

Fig. D.1: The horn antenna being measured in a compact antenna test range.

frequency is thus taken care of.

- The measured gain pattern at one cut in the front hemisphere has also been shown in Fig. D.4. The same above comment applies to this case as well.

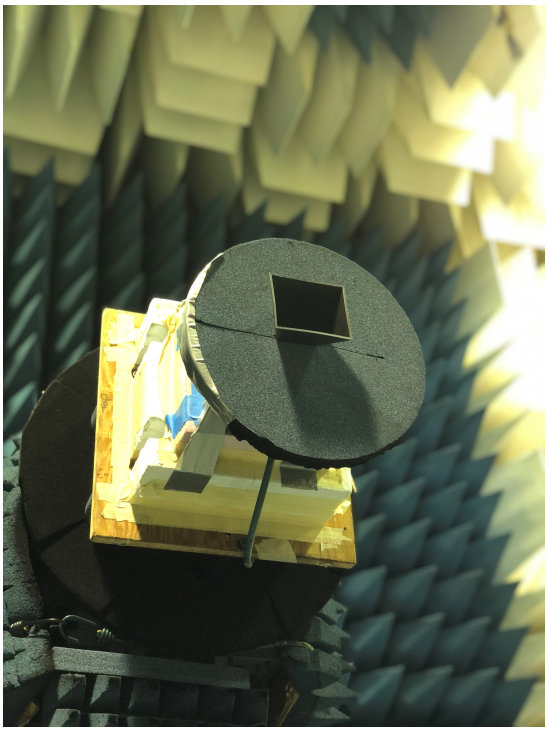

Fig. D.2: A close up view of the horn antenna being measured in a compact antenna test range.

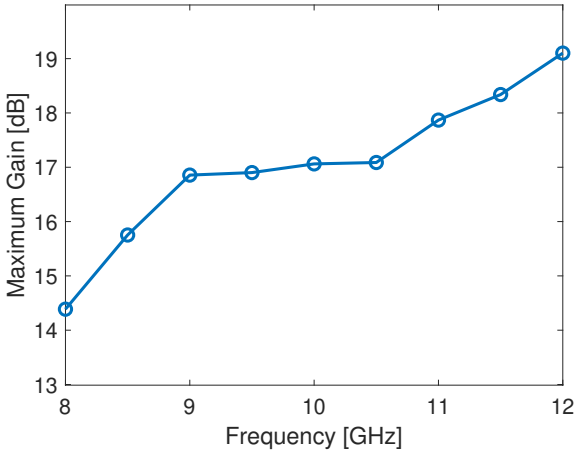

Fig. D.3: The measured maximum gain of the horn versus the frequency of operation: from 8 GHz to 12 GHz in the step of 0.5 GHz.

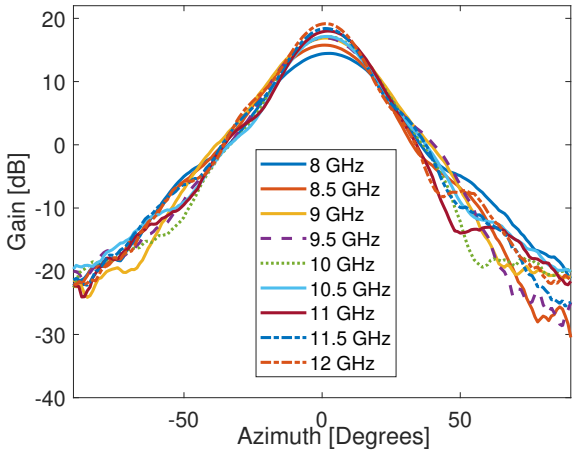

Fig. D.4: The measured gain pattern of the horn in one cut from -90° to 90° for 8 GHz to 12 GHz in the step of 0.5 GHz.